https://doi.org/10.15388/vu.thesis.739
https://orcid.org/0000-0001-6747-6167

VILNIUS UNIVERSITY
CENTER FOR PHYSICAL SCIENCES AND TECHNOLOGY

Mantas Norkus

Synthesis and Investigation of Luminescent Glass and Garnets

DOCTORAL DISSERTATION

Natural Sciences,
Chemistry (N 003)

VILNIUS 2025

The dissertation was prepared between 2017 and 2021 while studying at Vilnius University and is defended on an external basis.

Academic consultant – Prof. Dr. Ramūnas Skaudžius (Vilnius University, Natural Sciences, Chemistry – N 003).

This doctoral dissertation will be defended in a public meeting of the Dissertation Defence Panel:

Chairman – Assoc. Prof. Dr. Justina Gaidukevič (Vilnius University, Natural Sciences, Chemistry – N 003).
Members:
Prof. Dr. Kęstutis Baltakys (Kaunas University of Technology, Technology Sciences, Chemical Engineering – T 005),
Assoc. Prof. Dr. Inga Grigoravičiūtė (Vilnius University, Natural Sciences, Chemistry – N 003),
Dr. Loreta Tamašauskaitė-Tamašiūnaitė (Center for Physical Sciences and Technology, Natural Sciences, Chemistry – N 003),
Assoc. Prof. Dr. Vaclav Tyrpekl (Charles University, Natural Sciences, Chemistry – N 003).

The dissertation shall be defended at a public meeting of the Dissertation Defence Panel at 2 p.m. on 07 March 2025 in Inorganic Chemistry auditorium 141 of the Institute of Chemistry, Faculty of Chemistry and Geosciences, Vilnius University.

Address: Naugarduko street 24, LT-03225 Vilnius, Lithuania
Tel. +370 52193105; e-mail: info@chgf.vu.lt

The text of this dissertation can be accessed at the libraries of Vilnius University and Center for Physical Sciences and Technology, as well as on the website of Vilnius University:
www.vu.lt/lt/naujienos/ivykiu-kalendorius

https://doi.org/10.15388/vu.thesis.739
https://orcid.org/0000-0001-6747-6167

VILNIAUS UNIVERSITETAS
FIZINIŲ IR TECHNOLOGIJOS MOKSLŲ CENTRAS

Mantas Norkus

Liuminescencinio stiklo ir granatų struktūros junginių sintezė ir tyrimas

DAKTARO DISERTACIJA

Gamtos mokslai,
chemija (N 003)

VILNIUS 2025

Disertacija rengta 2017 – 2021 metais studijuojant doktorantūroje Vilniaus universitete ir ginama eksternu.

Mokslinis vadovas – prof. dr. Ramūnas Skaudžius (Vilniaus universitetas, gamtos mokslai, chemija – N 003).

Gynimo taryba:
Pirmininkė – doc. dr. Justina Gaidukevič (Vilniaus universitetas, gamtos mokslai, Chemija N 003).
Nariai:
prof. dr. Kęstutis Baltakys (Kauno technologijos universitetas, technologijos mokslai, chemijos inžinerija, T 005),
doc. dr. Inga Grigoravičiūtė (Vilniaus universitetas, gamtos mokslai, chemija, N 003),
dr. Loreta Tamašauskaitė-Tamašiūnaitė (Fizinių ir technologijos mokslų centras, gamtos mokslai, chemija, N 003),
doc. dr. Vaclav Tyrpekl (Prahos Karolio universitetas, gamtos mokslai, Chemija, N 003).

Disertacija ginama viešame Gynimo tarybos posėdyje 2025 m. kovo mėn. 7 d. 15 val. Vilniaus universiteto Chemijos ir geomokslų fakulteto / Chemijos instituto Neorganinės chemijos auditorijoje. Adresas: Naugarduko g. 24, LT-03225, Vilnius, Lietuva tel. +37052193108 ; el. paštas info@chgf.vu.lt.
Disertaciją galima peržiūrėti Vilniaus universiteto, Fizinių ir technologijos mokslų centro bibliotekose ir VU interneto svetainėje adresu:
https://www.vu.lt/naujienos/ivykiu-kalendorius

LIST OF SYMBOLS AND ABBREVIATIONS

GGG – Gadolinium Gallium Garnet, $Gd_3Ga_5O_{12}$;

YAG – Yttrium Aluminum Garnet, $Y_3Al_5O_{12}$;

YAG:Ce – Yttrium Aluminum Garnet doped with cerium;

YAG:Er – Yttrium Aluminum Garnet doped with erbium;

YAG:Nd – Yttrium Aluminum Garnet doped with neodymium;

YAM – Yttrium Aluminum Oxide $Y_4Al_2O_9$ with monoclinic structural unit;

YAP – Yttrium Aluminum Oxide $YAlO_3$ with perovskite structural unit;

YIG – Yttrium Iron Garnet, $Y_3Fe_5O_{12}$;

RE – Rare Earth;

W-LED – white light emitting diode;

XRD – X-ray diffraction;

SEM – Scanning electron microscopy;

EDX – energy dispersive X-Ray spectroscopy.

TABLE OF CONTENTS

INTRODUCTION

In the ever-evolving landscape of advanced ceramic materials, the synthesis and study of luminescent glass and garnets is at the forefront of scientific inquiry, offering transformative potential for a wide range of applications. As we navigate the new media age, the pivotal role played by the telecommunications industry is evident, particularly with the shift from copper wire communications to the advent of fiber optic communications in the late 1980s. This revolutionary method involves the transmission of information through pulses of infrared light along optical fibers, ushering in a new era for applications in optical glass, displays, optical sensors and solid-state lasers in the field of optoelectronics [1,2].

The ever-increasing demand for novel optical glasses, especially those doped with rare earth (RE) ions, demonstrates the relentless pursuit of innovative solutions. Optical glasses, especially phosphate glasses, are emerging as the preferred optical medium due to their advantages over crystalline materials. Ease of preparation, casting capabilities and the inherent ability to accept activator RE ions make them an integral part of the optoelectronic arsenal. However, despite these advantages, the widespread adoption of RE ions is hindered by concentration quenching, where an increase in the concentration of RE oxide beyond a certain threshold leads to a decrease in the fluorescence lifetime, a phenomenon with detrimental effects on the lasing properties [3–7].

Phosphate-based glass, composed of metaphosphates of various metals, is unique in its composition, with P_2O_5 as the glass-forming structural backbone. Compared to borate, silicate and other glasses, the distinctive chemical and physical properties result from the different glass network formers. Silica and borate glasses, which are soluble in hydrofluoric acid, contrast sharply with phosphate glasses, which are highly resistant to this acid. Another critical difference is the melting point, with borosilicate glass having a higher temperature threshold than silica or phosphate glasses [2,8–13].

The superior properties of RE doped phosphate glass make it particularly suitable for fiber optic communications. In this field, compactness, high beam quality through single-mode operation and excellent heat dissipation are essential to ensure high laser reliability and long-term stability. The search for an active medium with high optical gain over a short length becomes paramount to realize efficient devices while mitigating non-linear optical effects. Among RE ions, Eu^{3+} emerges as a prominent choice due to its narrow fluorescence peaks and longer optically active state lifetimes derived from the $^5D_0 \rightarrow ^7F_J$ transitions and their splitting, which are concentration-dependent [14–17].

As the demand for advanced ceramic materials continues to grow, we are entering the realm of yttrium aluminum garnet, an optical oxide ceramic with a nominal composition of $Y_3Al_5O_{12}$. Initially optically isotropic, YAG transforms into a versatile material when doped with various trivalent ions, particularly lanthanides. This transformation has paved the way for remarkable successes in research studies and commercial viability, exemplified by YAG:Nd, YAG:Er solid-state lasers and the luminescent application of YAG:Ce in cathode ray tubes and light emitting diodes [18–21].

The limitations of single-crystal laser materials, such as technological challenges related to melt temperature variation and inhomogeneous distribution of optically active ions, were overcome by the groundbreaking introduction of polycrystalline YAG:Nd ceramic lasers in 1995. This development not only demonstrated equivalent or superior properties to single-crystal lasers, but also opened avenues for the exploration of polycrystalline YAG as a viable replacement, opening up possibilities for complex geometries, multi-layered structural units and increased scalability [18,22].

This investigation extends to the luminescence properties of chromium-doped YAG and presents findings that are contrary to the typical concentration-dependent effects reported in the literature. In the well-established YAG host material, the occupation of tetrahedrally coordinated Al^{3+} sites by Cr^{4+} or Cr^{3+} ions, found in octahedrally coordinated Al^{3+} sites, dramatically alters the luminescence properties [23–31]. By combining polycrystalline ceramic powders with a host glass matrix, the fundamental issue of scalability versus cost is practically mitigated [32,33].

In parallel with the study of luminescent glass and YAG, a third area of research has emerged involving ferrites in the form of nanoparticles. These magnetic nanoparticles, with applications ranging from electronics to biotechnology and medicine, offer unique properties such as ferrimagnetism, excellent creep and radiation damage resistance, and energy transfer efficiency. Among these, yttrium iron garnet ($Y_3Fe_5O_{12}$; YIG) with its cubic garnet structure has been extensively studied for its magnetic, magneto-optical, thermal, electrical and mechanical properties. The versatility of lanthanide substituted garnets ($Ln_3Fe_5O_{12}$) positions them as suitable candidates for various device applications, including magnetic materials, sensors, lasers, phosphorescent sources and microwave devices [34–42].

The behavior of yttrium iron garnet, as shown in numerous publications, depends on valence-uncompensated doping or substitution of iron in tetrahedral or octahedral sites, as well as substitution of yttrium in dodecahedral sites by different metallic cations. This nuanced dependence is crucial for tailoring the properties of ferruginous garnets for specific applications. Various synthesis methods, from solid state reactions to sol-gel synthesis, have been explored for the preparation of iron garnets. The choice of synthesis technique is crucial as it determines the resulting magnetic properties such as coercivity, saturation magnetization and Neel temperature [43–47].

The aim of the thesis is to develop a synthesis route for luminescent glass incorporating Eu ions in its structure and garnets YAG:Cr, YIG doped with La, Ce, Pr, Nd and to study their properties.

The objectives of this research are:

- To determine the potential structure of phosphate glass doped with rare earth ions;
- To characterize the properties of doped YIG as a function of dopant concentration and whether single phase garnets can be synthesized under current conditions;
- To understand the luminescence behavior of YAG:Cr, why the decrease in dopant concentration leads to an increase in luminescence intensity.

As this work unravels the intricate world of luminescent glasses and garnets, it underlines their paramount importance in the broader context of advanced ceramic materials. By bridging the realms of optical glass, YAG and nanoparticle ferrites, these synthesis and investigation efforts aim to contribute to the development of optoelectronic technologies. Through the careful study of these materials, the aim is to unlock new opportunities, address challenges and drive scientific innovation towards the realization of advanced devices and applications that push the boundaries of conventional materials and provide a different perspective on one of the oldest known man-made materials.

Statements for defense:

- In phosphate glasses doped with Eu^{3+} ions$^5D_0 \rightarrow {}^7F_2$ transition contributes more than half of emission intensity compared with the whole emission intensity;
- Single phase garnets of $Y_{3-x}Ln_xFe_5O_{12}$ can be synthesized using sol-gel synthesis method only where Ln = Pr or Nd;

- Due to the distinct emission behavior of chromium ions in yttrium aluminum garnet, the emission spectra can be employed to determine the quantity of chromium contamination in polycrystalline yttrium aluminum garnet.

LITERATURE OVERVIEW

1.1. Glass Phosphors

Substances in the solid state at normal temperature and pressure can have a crystalline or amorphous structure. Both are used as phosphors, but glass phosphors are attracting increasing attention. Typically, phosphors are embedded in a polymer matrix that can degrade dramatically when exposed to moisture, oxygen, or high temperatures. One of the main advantages of phosphors in glass composites is the ability to withstand much higher temperatures for longer periods of time without degradation, oxidation, etc. [48].

1.1.1. Differences Between Glassy and Crystalline Compounds

In nature, crystalline solids are the most common, whose structure is characterized by a geometrically strict order of particles (atoms, ions) in three-dimensional space. The crystalline state is stable under normal conditions and is characterized by the lowest internal energy. Solid crystalline substances have clear geometric shapes, certain melting temperatures, in most cases show anisotropy, i.e. their physical properties (refractive index, thermal conductivity, dissolution and crystal growth rates, etc.) are unequal when measured in different directions.

The glassy state of matter is an amorphous version of the solid state. The glassy state is metastable, i.e. it is characterized by an excess of internal energy. The spatial arrangement of particles in the glassy state is disordered, which is confirmed by the results of X-ray studies [49].

According to the laws of chemical thermodynamics, the transition of substances from the glassy to the crystalline state should be spontaneous, but the high viscosity of solids makes it impossible for particles to move forward in order to restructure. In solids, particles make only oscillatory movements relative to the equilibrium position [50].

All types of glasses, regardless of their chemical composition and solidification temperature range, have specific properties that distinguish them from crystals and liquids.

Glasses are X-ray amorphous due to their disordered atomic structure. The structure of glass lacks long-range order, i.e. systematic repetition of elementary structural volumes, which is characteristic of crystalline substances.

If we roughly determine the interplanar distance corresponding to the maximum of the amorphous halo for the silicate glass, it is close to the diffraction maximum of cristobalite - 0.415 nm. However, in the structure of glass, the particles are not at strictly defined distances as in crystallite or other crystal modifications of quartz, but at distances greater or smaller than some statistical average [51,52].

Glasses are isotropic when they are homogeneous in composition, free of stresses and defects. The isotropic properties of glasses, like those of other amorphous media, are due to the absence of spatial orientation of the particles. Optical anisotropy can occur in glass as a result of tensile or compressive stress (optical anisotropy phenomena).

Glass transition temperature range - glasses do not have a definite solidification or melting temperature. Both processes occur gradually over a range of temperatures. When cooled, the melt changes from liquid to plastic and then to solid (glass transition process). Conversely, when glass is heated, it changes from a solid state to a plastic state and at higher temperatures to a liquid state (glass softening).

The temperature range in which the glass transition or the reversal of the softening process occurs is called the glass transition range and is limited to two temperatures: on the high temperature side, T_f, and on the low temperature side, T_g (glass transition temperature) (see Figure 1) [53].

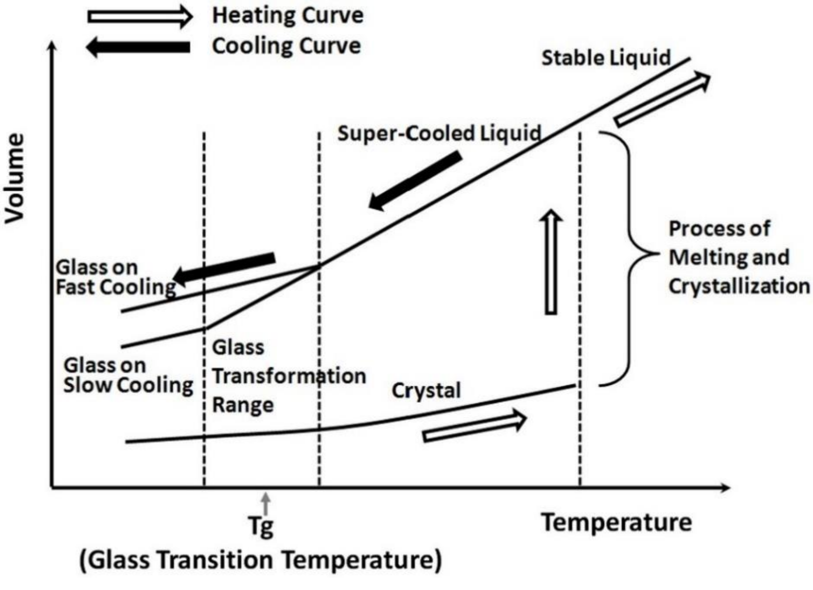

Figure 1. Volume changes in glass-forming systems during heating and cooling [53].

At T_g, glass has the properties of a solid elastic body with brittle fracture. Temperature T_f is the boundary between the plastic and liquid states. At T_f, it is already possible to draw thin strands from the glass mass.

The concepts of T_g and T_f were introduced by Tamman, but at that time it was not called the glass transition temperature [54]. The definition of T_g was proposed as a temperature at which a viscous liquid transition to a brittle state, or more simply – into a glassy state. The subscripts "g" and "f" are the first letters of "Glass" for glass and "Flissigkeit" for liquid in German [55]. In reality, this topic has been widely discussed and during the 20th century.

Tamman proposed another temperature, T_w, which denotes the temperature at which the property-temperature curve has a bend (w as in the German word "Windung" or "bend" - English). At that time, T_g was placed slightly before T_w, but the physicochemical connotation of the temperature was not explicitly stated, but it was briefly mentioned that between T_g and T_f there is a "transition interval" or "transition". Although he did not specify this transition region as the glass transition interval, it was later adopted and accepted by the scientific community. In general, as the temperature of a liquid decreases below its melting point, it usually undergoes a phase transition and becomes a solid with a crystalline structure. In contrast, inorganic glass liquids do not crystallize upon cooling, but rather develop a rigid, disordered network structure. This is due to the intricate molecular configuration of these materials and the slow transport processes that take place within them. An analogy with polymers can be drawn here, since glass can be considered to be polymeric in nature (e.g., as in the case of phosphate glasses [56,57]) - because it has a more or less chain-like structure with cross-linking, but with much shorter chain lengths. Another notable difference between crystalline materials is the melting point, in particular, the value of the melting point does not depend on the rate of temperature change or its direction (melting of a solid or freezing of a liquid), for glass it depends on both these conditions (see Figure 1) [58].

Glass properties are divided into three groups according to the type of change in the glass transition interval. The first group includes properties (P) characterizing the state function of substances (internal energy E, molar volume V, enthalpy H, entropy S) and kinetic properties (viscosity), specific resistance r). The properties of the first group change gradually with increasing temperature. In the glass transition interval, the curve has a rounded bend corresponding to the most abrupt change in the properties of the first group. The properties of the second group represent the first temperature derivative dP/dT of the properties of the first group (coefficients of thermal expansion-linear and volumetric, heat capacity). It can be seen that in the glass transition interval the first derivative dP/dT has an inflection point T_g. The third group includes properties (thermal conductivity, dielectric losses), which are the second derivatives of the state functions with respect to temperature. The temperature dependence d^2P/dT^2 has a maximum or minimum at point T_w [59,60].

The nature of changes in the properties of glasses upon heating is very different from the temperature dependence of the properties of crystalline materials. For the latter there is no division of properties into groups, the nature of temperature curves is uniform: insignificant linear change of properties up to melting point, sharp jump change of properties at melting point. The temperatures T_g, T_w, and T_f are always below the melting temperature of the corresponding crystal. The temperatures T_g, T_f and the glass transition (T_g - T_f) depend on the glass composition.

It can be seen that the volume of glass, unlike the volume of a crystalline substance, is not a constant for a given composition. It depends on temperature-time conditions of glass production. Isothermal tempering of tempered glass at temperature ($T < T_g$) is accompanied by a decrease in volume along the straight-line 1 t due to the tendency of the structure to reach an equilibrium state at temperature T. The time of structural rearrangement in the low temperature range is exceptionally long [59,60].

1.1.2. Structure of Different Glass Types

Silicate glass, as the name suggests, is formed from the basic component of silicon dioxide, often with other structural modifiers. Glass structure formers are the backbone of the interconnected network. In a pure silica glass, the structure is made up of repeating tetrahedral units of the oxygen network, with silicon in the center of this tetrahedron (the same structural trends could be said to apply to Ge glass). Although silica glass is made of a single repeating unit, its structure is much more complex, as there is still no complete or definitive description of the three-dimensional mid-range order first described by Zaccharisen [61].

Looking at the electronic structure of boron and oxygen, it should be obvious that in a glassy as well as in a crystalline structure, boron would form a triangular geometry with oxygen due to its sp2 hybridization. The majority of boron oxide triangles are contained in so-called boroxol rings. In boroxol rings each boron is coordinated by 3 oxygen atoms with a distance of 1:37 Å [62,63]. With the initial addition of network modifiers such as alkali oxides - up to a metal oxide/boron oxide ratio of 0.4 - boron oxide triangles are converted to boron tetrahedral units only [64]. Further increases in modifier concentration lead to the formation of at least one non-bridging oxygen formation per boron triangle. However, alkali borate glasses can contain several different ring structures in addition to boroxol rings, such as the pentaborate ring - B_5O_8, where a tetrahedral boron unit connects two six-membered rings, the triborate ring - a six-membered ring containing a tetrahedral boron, and diborate units - containing two trigonal boron units with three bridging oxygens and two tetrahedral borons with four bridging oxygens (see Figure 2) [65].

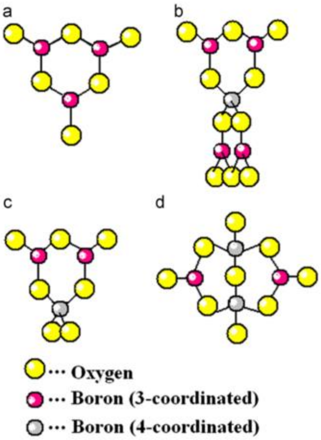

Figure 2. Four structural units of alkali borate glasses: a) boroxol ring, b) pentaborate ring, c) triborate ring, d) diborate unit [66].

However, by introducing additional oxygen atoms into the glass network, i.e., by incorporating silicon dioxide, structural rearrangement of boron oxide triangles into sp^3 hybridized tetrahedral units is induced. As an example, the ternary system Na_2O-B_2O_3-SiO_2 can be used to describe main principles of borosilicate glasses. The ratio of SiO_2:B_2O_3 and modifier (Na_2O) was used as a function to predict the fraction of boron atoms in tetrahedral coordination [67].

As can be seen from Figure 3, it is assumed that when $R<0.5$, the ternary glass-forming system behaves exactly like a binary one, i.e. with the addition of an alkaline metal ion, a single boron trigonal unit must be converted into a 4-coordinated one, regardless of the concentration of SiO_2. Predictions based on this model are relatively accurate in predicting trends in physical properties in such glasses, such as the coefficient of thermal expansion, which is directly proportional to the concentration of four-coordinated boron atoms, and the concentration of nonbonding oxygens of silicate groups. For other network modifying oxides, other than single charged alkaline metal ions, the role between this and charge compensation is much more complicated d [68,69]. The extent to which mixing of Si and B occurs depends largely on the exact composition of the glass. That is, in SiO_2-rich glass, B(IV) is most likely coordinated with four -O-Si- groups, whereas higher concentrations of B_2O_3 lead to the formation of -B-O-B- bonds, e.g., B(IV) is coordinated with one or more -O-B- units and three or fewer -O-Si- units [67].

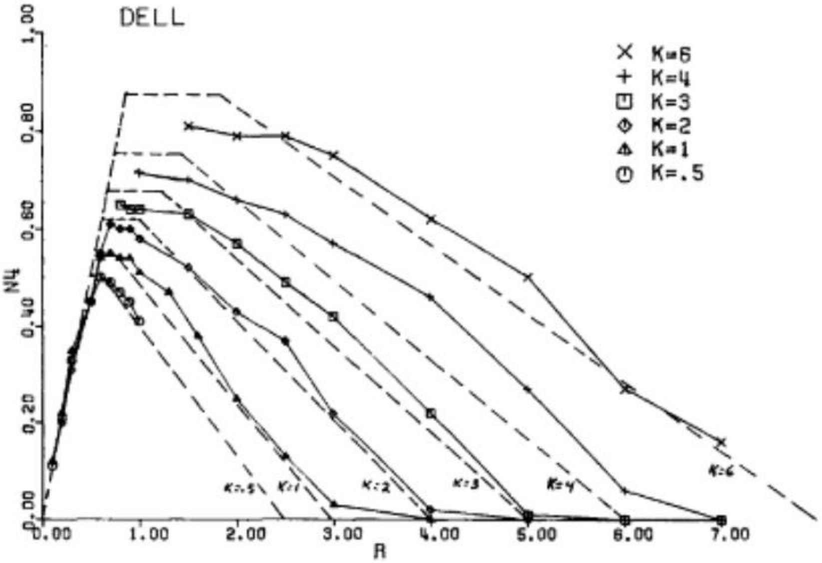

Figure 3. Graph of fourfold coordinated boron content dependence on glass composition. Where K depicts the ratio of SiO_2:B_2O_3 and N-4 – tetrahedrally coordinated boron fraction dependence on R (ratio of Na_2O:B_2O_3) [67].

The basic structural unit of quartz glass is a silica-oxygen tetrahedron. The silicon atom is surrounded by four oxygen atoms located symmetrically at the vertices of the imaginary tetrahedron.

The structure of silica glass is made up of SiO_4 tetrahedrons connected by oxygen atoms at the vertices. The result is a continuous spatial framework that differs from the geometrically regular lattices of crystal modifications of quartz by the lack of long-range order in the arrangement and orientation of the tetrahedrons. SiO_4 tetrahedrons do not form geometrically regular structural units in space in the form of six-part rings typical of the high-temperature cristobalite structure [70].

The structural lattice of glass looks like a distorted crystal lattice. The distortion consists in arbitrary variation of the values of the Si-O-Si bond angle between neighboring tetrahedrons in the glass structure.

The $[SiO_4]^{4-}$ group has an excess negative charge (-4), but the lattice of SiO_4 tetrahedrons is generally electrically neutral, since each oxygen atom is bonded to two silicon atoms. In the structure of fused silica, all oxygen atoms are bridged.

The structures of crystalline and vitreous forms of silica are not tightly packed because the tetrahedrons are connected by vertices, not edges or faces. Silica glass has free structural voids that are spatially bounded by bridging oxygen atoms. Because of the presence of free voids in the structure, silica glass has the highest gas permeability (helium, hydrogen, neon) compared to other silicate glasses, which contain alkali and alkaline earth metal oxides in addition to silica.

Where the alkali metal ions are aligned, there is no chemical bonding between the elements of the structure. The alkali ions are modifiers. As the concentration of Me_2O in the glass composition increases, the number of vacancies in the lattice and the number of non-bridging oxygen atoms per SiO_4 tetrahedron increases. At Me_2O concentrations greater than 60 mol%, conditions are created for the formation of isolated SiO_4 tetrahedrons. Such melts crystallize extremely rapidly because the conditions for reorientation of structural units are facilitated, whereas solidification of the melt as glass is complicated in this case. The regions of glass formation in binary alkali-silicate systems are continuous. In the system with Li_2O the content of limiting concentrations of SiO_2 is 100-64 mol%, with Na_2O 100-48 mol%, with K_2O 100-46 mol% [71–75].

Phosphate glasses are composed of $[PO_4]_3$ tetrahedra. One of the oxygen atoms of the tetrahedron cannot participate in the formation of bonds with other components of the structure due to the presence of a phosphorus-oxygen double bond. In the structure of phosphate glasses only three oxygen atoms of the phosphorus oxygen tetrahedron can be bridged.

In this respect, the structure of P_2O_5 differs from the structures of other glass formers in which all oxygen atoms are bridged. The spatial structure of phosphate glasses may consist of rings of different sizes formed by alternating phosphorus and oxygen atoms, ribbons or chains of RO_4 tetrahedrons.

The results of X-ray analysis show that the structure of double phosphate glasses is similar to that of double silicate glasses in two respects: the structural basic unit is the tetrahedral element-oxygen groups; the number of non-bridging oxygen atoms increases with the addition of modifying oxides [76–81].

According to the type of inorganic compounds, the following classes of glasses are distinguished: elemental, halide, chalcogenide, oxide, metallic, sulfate, nitrate, carbonate, etc. Elemental glasses can form only a small number of elements – sulfur [82–85], selenium [86–88], arsenic [89–91], phosphorus [92], carbon [93–96].

Glasses - sulfur and selenium, can be obtained by rapid supercooling of melt; arsenic - by sublimation in vacuum; phosphorus - when heated to 250 °C under pressure exceeding 100 MPa; carbon - as a result of continuous pyrolysis of organic resins. Of industrial importance is glassy carbon, which has unique properties exceeding those of crystalline carbon modifications: it can remain in the solid state up to 3700 °C, has a low density of about 1500 kg/m^3, high mechanical strength, electrical conductivity and chemical stability.

Halogenide glasses are produced on the basis of the glass-forming component BeF_2. Multicomponent compositions of fluoroberyllate glasses also contain fluorides of aluminum, calcium, magnesium, strontium, barium. Fluoroberyllate glasses find practical application due to high resistance to harsh radiation, including X-rays, and to such aggressive media as fluorine and hydrogen fluoride [97–100].

Chalcogenide glasses are produced in oxygen-free systems such as As-X (where X-S, Se, Te), Ge-As-X, Ge-Sb-X, etc. Chalcogenide glasses have high transparency in the infrared spectrum, possess electronic conductivity, and detect the internal photoelectric effect. Glasses are used in high-sensitivity television cameras, in electronic computers as switches or memory elements [101–103].

Oxide glasses are a large class of compounds. The oxides SiO_2, GeO_2, B_2O_3, P_2O_5 form glass most easily.

A large group of oxides are TeO_2, TiO_2, SeO_2, WO_2, Bi_2O_3 or for example, glasses are easily formed in the systems CaO-Al_2O_3, CaO-MgO-V_2O_3, P_2O_5-ZnO.

Each of the glass-forming oxides can form glasses in combination with intermediate or modifying oxides. Glasses are named according to the type of glass-forming oxide: silicate, borate, phosphate, germanate, etc. Glasses of simple and complex compositions belonging to silicate, borate, borosilicate, phosphate, germanate, aluminate, molybdate, tungstate and other systems are of practical importance [104–107].

The main advantage of glass technology is that it allows to obtain in the solid-state substances with non-stoichiometric proportions of components that do not exist in the crystalline state. Moreover, the properties of glasses can be smoothly adjusted in the desired direction by gradually changing the composition. Glasses based on nitrate, sulfate, and carbonate compounds are currently of scientific interest, but have not yet found practical application [108,109].

1.1.3. Glass Formers

It is well known that not all substances can be obtained in a glassy state. There is no certain class of substances, all representatives of which are able to give glass. Glass is made from a number of elements (e.g. P, Se, S), from oxides (SiO_2, B_2O_3, GeO_2, P_2O_5), from silicates, phosphates, fluorides, selenides, sulfoselenides and many complex compounds. The factors influencing glass formation are considered in the most detail for oxides. The list of major glass-forming oxides includes SiO_2, B_2O_3, GeO_2, P_2O_5. The elements that form these oxides are in a fairly narrow region of the periodic system. The bonding nature of the compounds of these elements is mixed (ionic and covalent), and their structures are usually a three-dimensional polymeric framework. Some other oxides also tend to form glass. For example, As_2O_3 and Sb_2O_3 change to the glassy state, but at very high cooling rates. There are oxides that do not form glass by themselves, but can form glass in the presence of other non-glass-forming oxides. For example, in the CaO-Al_2O_3 system, glass can be formed even though neither Al_2O_3 nor CaO in the glassy state. The most important condition for the formation of glass is the ability of the substance to form a continuous spatial three-dimensional network structure in which there is no long-range order. The first person to use crystallochemical approach to glass formation, Zachariasen, formulated a set of rules that oxides must meet in order to be glass-forming [61,110]:

1. Each oxygen ion must be bonded to no more than two positive ions of high charge and small ionic radius;
2. The number of oxygen ions surrounding the positive ion to form a polyhedron should be neither too many nor too few (3 or 4);
3. Adjacent oxygen polyhedra should be connected by common vertices, but not by edges or faces;
4. Each polyhedron should have at least three oxygen species in common with its neighbors, thus providing for the formation of a lattice structure.

These conditions are met by oxides of the type R_2O_3, RO_2, R_2O_5 with a cation radius not exceeding 0.055 nm. They are capable of forming a three-dimensional spatial lattice and are called glass formers. Oxides such as R_2O, RO and RO_3 do not meet these requirements and cannot produce glass by themselves, although they can form part of glass in the presence of glass formers. They are called modifiers.

The low coordination number of the oxygen atoms, equal to 2, contributes to the fact that the valence angles between the bonds of the oxygen atom, e.g. Si-O-Si, can change within a wide range without leading to the destruction of the tetrahedrons themselves. This contributes to the realization of a three-dimensional lattice structure without periodicity in the arrangement of the atoms [61].

Using these rules, Zachariasen predicted the tendency of oxides such as V_2O_5, Nb_2O_5, Ta_2O_5, Sb_2O_5, P_2O_3, and Sb_2O_3 to form glass. However, it was later discovered that there are a number of oxides that do not obey Zachariasen's rules, but from which glass can be obtained (e.g., WO_3, MoO_3). Although most glass-forming oxides meet these requirements, the class of glass-forming substances is much broader than Zachariasen's rules suggest [61].

Another theory was proposed by C. Sun, which states that glass-forming substances are predicted by the strength of a single cation-oxygen bond. For glass-forming oxides, the strength of such a bond is in the range of 80-120 kcal/mol (330-500 kJ/mol). These limits greatly increase the number of oxides that can form glass compared to the limits suggested by Zachariasen. As Sun notes, at bond strengths below 60 kcal/mol (250 kJ/mol) the oxides are unable to form glass, and at 60-80 kcal/mol (250-330 kJ/mol) they are intermediate (Table 1) [111].

Table 1. Calculated bond strength of oxide components [111]. “ “ – denotes assumed values.

M in MO_k	Valence	Dissociation energy per M_{Oz}, E_d (kilocalories)	Coordination No.	Single bond strength B_{M-O} (kilocalories
Glass formers				
B	3	356	3	119
Si	4	424	4	106
Ge	4	431 (?)	4	108
Al	3	402-317	4	101-79
B	3	356	4	89
P	5	442	4	111-88
V	5	449	4	112-90
As	5	349	4	87-70
Sb	5	339	4	85-68
Zr	4	485	6	81
Intermediate				
Ti	4	423	6	73
Zn	2	144	“2”	72
Pb	2	145	“2”	73
Al	3	317-402	6	53-67
Th	4	516	8	64
Be	2	250	4	63
Zr	4	485	8	61
Cd	2	119	“2”	60
Modifiers				
Sc	3	362	6	60

M in MO_k	Valence	Dissociation energy per M_{Oz}, E_d (kilocalories)	Coordination No.	Single bond strength $B_{M\text{-}O}$ (kilocalories
La	3	406	7	58
Y	3	399	8	50
Sn	4	278	6	46
Ga	3	267	6	45
In	3	259	6	43
Th	4	516	12	43
Pb	4	232	6	39
Mg	2	222	6	37
Li	1	144	4	36
Pb	2	145	4	36
Zn	2	144	4	36
Ba	2	260	8	33
Ca	2	257	8	32
Sr	2	256	8	32
Cd	2	119	4	30
Na	1	120	6	20
Cd	2	119	6	20
K	1	115	9	13
Rb	1	115	10	12
Hg	2	68	6	11
Cs	1	114	12	10

Winter-Klein developed a view of the importance of chemical bonding in the processes of glass formation. It is noted that the most important role in the formation of glass is played by bonding through p-electrons. All elements capable of forming a glassy lattice, have p-electrons in the outer electron shell, and simple glass, i.e. a lattice without foreign atoms, can be formed only the elements with four p-electrons in the outer shell [112].

According to the ideas of Winter-Klein, the behavior of elements during glass formation obeys the following rules [113]:

1. The ability to form glass is a periodic property of elements.

2. Group VI elements with s^2p^4 type outer shell are able to form simple glass (they have 4 p-electrons).

3. Group VI elements retain the ability to form glass in mixtures and compounds such as SeS, SO_2, etc.

4. The elements of the VI group are capable of forming glasses with the elements of the III-V group, whose outer electron shells are of the s^2p, s^2p^2 and s^2p^3 type, respectively.

5. Elements of the VII group with the s^2p^5 valence shell can also participate in the formation of a complex glass network.

According to A. Winter-Klein, without the participation of elements of groups VI and VII, glass cannot be formed at all, and substances that form glass must satisfy the following rule: the ratio of the sum of p-electrons to the number of atoms must be greater than 2. However, there are substances that satisfy this rule, but on the basis of which glass was not formed, for example, $AlPO_4$ [114].

It follows from the above that the formation of the structural lattice of glass depends primarily on the formation of interatomic bonds carried out by p-electrons. This ability is most pronounced in elements of group VI - s^2p^4. Next are the elements whose ability to form a structural lattice depends not only on the number of their own electrons, but also on the number of p-electrons that all other elements have in the lattice (elements of groups III, IV, VI and VII). Thus, in this case, the concept of a glass-forming oxide or element is replaced by the concept of a glass-forming bond formed by p-electrons.

Glass crystallization is a relaxation process, so this process is highly dependent on the rate of cooling. The crystallization of a supercooled liquid involves two stages: 1) nucleation of the crystal phase; 2) crystal growth. Favorable kinetic conditions for glass formation are low nucleation or crystal growth rates. If the nucleation rate is significant, the limiting stage of crystallization is the crystal growth stage. Conversely, for the crystal growth rate to be significant, there must be a very low nucleation rate in the system. Glass formation is most active when both rates are very low [108].

The cooling rate affects the properties of the final glass. As the temperature decreases, the mobility of the particles decreases and the rate of structural rearrangement to reach the equilibrium state at a given temperature slows. The high cooling rate "freezes" the high temperature state with increased molar volume or reduced density. The lower the cooling rate of the glass-forming melt, the closer the glass structure is to the "notional" equilibrium structure of the supercooled liquid.

1.1.4. Glass Synthesis Methods

To produce glass of defined composition, the first step is to carefully select the raw materials. Each of the glass batch constituents can typically be expressed either in terms of mass ratios of oxides or in terms of molar ratios. The batch precursors should contain solid particles of the smallest possible size to allow the most optimal mixing of the precursors, which in turn will ensure the lowest melting temperature, shortest melting times, and least interaction time with the crucible. Typically, many different chemical and physical reactions occur during glass melting, depending on the precursors used and the temperature program. The first type of reaction can be considered as dehydration or release of water from the precursor mixture, which can have several different origins: water intentionally added to aid mixing of raw materials, water adsorbed on the surface of materials, and hydrate water in the form of precursor crystallohydrates. The adsorbed water typically evaporates at about 100 °C, while that of hydrated precursors usually exceeds this temperature, e.g., sodium carbonate monohydrate loses water at about 109 °C [115]. At elevated temperatures, solid state reactions can begin. Interactions between alkali metal carbonates and alkaline earth metal carbonates tend to start at the lowest temperatures, forming double carbonates (1, 2) at temperatures around 300 °C to 900 °C [116], e.g.:

$$Na_2CO_3 + CaCO_3 \rightarrow Na_2Ca(CO_3)_2 \quad (1)$$

$$Na_2CO_3 + MgCO_3 \rightarrow Na_2Mg(CO_3)_2 \quad (2)$$

Although these types of reactions may thermodynamically proceed at lower temperatures, they are rate limited by the contact of interacting particles, surface area, and diffusion coefficients not only between precursors but also through the formed product layer.

Another type of reaction, the calcination reaction, occurs when carbonate salts begin to react with silica particles, usually by the formation of meta-silicates (3) or disilicates (4) [117]:

$$Na_2CO_3 + SiO_2 \rightarrow Na_2O \cdot SiO_2 + CO_2 \quad (3)$$

$$Na_2CO_3 + 2\ SiO_2 \rightarrow Na_2O \cdot 2\ SiO_2 + CO_2 \quad (4)$$

Two types of calcination reactions are often distinguished here - thermal calcination and reactive calcination. Thermal calcination occurs at temperatures above which carbonate salts begin to decompose, e.g.,

$$CaCO_3 \rightarrow CaO + CO_2 \quad (5)$$

Reactive calcination was mentioned in reactions 3, 4, which means that this type of calcination does not occur due to thermal decomposition of precursors, but due to solid-state reactions between different components, mostly limited by diffusion.

This is followed by the formation of eutectic phases, which greatly increase the diffusion coefficients between reactants due to the increased mobility through the product layer, while some of the formed eutectic phases can separate from solid particles, which in turn promotes further contact between solid reactant particles. However, liquid phase formation can occur not only between eutectic mixtures, but also through melting of the solid precursors, such as the melting of sodium carbonate that occurs at about 850°C. For example, a eutectic mixture of $Na_2O \cdot SiO_2$ and $Na_2O \cdot 2\ SiO_2$ has a eutectic point at 840 °C, but $Na_2O \cdot 2\ SiO_2$ and SiO_2 form a melt phase at

800 °C (Figure 4), even though the melting points of pure $Na_2O \cdot 2\ SiO_2$, $Na_2O \cdot SiO_2$ and SiO_2 are much higher (see Figure 4).

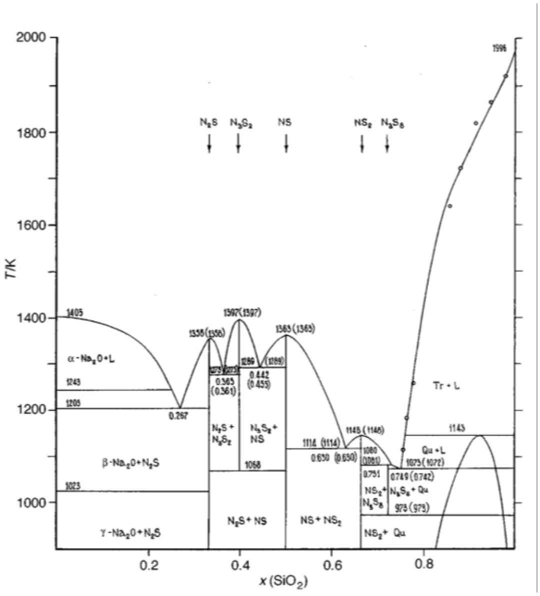

Figure 4. Phase diagram of Na_2O and SiO_2 [118].

As can be seen in the figure, the melting point of the eutectic mixture also shifts to lower temperatures with increasing SiO_2 content, whereas the viscosity of this system is greatly reduced by the increased Na_2O content, which means that the reactivity of the melt is reduced. The formation of the double carbonate salt also tends to have a lower viscosity than the silica melt phases, further increasing the reaction rate of the SiO_2 grains [118].

Because of the competing nature of two types of reactions, namely double carbonate formation and silica phase dissolution. At low heating rates, the silica pathway is thought to predominate, while at heating rates of hundreds of degrees per minute, the carbonate pathway dominates. The carbonate pathway proceeds through the formation of double carbonate (reactions 1 and 2), noting that triple carbonate ($Na_2CaMg(CO_3)_3$) is also possible. The alkaline nature of the phases formed is extremely reactive with silica phases, and the reaction proceeds with the release of CO_2. The silica pathway proceeds through the eutectic melt of sodium disilicate and silica phases. As the temperature increases, the melt continues to react with the remaining sodium carbonate, promoting the dissolution of SiO_2 as the temperature increases [119].

Since the double carbonate has a much lower viscosity and alkalinity towards SiO_2 particles, it is theorized that this leads to a much faster conversion of the precursor to a complete melt than the silica pathway.

At about 1200 °C, most of the precursor material is already present in the glass melt along with undissolved silica, alumina, and gas bubbles. With increasing temperature, the dissolution rate of the difficult to dissolve components also increase, which is the product of the complex relationship between melt viscosity and diffusion coefficient, and the increased solubility of the dissolving material, which is typically governed by heterogeneous reaction kinetics. Since the glass batch contains a large proportion of dissolved gases, including those in the form of bubbles, i.e., water vapor, N_2, CO_2, CO, O_2, SO_2, NO, Ar, and possibly others, immediately after the precursor conversion to melt. Since a low degree of dissolved gas removal can be one of the main reasons for a high number of defects in the final melt, a process called fining is of great importance [120,121].

Typically, fining is accomplished by adding small amounts of so-called fining agents (about 1% by weight) to the precursor batch. The fining agent acts through the production of fining gases, which are produced to aid in the removal of bubbles produced in each batch at the point of highest temperature of each melt. The decomposition of the fining agent increases the rate at which bubbles are produced, increasing the rate of their growth and removal to the surface. However, depending on the composition of the melt, several different fining agents with different mechanisms of action may be helpful. The most commonly used fining agents are sulfate salts or Na_2SO_4. Although the primary goal of sulfate addition is to fine scale the melt, it can also act as an oxidizer and promote the improvement of batch melting kinetics by improving the dissolution kinetics of hard-to-dissolve oxides. As mentioned above, the temperature at which fining begins depends largely on the reduction capabilities of the melt. In oxidizing melts, the main mechanism of sulfate fining is simple thermal sulfate decomposition (1430 - 1480 °C) [122,123]:

$$Na_2SO_4 \rightarrow Na_2O + SO_2 + \tfrac{1}{2} O_2 \qquad (6)$$

As can be seen from reaction No. 6, the fining gases in this case are SO_2 and O_2, but note that O_2 can also be incorporated into the melt structure as O^{2-} ions. A smaller portion may also react with SiO_2 before thermal decomposition begins, as shown in the reaction:

$$Na_2SO_4 + n\, SiO_2 \rightarrow Na_2O\cdot(SiO_2)_n + SO_2 + \tfrac{1}{2} O_2 \qquad (7)$$

This results in an earlier release of refining gases into the melt. Meanwhile, in a reducing precursor charge (e.g., containing CO, carbon, organic materials), some of the sulfate can be reduced to sulfide:

$$4\ CO + Na_2SO_4 \rightarrow 4\ CO_2 + Na_2S \qquad (8)$$

$$4\ C + Na_2SO_4 \rightarrow 4\ CO + Na_2S \qquad (9)$$

The reactions that produce sulfides can occur at relatively low temperatures of 700 - 800 °C, but they can also react with residual sulfates in the melt [122]:

$$S^{2-} + 3\ SO_4^{2-} \rightarrow 4\ SO_2 + 4\ O^{2-} \qquad (10)$$

The onset of these types of reactions is in the interval between 1000 °C and 1350 °C, providing a lower fining temperature in reducing melts. However, another route is the direct reaction of sulfates with reducing agents to produce fining gases:

$$C + 2\ Na_2SO_4 + m\ SiO_2 \rightarrow CO_2 + 2\ SO_2 + (Na_2O)_2\cdot(SiO_2)_m \qquad (11)$$

$$C + Na_2SO_4 + m\ SiO_2 \rightarrow CO_2 + 2\ SO_2 + (Na_2O)\cdot(SiO2)_m \qquad (12)$$

Although many reactions take place in a reducing melt, the only gas that provides sufficient fining is SO_2, whereas in an oxidizing matrix both SO_2 and O_2 can be present. If there is a large excess of reducing materials, even more complex reactions can occur [124]:

$$3\ Na_2S + Na_2SO_4 + x\ SiO_2 \rightarrow (Na_2O)_4\cdot(SiO_2)_x + 2\ S_2 \qquad (13)$$

The most important thing to note here is that the redox conditions of the resulting melt influence the mechanism of fining - the primary reaction temperatures, the competing reactions, and the extent to which they occur.

The halide fining mechanism is very different from sulfate fining due to the very limited solubility of halides in the melt. The most important parameters affecting which halide salts will begin to evaporate are melt temperature, composition, and most importantly, halide concentration in the melt. The solubility of halide salts in the melt decreases as the halide radius increases, which means that lower concentrations of NaI would be required compared to NaCl to achieve the same fining temperature range, but iodine and bromine emissions are strictly regulated compared to chlorine. However, there is a different risk with chlorine, as it can easily react with oxygen to produce corrosive HCl fumes, combined with much higher fining temperature requirements, which pose the greatest risk to furnace materials and crucibles if metal crucibles are used [125–127].

1.1.5. Phosphor in Glass and Other Ways to Get Luminescent Materials

Typically, phosphors in glass can be categorized into a few different types according to their composition, such as glass phosphors and glass-ceramics, which can also be classified according to their synthesis route: glass crystallization, low-temperature co-sintering and sol-gel method synthesis.

In the glass crystallization synthesis method, a glass of desired composition is first synthesized by melt quenching method and then thermally treated near its crystallization temperature, determined by differential scanning calorimetry, for a certain period of time to induce controllable crystallization of precursor materials. The most important step is the precipitation of the desired phases in the glass matrix and their combination with the optically active ions. A nucleation-growth approach is the most commonly used approach. Nucleation begins with the formation of nano-sized nuclei, where in the growth stage these nuclei form defined crystals also of nano- or micro-size. Schematically, these two stages can be visualized in Figure 5, where it can be seen that nucleation and growth rates pass through their maxima in different temperature ranges, although there is an overlap in the temperature interval where these processes can and do occur simultaneously.

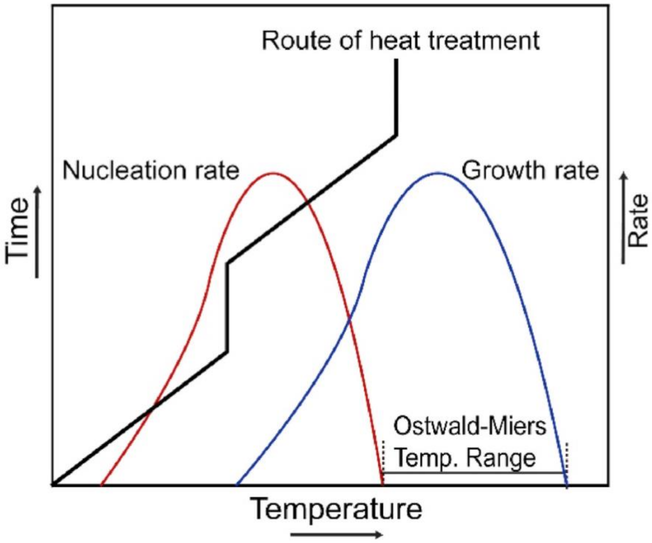

Figure 5. Schematic representation of nucleation (red line) and growth (blue rate) of glass ceramics as a function of temperature, where the black line represents the two-step growth treatment process [129].

Nucleation typically occurs at lower temperatures than growth. As a generalization, nucleation typically occurs at temperatures just above T_g, while crystal growth requires much higher temperatures close to T_c. The graphically visualized Ostwald-Miers temperature is sometimes referred to as the metastable supercooling range, which is used for nucleation growth that forms at the lower end of the temperature spectrum. For maximum control and separation of these processes, a two-step isothermal treatment route is used at two different temperature sets [128]. First, a low temperature is maintained for nucleation, which typically grows to 3 – 7 nm in size.

Another type of glass crystallization can be induced by phase separation by introducing different immiscible phases into the glass melt. Two types of phase separation can be observed, first at high temperature melting phase immiscibility and more often during melt quenching, but in most cases this can result in homogeneously distributed phases. Phase separation in this case occurs when network modifying cations compete with network forming cations for anionic linkers, most commonly - O^{2-}, which is related to the ionic potential - valence and radius ratio. It is known that the larger the ratio, the higher the tendency to phase separation (Cs < Rb < K < Na < Li < Ba < Sr < Ca < Mg) [130–133]. These phenomena can be explained by several mechanisms. First, the separation of different phases introduces more nucleation interfaces. Second, the greater mobility in ionic phases can increase the frequency of nucleation, and third, nucleating agents deliberately introduced into the separated phases can promote heterogeneous nucleation [134].

A low temperature co-sintering approach eliminates one of the most common problems with crystallized glass - the very limited number of available phosphors that can be crystallized from the precursor glass melt. The method is approached as a multi-step process in which a glass of desired composition is first synthesized by the typical melt quenching method. The resulting glass, called glass frit, is ground into a powder with as small a particle size as possible and mixed with the desired phosphor powder as homogeneously as possible. In the next step, there are two different approaches to the production of composite material as in how this co-sintering is applied. In the first approach, the glass frit powder and the phosphors are melted just above the glass melting temperature, i.e. the temperature is kept as low as possible to obtain the viscous flow of the glass, and then the melt is quenched as in the glass frit synthesis. It is important to note that there are several requirements for the glass to maintain phosphor luminescence in the final product. First, the melting temperature range of the glass should be as low as possible to prevent melting or decomposition of the phosphor material.

Second, it should have excellent chemical stability to ideally prevent or limit chemical reaction or dissolution of the phosphor in the glass melt. Third, it should have similar refractive indices of glass and phosphor crystals to minimize scattering at the phase interface of the materials.

A different approach can be used to partially circumvent the first two drawbacks of the phosphor and glass melt approaches. First, the synthesis of the composite is analogous to the melt approach, in that glass frit is ground to a small fraction of powder and thoroughly mixed with phosphor material. The resulting heterogeneous mixture is then pressed into pellets and sintered up to 80% of the glass melting point to induce sufficient kinetic energy for rearrangement of the glass structure, inducing reaction between the dangling surface bonds of the glass powders into a homogeneous structure, also incorporating phosphor crystals into the heterogeneous structure. This approach has several advantages because of the lower temperature used, which limits the degradation of the phosphor, as well as the much slower rates of dissolution into the matrix material. However, the major drawback is the micro-sized pores that can and do act as light scattering points. Despite this limitation, the main selling point of this synthesis method is the ability to incorporate different phosphor phases into a single pellet or other shape or product.

The sol-gel method typically involves condensation and hydrolysis of metal alkoxides in solution. The resulting xerogels are calcined to induce crystallization of the phosphor phase with some of the activator ions in the crystalline phase. However, another approach has been proposed by dispersing the phosphor phase directly into the sol-gel mixture at low temperature [135]. The xerogel is then also calcined at high temperature. This approach does not limit the phosphor phases to those that can be precipitated during the heat treatment step, which also has the disadvantage that only some of the activator ions precipitate together within the activator crystallites, which is especially true for rare earth ions. Overall, however, the sol-gel approach has several drawbacks, as it is difficult to produce large end products without cracking during solvent evaporation in the drying stage, and the resulting hydroxyl and carboxyl groups in the final glass composite severely limit its optical properties.

Luminescent properties in glasses are often achieved by incorporating specific dopants or additives into the glass matrix. These dopants introduce energy levels into the band gap of the glass, allowing for the absorption and subsequent emission of light. Common luminescent materials added to glasses include rare earth ions, transition metal ions, and organic or inorganic compounds. Here are a few examples:

1. Rare Earth ions: Dysprosium (Dy^{3+}), Europium (Eu^{3+}), Terbium (Tb^{3+}). These ions are commonly used for red, green and blue luminescence. They are widely used in phosphors for various applications [136].
2. Transition metal ions: Manganese (Mn^{2+}), Chromium (Cr^{3+}). These ions can be used to achieve different colors of luminescence in glasses. For example, Mn^{2+}-doped glasses can exhibit red luminescence [137].
3. Organic compounds: Fluorescent dyes. Organic compounds, such as fluorescent dyes, can be incorporated into glasses to impart luminescent properties. These are commonly used in display technologies and sensors [138].
4. Inorganic oxides:
    - Cerium Oxide (CeO_2): Cerium oxide is often added to glasses for its ability to act as a redox catalyst and modify the optical properties of the glass. It can influence the absorption and emission characteristics [139].
    - Neodymium Oxide (Nd_2O_3): Neodymium-doped glasses can exhibit laser properties in the infrared region. These glasses are used in various applications, including telecommunications [140].
    - Lanthanum Oxide (La_2O_3): Lanthanum oxide is sometimes added to glasses for optical and electrical applications. It can influence the glass transition temperature and other physical properties [141].
    - Titanium Dioxide (TiO_2): Titanium dioxide is a common dopant for glasses, imparting various optical and electrical properties. It can influence the refractive index and has applications in optics [142].
5. Garnet structure compounds:
    - Yttrium Aluminum Garnet: YAG is often widely used as a laser material, and its incorporation into glasses has been explored for optical applications [143].
    - Gadolinium Gallium Garnet: Gadolinium gallium garnet is another compound with garnet structure that has been studied for its optical properties. It is used in various optical devices [144].
    - Yttrium Iron Garnet: Yttrium iron garnet is a magnetic garnet structure compound that has been studied for its magneto-optical properties. Its incorporation into glasses is explored for magneto-optical applications [145].

1.2. Garnet Structure Phosphors

Garnet structure materials are one the most studied materials for optical applications. Yttrium aluminum garnet is probably the most extensively studied amongst the garnet matrix materials. It possesses an excellent chemical stability, wide band-gap, and one of the highest efficiencies of radiation conversion.

1.2.1. Garnet Structure

Garnet-type materials were initially identified as silicate minerals that are commonly used as gemstones. The most common structure in chemical notation can be written as $A_3B_2C_3O_{12}$. This structure was first described as early as 1917, in which almandite was identified as a space group in Schonfles's notation [146]. In 1929, the structure was identified as Ia-3d in different garnet minerals [147]. One of the most renowned or perhaps the most renowned synthetic garnet materials is $Y_3Al_5O_{12}$, or YAG, which has a multitude of applications in the field of optics. As the name implies, it is not found in nature. It was first synthesized and described as being in the garnet structural phase in 1951 [148]. However, in recent times it is known that not only aluminate but also gallate, germanate and other garnets can be synthesized not only that of silicate class. As can be seen in Figure 6 the A or c position as noted by Wyckoff [149] in the $A_3B_2C_3O_{12}$ structure, occupies dodecahedral sites (8-coordinate ones) with D_2 symmetry. In contrast, B(a) and C(d) represent cations in octahedral sites (6-coordinate ones) with S_6 symmetry. The unit cell is composed of eight formula units, or 160 atoms, distributed across three types of sites: octahedral (6-coordinate, S_6 symmetry), tetrahedral (4-coordinate, S_4 symmetry), and oxygen anions in tetrahedral positions.

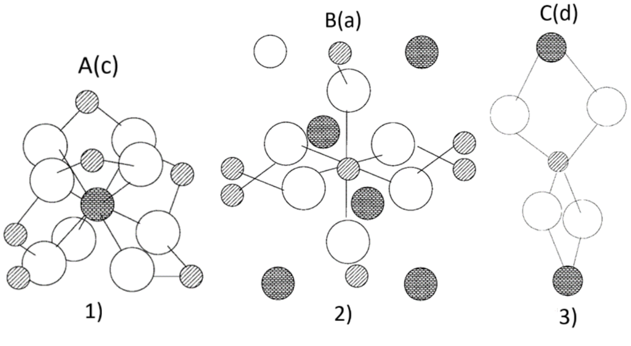

Figure 6. Schematic representation of cation sites in garnet structure, **1**) representing dodecahedral, **2**) octahedral, **3**) tetrahedral sites [151].

The ionic radius and valence states of cations or combinations of cations can be varied, but they are limited to the net neutrality of charge in the structure. As an example, the distances between Al^{3+}-O^{2-} in octahedral sites are 1.94 Å and 1.76 Å in tetrahedral ones [150]. The lattice constant for stoichiometric YAG is 12.000 ± 0.002 Å.

1.2.2. Synthesis of Garnet Structure Compounds

The most direct and straightforward approach is the solid-state reaction approach. As raw materials for the reaction, metal oxides and carbonates can be used; however, the most preferred salts are the nitrate salts. Thus, in a typical synthesis procedure, oxides and carbonates are first converted to nitrates by dissolving them in nitric acid, which is then evaporated slowly after the conversion to nitrate salts. During the synthesis process, a number of different phase formation cornerstones are typically observed, including YAG. These include $YAlO_3$ (YAP with perovskite structural unit), $Y_4Al_2O_9$ (YAM – monoclinic), and $Y_3Al_5O_{12}$ (YAG with cubic garnet structure). As demonstrated in the Y_2O_3–Al_2O_3 system, the reactions proceed initially through the formation of YAM, which is subsequently converted to YAG.

$$2\ Y_2O_3 + Al_2O_3 \rightarrow Y_4Al_2O_9\ (900 - 1100\ ^\circ C) \tag{14}$$

$$Y_2O_3 + Al_2O_3 \rightarrow 2\ YAlO_3\ (1100 - 1400\ ^\circ C) \tag{15}$$

$$Y_4Al_2O_9 + Al_2O_3 \rightarrow 4\ YAlO_3\ (1100 - 1400\ ^\circ C) \tag{16}$$

$$3\ YAlO_3 + Al_2O_3 \rightarrow Y_3Al_5O_{12}\ (1300 - 1600\ ^\circ C) \tag{17}$$

$$Y_4Al_2O_9 + Y_2O_3 + 4\ Al_2O_3 \rightarrow 2\ Y_3Al_5O_{12}\ (1300 - 1600\ ^\circ C) \tag{18}$$

It is postulated that YAG formation occurs via the solid-state diffusion of aluminum cations into the Y_2O_3 cubic structure. However, this reaction is thermally constrained by the high melting points of the considered oxides. To achieve the most homogeneous mixture possible, organic solvents could be added during the initial mixing stages of the precursor powder. The resulting batch is then treated at temperatures above 1500 °C for extended reaction times to obtain the garnet structure. To enhance the crystallinity of the desired phase or to facilitate the formation of smaller grain structures at lower temperatures, various fluxes, including H_3BO_3, BaF_2, Li_2CO_3, NH_4NO_3, SiO_2, YF_3, NaOH, and NaF, may be employed. Due to the nature of this process, repeated grounding of the resultant material and re-sintering is essential, since prolonged exposure to high temperatures can lead to a highly defective state. The high-temperature treatment time can vary greatly, ranging from a few hours to several days [152]. Some works also demonstrate that the precursor oxides can be found in the batch up until approximately 1600°C [153,154].

The sol-gel combustion method represents another synthesis route for the production of garnet-structured compounds. As with the typical sol-gel synthesis method, various oxides, salts such as nitrates, acetates, and others can be employed as metal ion sources. Additionally, metal alkoxides can be utilized, though this approach entails a more challenging and costly process. In the case of salt and/or oxide usage, water with added acid (i.e., HNO_3) typically acts as dispersant media. The next step in the process is the introduction of chelating agents such as citric acid, malic acid, ethylene glycol, and others. Here, different types of sol-gel processes can be differentiated. However, the most commonly used is the Pechini process, where nitrates act as starting materials. For the combustion process to propagate and be initiated, a fuel is required, which can be carbamide, glycerin, triethanolamine, and others. These must be dispersed within the reaction media. The most important parameters are temperature, the pH of the solution, the ratio of the complexing agent and metal cation, as well as fuel material concentration. The process is maintained at a temperature of 60 to 80°C while maintaining the pH of the solution between 2 and 5 to prevent precipitation. The duration of the process can be as low as 1 hour and extend up to 24 hours. At pH levels of <2, complexing agent ionization is severely inhibited, as observed in the case of yttrium aluminum garnet. However, maintaining the pH of the reaction solution at or above 5 may result in the formation of different phases or even precipitates that may be observed in the solution. However, the optimal ratio between the complexing agent and the other components is typically between 1 and 2. When the ratio is greater than 1, the complexing agent acts not only as the complexing agent but also as an additional fuel for the combustion reaction, which is necessary for the formation of optimal luminescence properties of the material. During the condensation step, the solution proceeds to a controlled gel formation if the pH and the temperature of the solution are kept within the controlled limits of the reaction. Subsequently, the gel is dried at temperatures between 100 and 150 °C for several hours or weeks, resulting in the formation of xerogel. However, it is important to exercise caution when using nitrates or nitric acid in the media, as various nitrogen oxides can be formed due to the decomposition of nitrates. When the process is carried out as a solid-state process, the primary combustion and pyrolysis reaction occurs during an intermediate thermal treatment at 200–600 °C for several hours. The decomposition of nitrates typically initiates at temperatures above 200°C, whereas carbonates require temperatures above 350°C to proceed towards the elimination of organics from the system. Following pyrolysis, the combusted gel must be reground and sintered at temperatures conducive to the formation of the desired material. Sintering can also be carried out in inert, oxidative, or reductive atmospheres to maintain or convert luminescent ions to the desired state. As a case study, YAG:Ce or YAG:Ce,Re can be employed for the proposed reaction processes:

$$(9–3x)\ Y(NO_3)_3 + 3x\ Ce(NO_3)_3 + 15\ Al(NO_3)_3 + 20\ C_6H_8O_7 \rightarrow 3\ Y_{3–x}Ce_xAl_5O_{12} + 120\ CO_2 + 80\ H_2O + 36\ N_2 \qquad (19)$$

$$(9–3x)\ Y(NO_3)_3 + 3x\ Ce(NO_3)_3 + 3y\ Re(NO_3)_3 + 15\ Al(NO_3)_3 + 20\ C_6H_8O_7 \rightarrow 3\ Y_{(3–x–y)}Ce_xRe_yAl_5O_{12} + 120\ CO_2 + 80\ H_2O + 36\ N_2 \qquad (20)$$

In contrast, the citrate reaction proceeds through a series of reactions, including the formation of citric acid and metal ion poly-chelates, followed by esterification with alcohol groups of organic compounds. For the acetate-nitrate-glycolate sol-gel process, the following reaction occurs:

$$M_2O_3 + 6\ CH_3COOH \rightarrow 2\ M(CH_3COO)_3 + 3\ H_2O \text{ (where: M=Y, Ce, co-dopant)} \qquad (21)$$

$$M(CH_3COO)_3 \rightarrow M^{3+} + 3\ CH_3COO^– \qquad (22)$$

$$M(NO_3)_3 \rightarrow M^{3+} + 3\ NO_3^– \text{ (where: M=Al, Y, Ce, co-dopant)} \qquad (23)$$

$$M^{3+} + 3\ H_2O \rightarrow M(OH)_3 \qquad (24)$$

$$2\ M(OH)_3 \rightarrow (HO)M(OO)M(OH) + 2\ H_2O \qquad (25)$$

$$2n\ (HO–CH_2–CH_2–OH) + n\ (HO)M(OO)M(OH) \rightarrow [–OCH_2–CH_2–O–M(OO)M–O–CH_2–CH_2–O–]_n + 2n\ H_2O \qquad (26)$$

During combustion, metal ions tend to act as oxidants, while complexing reagents act as reductants. This process provides the mixing of molecular compounds on a molecular level, but it is also very time-consuming due to the numerous stages involved.

1.2.3. Luminescence

The term "luminescence" was first coined in 1888 by German physicist Eilhardt Wiedemann in his book, which proposed the first definition of the phenomenon, although it was not technically accurate [155]. Wiedemann defined luminescence as the excess emission over and above the thermal emission background. He was also the first to classify luminescence into six classes that are still recognized today: photoluminescence, electroluminescence, chemiluminescence, thermoluminescence, triboluminescence, and crystalloluminescence. Photoluminescence is excited by electromagnetic radiation and is also subdivided into fluorescence and phosphorescence. Electroluminescence occurs in the gaseous state and is excited in electrical fields. Chemiluminescence presents itself with the release of energy during a chemical reaction. Thermoluminescence, however, is a distinct phenomenon that should not be confused with the aforementioned forms of luminescence. With thermal excitation, a stimulated luminescence occurs when a solid material is heated after being excited in some other way. Triboluminescence and crystalloluminescence are similar phenomena, occurring when crystals are mechanically crushed or broken, and when solutions crystallize or solid materials crack while growing, respectively.

A diverse array of materials, including metal oxides, silicates, phosphates, and sulfides, exhibit luminescence properties. In certain instances, bulk materials lack luminescence, necessitating the addition of activators. These activator ions form luminescence centers where excitation-emission processes occur when surrounded by host-crystal ions. Only a trace of these ions should be doped, and the distribution of activator ions must be as regular as possible, since in high concentrations activators inhibit luminescence. Transition metal ions, as well as various lanthanides, are usually used as activators. All 15 lanthanides, from lanthanum to lutetium, in addition to scandium and yttrium, have been used as activators in various hosts. They are described by an incompletely filled 4f orbital, which is shielded by $5s^2$ and $5p^6$ filled shells, giving rise to a narrow and sharp lines in the emission spectra of transitions within 4f configuration [156]. In contrast, the emission spectra contain broad bands when a 5d-4f transition occurs, since 5d electrons are unshielded and heavily influenced by their surroundings. The emission lifetimes of a given transition depend on its origin. For instance, f-f transitions are considered to be long-lived, with lifetimes in the range of milliseconds. In contrast, 5d-4f transitions have much faster lifetimes, with a typical value of approximately 10-5 s [157]. Of all the lanthanides, Er^{3+}, Yb^{3+}, Tm^{3+} and Eu^{3+} ions are considered to be the most commonly used activators. The second most commonly used elements as luminescence centers are transition-metal ions, which have incompletely filled d orbitals (d^n, where n varies from 0 to 10). In comparison to lanthanides, the 3d orbitals are not shielded from the host lattice, which can influence the optical properties. The emission spectra of transition metal ions exhibit broad and undefined features due to the strong coupling between electronic and vibrational transitions of the host lattice. For the most part, transition metal ions with three electrons in the d shell (e.g., Cr^{3+} and Mn^{4+}) or five electrons (e.g., Mn^{2+} and Fe^{3+}) are employed in phosphors. Other transition metals, such as vanadium, cobalt [158], nickel, copper, and cadmium [159], can also be employed as activators.

1.2.4. Group B Elements Doped Garnets

The chemical composition of the garnet host determines the suitability of the aforementioned transition metals as activators [160–164]. The garnet structure doping with transition metals results in the appearance of broad luminescence bands in the visible and near-infrared regions, as well as long-persistent luminescence and photochromism [164]. These properties have the potential to be applied in the development of luminescent thermometers [161,163] and high-power W-LEDs [165].

In order to predict possible electromagnetic absorptions in UV, visible or IR spectrum of transition metal, two different types of diagrams, called Orgel and Tanabe-Sugano, are used. The main difference between these diagrams is that Orgel diagrams can be used only for high spin complexes, while Tanabe-Sugano diagrams can be used for both high spin and low spin complexes. Tanabe-Sugano diagrams show how the strength of the octahedral ligand field depends on the positions of the different energy level components resulting from the splitting of the degenerate free ion states of transition metals. This diagram can also be used in luminescence spectra of transition metals in inorganic solid-state matrices, where the dominant external force is the crystal field [166]. In the garnet structure, the transition metal occupies sites with six oxygen ions as nearest neighbors, resulting in a coordination sphere known as a distorted octahedron.

The Tanabe-Sugano diagram can be used to interpret the emission spectra of YAG doped with Cr ions, since the optical properties of Cr^{3+} ions are directly dependent on the strength of the crystal field surrounding the host lattice. It should be noted that yttrium aluminum garnet is not a phosphor and does not produce luminescence by itself, but acts as a host. The effects of Cr^{3+} doping on the photoluminescence properties of YAG have been previously reported by various authors [167–172]. T. Xu et al. [171] showed that the optical transmittance spectra of Cr^{3+}-doped YAG single crystals contained two absorption bands located at 430 and 600 nm, which were assigned to $^4A_2 \rightarrow {}^4T_1$ and $^4A_2 \rightarrow {}^4T_2$ optical transitions. When YAG:Cr was excited with different wavelengths in the 430-600 nm range, the photoluminescence emission spectra contained a broad band in the 620-800 nm range with a sharp peak at 688 nm, which was attributed to either $^4T_2 \rightarrow {}^4A_2$ [167,169,171] or $^2E \rightarrow {}^4A_2$ [168,170,172] transitions. In order to successfully grow a plant, the photophysiological processes must be met, and this requires light in three separate spectral regions: far-red (700-760 nm), red (620-680 nm), and blue (400-500 nm) [173], and for this application, chromium-doped YAG is a perfect candidate.

1.2.5. Lanthanide Doped Garnets

Lanthanide doped garnets, in particular yttrium aluminum garnet, have proven successful for commercial applications over the past few decades. For example, Ce^{3+}-activated YAG has been widely used as a yellow phosphor in white LEDs [174–176]. The emission spectra for this material show a broad yellow emission band, and this phosphor has an external quantum efficiency of 87% and its optical absorption of 95% under blue light excitation [176]. Moreover, Nd^{3+} doped YAG is one of the most widely used solid state lasers which can be available in different forms like continuous, normal pulsed as well as Q-switched [177].

For solid-state phosphors, two selection rules can be highlighted: the spin selection rule (which forbids electronic transitions between levels with different spin states) and the parity selection rule (which forbids electric-dipole transitions between levels with the same parity; for example, electronic transitions cannot occur within the d-shell, within the f-shell, and between the d- and s-shells). Considering phosphors containing rare earth elements, two different types of optical transitions can occur, namely 4f-5d and charge transfer transitions [178]. The type of transitions allowed depends on the rare earth ion charge: divalent ions (Sm^{2+}, Eu^{2+}, Yb^{2+}) show 4f-5d transitions, trivalent ions (Sm^{3+}, Eu^{3+}, Yb^{3+}) show charge-transfer absorption bands in the ultraviolet, while tetravalent ions (Ce^{4+}, Pr^{4+}, Tb^{4+}) show charge-transfer absorption bands in the visible. In addition, emission for rare earth ions can arise from intraconfigurational 4f transitions, which are parity forbidden and only partially allowed due to the mixing of opposite parity wave functions [157]. The possible transition of the most commonly used rare earth ions is shown in Figure 7.

Some rare earth ions show broad emission bands that can be related to 4f-5d transitions. Ce^{3+} ions are one of the simplest examples, since it contains only one electron in the f-shell. The excited configuration for this cation is $5d^1$. The $4f^1$ ground state configuration gives rise to two levels, $^2F_{5/2}$ and $^2F_{7/2}$, which are separated by about 2000 cm^{-1} due to spin-orbit coupling. The $^5d_1$ configuration is split into 2 to 5 components and the total splitting is 15000 cm^{-1}. The emissions come from the lowest component of the $5d^1$ configuration to the two levels of the 4f ground state, giving a typical double-band shape. A completely different situation can be observed for rare earth elements containing more than one electron in the f-shell, for example Eu^{3+}, which shows a superior red emission around 616 nm. The host with Eu^{3+} ions as activator contains 5 characteristic bands corresponding to $^5D_0 \rightarrow {}^7F_j$ transitions (j = 0, 1, 2, 3 and 4), which can be seen in Figure 7. Moreover, the luminescence for this ion also depends on the host lattice, and when Eu^{3+} is located at a site of inversion symmetry, the electric dipole transition $^5D_0 \rightarrow {}^7F_2$ is forbidden [177,180].

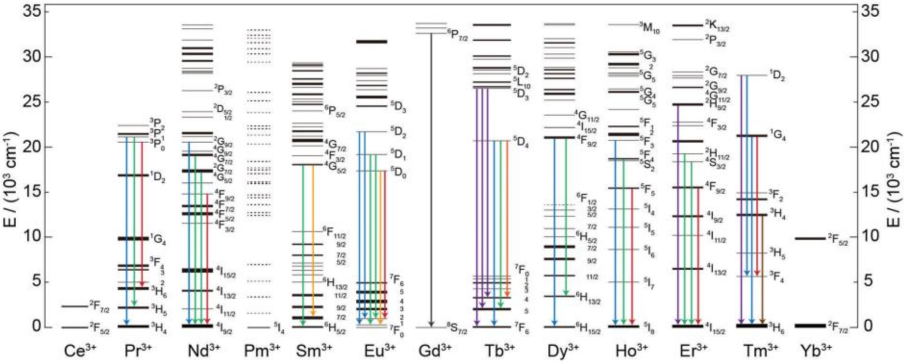

Figure 7. Partial energy level diagram of lanthanide ions, which commonly used to achieve upconversion emission [179].

1.2.6. Magnetic Garnets

Yttrium iron garnet (YIG) is a soft ferrite material with a cubic structure. In this compound, individual ions occupy three distinct sites: the dodecahedron (filled specifically with Y^{3+} ions), the tetrahedron (filled with three Fe^{3+} ions), and the octahedron (where two Fe^{3+} ions reside). Antiparallel iron ions in separate positions cause superexchange interactions. The magnetic moment for this garnet is a result of the excess of Fe^{3+} ions in tetrahedral position, as other two iron ions in tetrahedral position have their magnetic moment canceled by two iron ions in octahedral position [181]. While the bulk sample has ferrimagnetic properties, nanocrystalline YIG powders have shown superparamagnetic properties with a decrease in saturation magnetization as the particle size decreases [182]. This material also exhibits a narrow resonance line width in the microwave region, low dielectric loss [183], which makes it applicable to the fabrication of oscillators, isolators, memory devices, tuning filters, delay lines [184].

The preparation of phase-pure YIG is a rather difficult task. Conventionally, this material is synthesized by solid state route using high temperature of 1450 °C and long soaking time of 10 h [185]. Other methods such as sol-gel [186], co-precipitation [187], surfactant assisted solid-sate [188], sol-gel autocombustion [189], microwave-assisted hydrothermal [190] are among the few methods that have been used for the preparation of yttrium iron garnet. These synthetic approaches allowed lower formation temperature varying in interval of 800-1050 °C, shorter synthesis time and in all cases monophasic garnets were obtained. Many different variations of the sol-gel method have been reported for YIG preparation, since it allows lower processing temperature, homogenization of starting materials at the atomic level, and use of precursors that do not produce impurity phases.

Another way to lower the synthesis temperature and the alternating magnetic properties is to dope YIG with different cations at both sites. For example, when Y^{3+} ions are exchanged with different rare earth elements in the dodecahedral position, this can lead to an increase in anisotropy [191] or a decrease in remanence and saturation magnetization when Sm^{3+} or Gd^{3+} ions are introduced [192,193]. Iron substitution with Al [194], Mn [195], Ga [196] has been shown to improve magnetic properties for shifter applications.

2. EXPERIMENTAL PART

2.1. Materials

2.1.1. Reagents for Glass Synthesis

Ammonium dihydrogen phosphate, $NH_4H_2PO_4$ (anhydrous, pure p.a., Firma Chempur CAS # 7722-76-1), boron oxide, B_2O_3 (98% - 40 mesh, ACROS ORGANICS, CAS #: 1303-86-2), silicon dioxide, SiO_2 (highly dispersed, Merck CAS # 7631-86-9), calcium oxide, CaO (p.a., Reachem s.r.o., CAS # 1305-78-8), sodium hydrocarbonate, $NaHCO_3$ (p.a., Reachem s.r.o., CAS #: 144-55-8), zinc oxide, ZnO (p.a., Reachem s.r.o., CAS #: 1314-13-2), lithium hydroxide, $LiOH·H_2O$ (pure p.a., Firma Chempur, CAS #: 1310-66-3), barium oxide, BaO (extra pure, ACROS ORGANICS, CAS #: 1304-28-5), potassium hydrogen carbonate, $KHCO_3$ (99%, Alfa Aesar, CAS #: 298-14-6), tin(II) chloride, $SnCl_2$ (anhydrous, pure p.a., Firma Chempur, CAS #: 7772-99-8), aluminum oxide, Al_2O_3 (p.a., Reachem s.r.o., CAS #: 1344-28-1), magnesium oxide, MgO (p.a., Reachem, CAS #: 1309-48-4), europium(III) oxide, Eu_2O_3 (99,99%, Alfa Aesar, CAS #: 1308-96-9), cerium(III) nitrate hexahydrate, $Ce(NO_3)_3·6\ H_2O$ (99,99%, Alfa Aesar, CAS #: 10294-41-4).

2.1.2. Reagents for Yttrium Iron Garnet Synthesis

Iron (III) nitrate nonahydrate, $Fe(NO_3)_3·9\ H_2O$ (98.0%, Duro-Galvanit-Chemie, CAS #: 7782-61-8), yttrium (III) nitrate hexahydrate, $Y(NO_3)_3·6\ H_2O$ (99.8%, Sigma-Aldrich, CAS #: 13494-98-9), lanthanum (III) nitrate hexahydrate, $La(NO_3)_3·6\ H_2O$ (99.8%, Sigma-Aldrich, CAS #: 10277-43-7), cerium (III) nitrate hexahydrate, $Ce(NO_3)_3·6\ H_2O$ (99.8%, Sigma-Aldrich, CAS #: 10294-41-4), praseodymium (III) nitrate hexahydrate, $Pr(NO_3)_3·6\ H_2O$ (99.8%, Sigma-Aldrich, CAS #: 15878-77-0) and neodymium (III) nitrate hexahydrate, $Nd(NO_3)_3·6\ H_2O$ (99.9% Merck, CAS #: 16454-60-7), nitric acid, HNO_3 (65%, Eurochemicals, CAS #: 7697-37-2), ethylene glycol 1,2-ethanediol $C_2H_6O_2$ (99.5 %, Aldrich, CAS #: 107-21-1).

2.1.3. Reagents for Yttrium Aluminum Garnet Synthesis

Aluminum nitrate nonahydrate $Al(NO_3)_3·9\ H_2O$ (≥98 %, Carl Roth, CAS #: 7784-27-2), yttrium nitrate hexahydrate $Y(NO_3)_3·6\ H_2O$ (99.9% , Alfa Aesar, CAS #: 13494-98-9) and chromium nitrate nonahydrate $Cr(NO_3)_3·9\ H_2O$ (≥99.99%, Sigma Aldrich, CAS #: 7789-02-8), nitric acid solution (65%, Chempur, CAS #: 7697-37-2), ethylene glycol 1,2-ethanediol $C_2H_6O_2$ (g.r., lachner, CAS #: 107-21-1).

2.2. Methods

Three different series of materials and their syntheses have been studied. In the first part, different types of phosphate glasses were doped with europium and cerium ions by the most widely used melt quenching method. In the other two, garnet-type materials were synthesized, more precisely, yttrium iron garnet doped with several lanthanides and yttrium aluminum garnet doped with chromium ions, which showed remarkable luminescence properties not previously reported in the literature.

2.2.1. Glass Synthesis Methods

Phosphor glass samples were prepared via a conventional melt quenching method. The precursor materials were weighed according to the theoretical glass compositions (see Table 2 and Table 3) as to make the final mass of the glass 2 g.

Table 2. Initial glass compositions expressed in mol % for corresponding element oxides. The glasses were additionally doped with 0.2%, 0.6%, and 1.0% of Eu^{3+} based on their initial compositions

Sample name	P_2O_5 mol %	Na_2O mol %	K_2O mol %	Li_2O mol %	CaO mol %	Al_2O_3 mol %	ZnO mol %	B_2O_3 mol %	SiO_2 mol %	SnO mol %
G1	50	–	15	10	10	2	10	2	–	1
G2	43	42	–	–	–	–	15	–	–	–
G3	45	34	–	–	5	–	10	5	1	–
G4	45	28	–	6	1	4	10	5	1	–
G5	45	28	–	6	4	1	10	5	1	–
G6	43	–	42	–	–	–	15	–	–	–

These mixtures were ground in an agate mortar for a minimum of 30 minutes, transferred to porcelain crucibles, and melted at 900 °C in a muffle furnace for a duration of one hour at an ambient atmosphere. To reduce the occurrence of internal stresses, the resulting melt was poured into preheated brass molds, annealed from 300 to 400 °C for 30 minutes, and then cooled to room temperature.

Table 3. Different glass compositions doped with 3% YAG:Ce^{3+}

Sample name	P_2O_5 mol %	Na_2O mol %	K_2O mol %	Li_2O mol %	CaO mol %	Al_2O_3 mol %	ZnO mol %	B_2O_3 mol %	SiO_2 mol %	SnO mol %
C1	57.5	–	–	2	–	–	38	–	–	2.5
C2	45	28	–	6	1	4	10	5	–	1
C3	50	–	15	10	10	2	10	2	–	1
C4	50	10	5	10	10	1	10	2	–	2
C5*	45	30	–	3	10	–	3	6	2	–
C6	45	34	–	–	5	–	10	5	1	–

*Contains 1 mol % of La_2O_3

2.2.2. Synthesis of Yttrium Iron Garnet Doped with Rare Earth Metals

A conventional aqueous sol-gel method was employed for the synthesis of lanthanum, cerium, praseodymium and neodymium-substituted yttrium iron garnet ($Y_3Fe_5O_{12}$; YIG). Nitrate salts of various elements (iron (III) nitrate nonahydrate, $Fe(NO_3)_3 \cdot 9\ H_2O$, yttrium (III) nitrate hexahydrate, $Y(NO_3)_3 \cdot 6\ H_2O$, lanthanum (III) nitrate hexahydrate, $La(NO_3)_3 \cdot 6\ H_2O$, cerium (III) nitrate hexahydrate, $Ce(NO_3)_3 \cdot 6\ H_2O$, praseodymium (III) nitrate hexahydrate, $Pr(NO_3)_3 \cdot 6\ H_2O$ and neodymium (III) nitrate hexahydrate, $Nd(NO_3)_3 \cdot 6\ H_2O$ according to their stoichiometric ratios in the theoretical compositions of substituted garnets were dissolved in 20 mL of deionized water. Concentrated nitric acid, HNO_3 (65% Eurochemicals) was added drop by drop to the resulting mixture until the pH of the solution reached approximately 1, after which the mixture was stirred for 1 h. A stoichiometric amount of ethylene glycol was added to the reaction vessel (keeping ethylene glycol to metal ion ratio 2:1), the vessel temperature was raised to 80 °C, covered with watch glass and stirred for another 2 h. The resulting gel was placed in a 150 mL tube. The resulting gel was placed in a 150 °C oven and dried for 24 h. The formed xerogel was ground in an agate mortar and powders were placed in a covered porcelain crucible and annealed at 1000 °C for 5 h at a heating rate of 5 °C/min.

2.2.3. Synthesis of Yttrium Aluminum Garnet Doped with Chromium

The chromium-doped yttrium aluminum garnets were synthesized using the sol-gel method. A stoichiometric amount of $Al(NO_3)_3 \cdot 9\ H_2O$, $Y(NO_3)_3 \cdot 6\ H_2O$ and $Cr(NO_3)_3 \cdot 6\ H_2O$ was dissolved in 20 mL of deionized water to which 65% nitric acid solution was added drop by drop up until pH reached approximately ~1 while stirring at room temperature for 30 minutes. A stoichiometric amount of ethylene glycol was then added to the reaction mixture to keep the total molar ratio of metal ion to ethylene glycol (1:2) constant between different samples. The gel preparation vessel was covered with a watch glass and stirred at 80 °C for 1 hour. The resulting gel was placed in a furnace at 150 °C and consequently dried for 24 hours. As formed xerogel was ground in an agate mortar transferred to a ceramic crucible and annealed at 1000 °C for 5 hours, after which it was reground and analyzed using various techniques.

2.3. Characterization Equipment

For crystalline phase identification of glass samples at ambient temperature the XRD data were collected at 10 – 70°, 2θ angle range (scanning speed of 10°/min) using Ni-filtered Cu radiation on Rigaku MiniFlex II diffractometer. For the characterization of Yttrium Iron Garnet Doped with Rare Earth Metals the data were collected at 10 – 80°, 2θ angle range (Bragg–Brentano (θ/2θ) geometry, scanning speed of 5°/min) using Ni-filtered Cu_{α} radiation.

Raman spectra were recorded using inVia Raman (Renishaw, United Kingdom) spectrometer equipped with thermoelectrically cooled (–70 ^{o}C) CCD camera and microscope. Raman spectra were excited with 785 nm beam from the diode laser (Renishaw, UK). The laser power at the sample was restricted to 3 mW. The 20x/0.40 NA objective lens and 1200 lines/mm grating were used to record the Raman spectra. The overall integration time was 50 s. Position of the Raman bands on the wavenumber axis was calibrated by the polystyrene film standard spectrum. Parameters of the bands were determined by fitting the experimental spectra with Gaussian-Lorentzian shape components using GRAMS/A1 8.0 (Thermo Scientific, USA) software.

SEM and EDX images were taken for the description of morphology and characterization of surface composition by using Hitachi TM3000.

For the characterization of luminescent glass spectra were recorded on Edinburgh Instruments FLS980 spectrometer equipped with a 450 W Xe arc lamp, cooled (−20 °C) single-photon counting photomultiplier (Hamamatsu R928). The photoluminescence emission spectra were corrected by a correction file obtained from a tungsten incandescent lamp certified by the National Physics Laboratory (UK). The excitation spectra were corrected with a reference detector. During the recording emission and excitation spectra, the spectral width of the emission slits was set to 0.5 nm and the excitation slits to 0.3 nm, the step size (for excitation and emission) being 0.5 nm and the integration time - 0.2 s. For the characterization of Yttrium Aluminum Garnet Doped with Chromium, during the recording emission and excitation spectra, the spectral width of the emission slits was set to 0.5 nm and the excitation slits to 1.25 nm, the step size (for excitation and emission) being 1.0 nm and the integration time - 0.2 s.

For the characterization of Yttrium Iron Garnet Doped with Rare Earth Metals the vibrating sample magnetometer consisting of laboratory magnet, the lock-in amplifier SR510 (Stanford Research Systems), the gauss/teslameter FH-54 (Magnet Physics), and the power source SM 330-AR-22 (Delta Elektronika) was applied for the magnetization measurements. Mössbauer spectrometer (Wissenschaftliche Elektronik GmbH) in transmission geometry using ^{57}Co (Rh matrix) source was applied to collect spectra at room temperature and elevated temperature with special Mössbauer furnace. The Mössbauer spectra were fitted to sextets using WinNormos Site software. Isomer shifts are given relatively to α-Fe at room temperature.

Bruker Alpha FT-IR spectrometer was used for FT-IR analysis of compounds. All transmittance spectra were recorded at ambient temperature in the range of 4000–400 cm^{-1}.

2.4. Synthesis and Characterization of Europium Doped Glasses

2.4.1. X-Ray Characterization of Glasses Goped with Europium

X-ray diffraction studies were performed to investigate whether the glass has crystallized after the rapid cooling of the melt. The XRD patterns of the undoped samples in

Figure *8* indicate no defined peaks which could be attributed to any crystalline phase formation in glass samples. The high intensity baseline also suggests about amorphous nature of the samples. Exclusively, only undoped G1 sample, analyzed by XRD, exhibits a single low-intensity and well-defined diffraction maximum at 2Θ = 22.28 which could be attributed to a rarely recurring crystallization of tin pyrophosphate (SnP_2O_7, PDF: 00-029-1352) (Figure 8).

The XRD patterns of doped samples are presented as a supplementary file (Appendix 3). Note, 1% europium doped G1 sample does not exhibit crystalline phase. Since glasses are amorphous materials, an additional technique is needed to identify their structure.

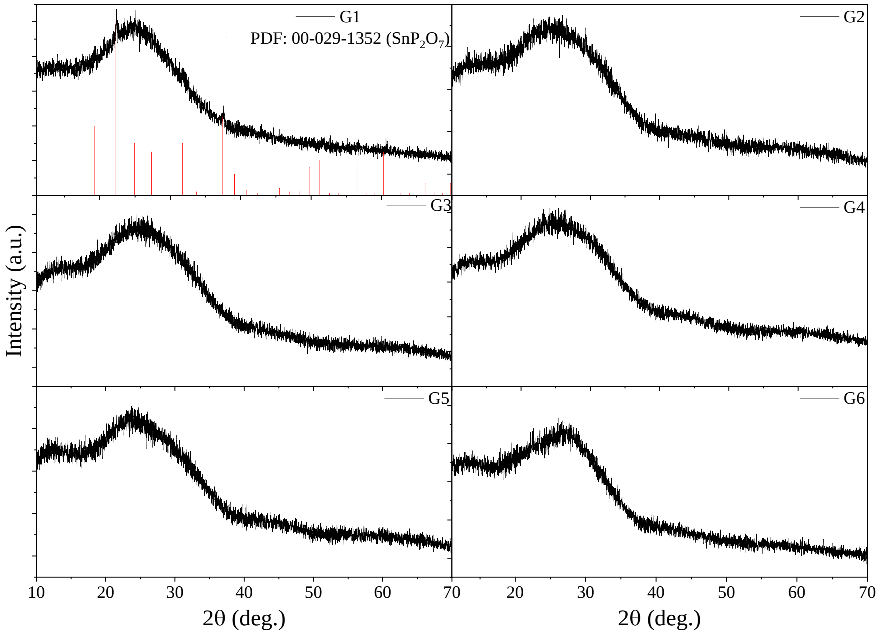

Figure 8. XRD patterns of different undoped glass compositions.

2.4.2. Raman Characterization of Phosphate Glasses without Europium Ions

Raman spectroscopy is able to provide detailed information on short-range molecular structure or local symmetry. The main structural elements of phosphate glasses are P−O−P network and various structure PO_n groups. Based on the number of bonded oxygen atoms in the phosphate group four phosphate tetrahedral sites were recognized (Figure 9) [197–199].

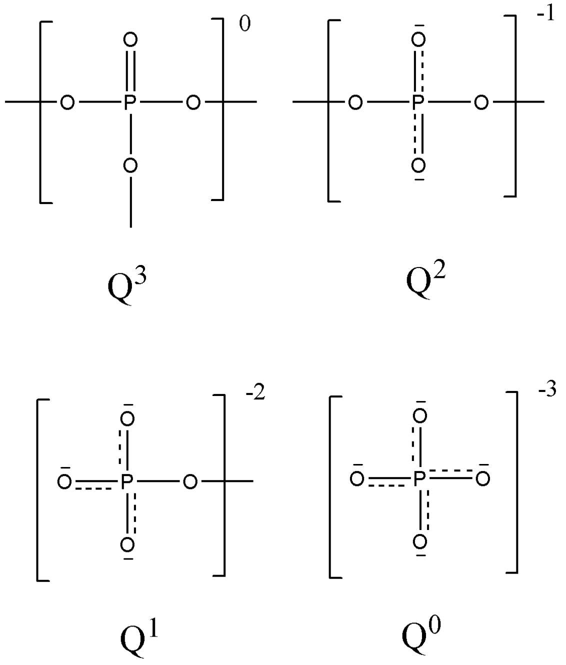

Figure 9. Tetrahedral phosphate sites in glasses.

Q^0 site is composed of $(PO_4)^{3-}$ structure with no oxygen atoms bounded to phosphate network, Q^1 site is composed of $[-(O)PO_3]^{2-}$ structure with one oxygen atom bound to phosphate network, Q^2 site is composed of $[-(O)_2PO_2]^-$ structure with two oxygen atoms bound to phosphate network, and Q^3 site is composed of $[-(O)_3PO]$ structure with three oxygen atoms bound to phosphate network. Raman spectra of different composition undoped phosphate glasses (Table 2) are displayed in Figure 10. The intense and relatively broad feature visible in the high frequency range at 1291−1305 cm^{-1} for samples G1−G6 belongs to symmetric stretching vibration of terminal P=O group in Q^3 tetrahedral structure, $\nu_s(P=O)$ [197] with some contribution from asymmetric stretching vibration of non-bonded PO_2 group of Q^2 tetrahedral site, $\nu_{as}(PO_2)$ [198,200]. This band shifts to lower wavenumbers due to depolymerization of the phosphate network resulting in increase of P=O bond length because of decrease in the average degree of π-bonding [197,200]. Thus, in the case of pure vitreous P_2O_5 glass the ν_s(P=O) band was visible as an intense feature near 1390 cm^{-1} [197].

Addition of alkali cations in our studied glasses results in downshift of this band by more than 80 cm^{-1} (Figure 10). The broad and asymmetric band near 692−696 cm^{-1} visible in the spectra of samples G1−G5 is related with symmetric stretching vibration of P−O−P network, ν_s(POP) [197]. The shoulder at higher frequency side belongs to asymmetric stretching motion of the same group, ν_{as}(POP) [197]. Peak position of in-chain ν_s(POP) mode is not very sensitive to the composition of the samples (Figure 10).

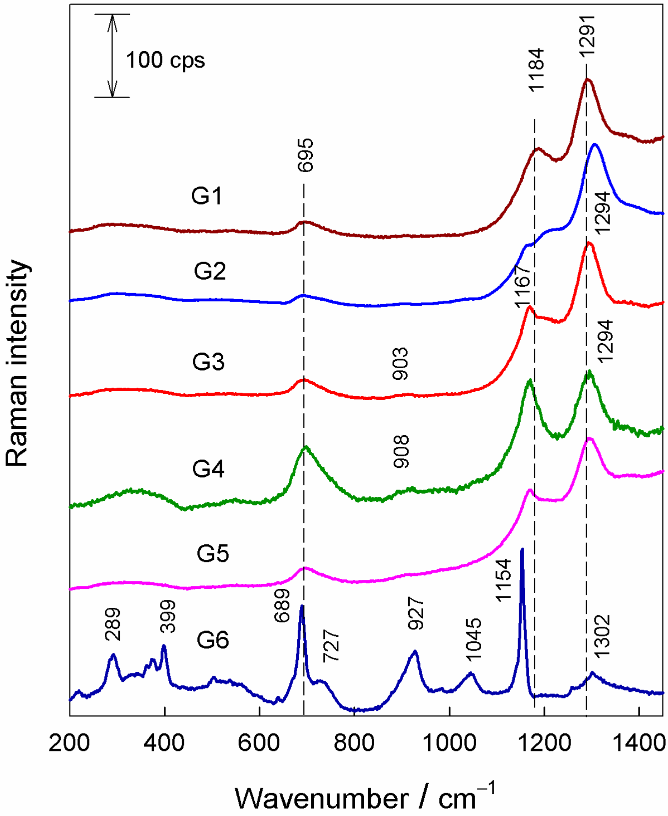

Figure 10. Composition dependent Raman spectra of phosphate glasses without Eu (samples G1−G6). The excitation wavelength is 785 nm (3 mW).

The highly structure-sensitive band is associated with symmetric stretching vibration of non-bridged oxygen PO_2 groups in Q^2 tetrahedron site, $\nu_s(PO_2)$ [197]. The position of this mode is cation-dependent; downshifts in frequency with decreasing electronegativity of the cation [197,201]. Two types of $\nu_s(PO_2)$ modes were distinguished in this work; higher frequency bands in strained tetrahedral structure (1180−1219 cm^{-1}) and lower frequency modes for unstrained Q^2 tetrahedral structure (1154−1171 cm^{-1}) [197,202]. Assignments of vibrational bands based on the previous extensive studies [197–210] as well as Raman peak positions of considered samples are displayed in the Table 4. Composition-induced changes in parameters of stretching vibrational bands of phosphate group are more clearly visible in Figure 11. Raman spectra reveal strained Q^2 structure for samples G1, G2, and G3 with corresponding peak position of $\nu_s(PO_2)$ bands at 1184, 1207, and 1219 cm^{-1}, respectively. Samples G2−G5 show unstrained $\nu_s(PO_2)$ band near 1160−1170 cm^{-1} (Table 4). Thus, samples G2 and G3 exhibit both strained and unstrained Q^2 tetrahedral structures, while only unstrained structure was detected for samples G4 and G5. Analysis of $\nu_s(P{=}O)$ band reveals that the sample G2 contains terminal phosphate group in Q^3 tetrahedral site with the shortest P=O bond length because the highest observed corresponding stretching frequency (1305 cm^{-1}) (Table 4).

Table 4. Peak positions (cm^{-1}) of Raman bands in spectra of different composition phosphate glasses.

Vibrational mode	Phosphate glass sample					
	G1	G2	G3	G4	G5	G6
$\nu_s(P{=}O)$ of terminal Q^3 tetrahedron; $\nu_{as}(PO_2)$ of non-bridging oxygen atoms of Q^2 tetrahedron.	1291 vs (1300 vs)	1305 vs (1290 vs)	1294 vs (1294 vs)	1294 vs (1295 s)	1294 vs (1294 vs)	1302 w (1302 vs)
$\nu_s(PO_2)$ strained, non-bridging oxygens atoms of Q^2 tetrahedron	1184 vs (1217 w)	1207 w (1180 vs)	1219 w	–	–	–
$\nu_s(PO_2)$ non-bridging oxygens of Q^2 tetrahedron	– (1163) vs	1160 w	1167 m (1166 m)	1166 vs (1171 vs)	1170 m (1169 m)	1154 vs, 1139 vw (1156 vs, 1140 s)
$\nu_{as}(POP)$; $\nu_s(PO_4^{3-})$ non-bridging oxygen atoms of Q^0 tetrahedron	–	–	903 w (905 w)	908 w	899 vw (901 vw)	927 s (926 m, 903 w)
$\nu_s(POP)$	695 m (691 m)	692 m (699 m)	693 m (694 m)	697 m (700 m)	696 m (697 m)	689 s (688 m)

Assignments based on references: [2–4,8–14,211–213]; Abbreviations: vs, very strong; s, strong; m, middle; w, weak; vw, very weak; ν_s, symmetric stretching; ν_{as}, asymmetric stretching.

Raman spectrum of sample G6 (Figure 10) exhibits several narrow bands located at 1154, 689, and 399 cm^{-1}; no intense and broad feature near 1290 cm^{-1} associated with ν_s(P=O) mode is visible. Instead, very low intensity several peaks are seen at 1260 and 1302 cm^{-1}. These bands most likely are associated with asymmetric stretching vibration of non-bonded PO_2 groups. Thus, characteristic Q^3 tetrahedral site is absent for this sample. The low intensity band near 1045 cm^{-1} is associated with symmetric stretching vibration of non-bonded PO_3 group [203] and reflects presence of Q^1 tetrahedral site for this sample. Presence of small amount of non-bonded phosphate groups in Q^0 tetrahedral sites is apparent from the visible band of symmetric stretching vibration $\nu_s(PO_4^{3-})$ near 927 cm^{-1} (Figure 10) [203–205,210]. Alternatively, this band might be related with asymmetric stretching vibration of P−O−P network [203,209]. The phosphate Raman bands of sample G6 are considerably narrowed comparing with other samples (Figure 10). Thus, the full width at half maximum (FWHM) value of $\nu_s(PO_2)$ band of sample G4 at 1166 cm^{-1} was found to be 58.8 cm^{-1}. In the case of sample G6 (Figure 10), the FWHM value for band at 1154 cm^{-1} decreases to 10.6 cm^{-1} indicating formation of crystalline phase containing pyrophosphate anions [198,209].

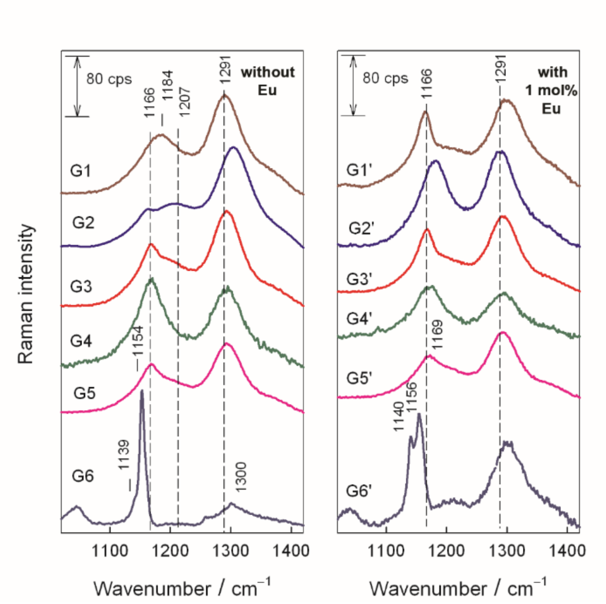

Figure 11. Composition dependent Raman spectra of phosphate glasses without Eu (samples G1−G6) and with Eu (samples G1′−G6′) in phosphate group stretching vibrations spectral region. Spectra are background corrected by using polynomial function. The excitation wavelength is 785 nm (3 mW).

2.4.3. Effect of Europium Ions (1 mol – %) on Raman Spectra of Phosphate Glasses

Introduction of europium into the phosphate glasses of different composition results in observable perturbations of the Raman spectra, which are compared in Figure 11. The Raman spectra of phosphate glasses containing europium in the wide frequency region (200−1450 cm^{-1}) are displayed in Appendix 1 (Supporting Information). In the case of sample G1´, two Eu-induced perturbations are clearly visible. Firstly, the prominent ν_s(P=O) band shifts to higher wavenumbers by 9 cm^{-1} indicating that average degree of bond order increases due to increase in π-bond localization on the Q^3 tetrahedral site.[197] Secondly, the $\nu_s(PO_2)$ band downshifts by 21 cm^{-1} and width of the mode considerable narrows (FWHM decreases from 85.0 to 43.5 cm^{-1}) (Figure 11 and Table 4). The reduction in frequency indicates changes in interaction of non-bonded PO_2 groups with the cations in the presence of europium ions. This result in more homogeneous structure of Q^2 tetrahedral sites (lower FWHM). The increase in ν_s(P=O) bond frequency was observed only for the sample G1´. No observable changes were found for samples G3´ and G4´. In contrast, sample G2´ shows opposite behavior; frequency of ν_s(P=O) band considerably decreases (15 cm^{-1}) indicating increase in π-bond delocalization, decrease in P=O bond order and increase in bond length. In addition, the intensity of strained $\nu_s(PO_2)$ mode at 1180 cm^{-1} considerably increases, suggesting development of more Q^2 tetrahedral structure sites in the presence of europium ions. In the case of sample G6´(Figure 11), introduction of europium ions results in considerable increase in intensity of prominent ν_s(P=O) band at 1302 cm^{-1} indicating development of more Q^3 tetrahedral sites. The presence of crystalline-structure phosphate sites is evident for this sample from the detected narrow bands at 1140 cm^{-1} (FWHM=12.4 cm^{-1}) and 1156 cm^{-1} (FWHM=16.1) associated with $\nu_s(PO_2)$ vibrational mode of non-bridging oxygen atoms in Q^2 tetrahedral sites.

2.4.4. Effect of Europium Emission on Glass Composition and Europium Content

One of the aims of this study is to develop new low temperature glass compositions acting as a host material for Eu^{3+} ions. Photoluminescence spectra excited under 393 nm light are consistent with other glass matrices doped with Eu^{3+} described in literature [214–217]. As can be seen in Figure 12 emission spectra of phosphate glasses consist of $^5D_0 \rightarrow {}^7F_J$ transition peaks: $^5D_0 \rightarrow {}^7F_0$, $^5D_0 \rightarrow {}^7F_1$, $^5D_0 \rightarrow {}^7F_2$, $^5D_0 \rightarrow {}^7F_3$ and $^5D_0 \rightarrow {}^7F_4$ transitions are located at

580 - 600 nm ,605 - 629 nm, 646 - 658 nm and 680 - 710 nm ranges, respectively. The magnetic dipole transition $^5D_0 \rightarrow {}^7F_1$ (maximum at 596 nm) is allowed by selection rules, in contrast to the electric dipole transition $^5D_0 \rightarrow {}^7F_2$ (maximum at 616 nm), whose strength increases with a reduction in the symmetry of the local environment of Eu^{3+}. Since europium exhibits similar behavior as in low symmetry crystals the center of a distorted cubic crystal field is occupied by Eu^{3+} ions and each of the vertices are occupied by oxygen, two of which usually form an edge belonging to the same tetrahedron of phosphate group. As previously discussed in the section 2.4.2 these tetrahedral sites can be connected to phosphate network through either one, two or three oxygen atoms or none at all. This directly reflects in europium ligand field where phosphate groups could experience inhomogeneous strains arising from how they are connected to the glass network, which in turn also reflects in variable ligand fields arising from differences in oxygen to europium bond lengths. Comparing the emission intensity of different glass compositions for $^5D_0 \rightarrow 7F_1$, $^5D_0 \rightarrow {}^7F_2$, $^5D_0 \rightarrow {}^7F_4$ transitions, while dopant concentration is kept constant (1% Eu), G1 resulted in emission intensity, more than two times that of the lowest intensity (G6) composition (Figure 12).

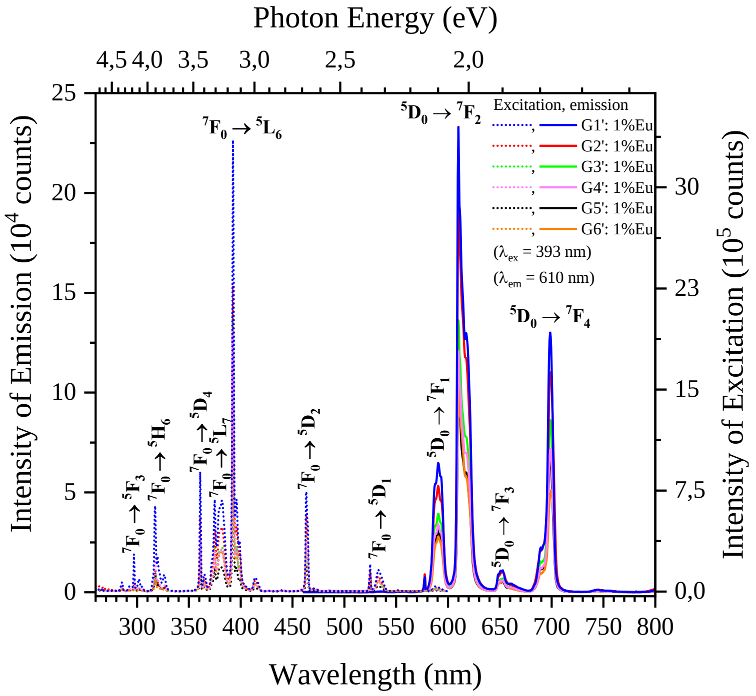

Figure 12. Emission and excitation intensity comparison between different glass compositions where dopant level remains constant.

Moreover, the influence of europium content on luminescence properties has been also investigated. For this purpose, separately 0.2%, 0.6% or 1% of Eu^{3+} (mol-%) were added to the precursor batch. As can be seen in Figure 13, the glass samples produced visual differences in color (changing from pink to orange).

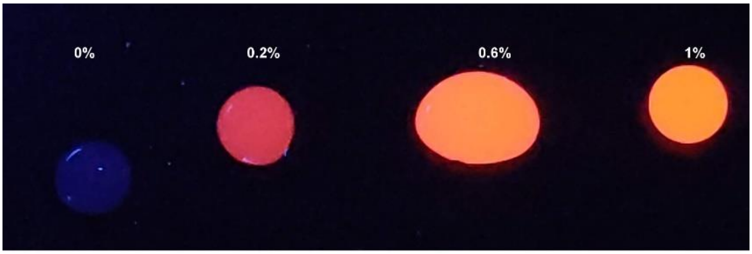

Figure 13**.** Optical image of G1 glass composition showing differences between different dopant levels (λ_{ex}= 395 nm).

Detailed luminescence results are given in Figure 14. As can be expected with increasing levels of Eu in glasses, emission intensity (λ_{ex} = 395 nm) also increases. As an example, the luminescence intensity at 610 nm, going from 0.2% to 0.6% and then to 1% of Eu, increases 2.0 and 2.8 times respectively for the G1 glass composition.

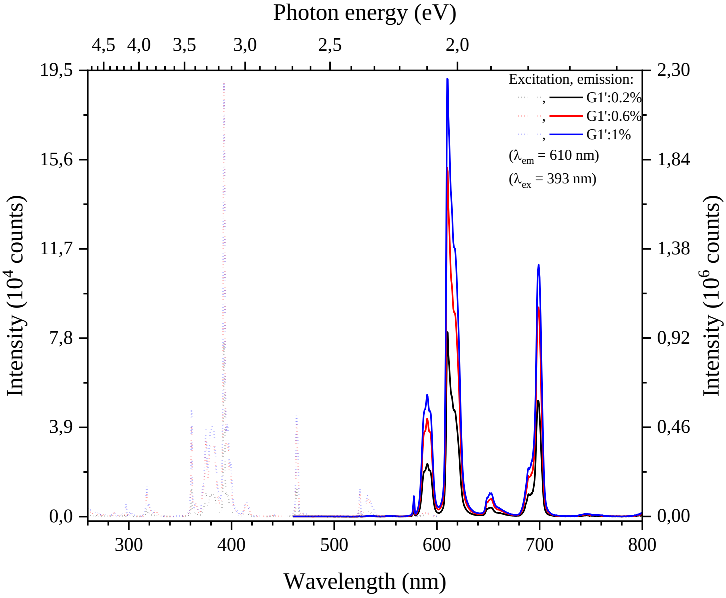

Figure 14**.** Photoluminescence emission and excitation spectra of G1 glass composition.

It was explained in other studies that europium emission ratio of $^5D_0 \rightarrow ^7F_2/^5D_0 \rightarrow ^7F_1$ in high symmetry environments is less than or equal to one, conversely the higher the ratio the lower symmetry sites is occupied by europium [218]. Variations in sample composition introduce differences in coordination number, ligand distances, and bond angles which also influence ligand field strength leading to differences in ion energy levels. Comparing relative intensities of $^5D_0 \rightarrow ^7F_2/^5D_0 \rightarrow ^7F_1$ in Table 5. All values fall within 3 – 4 indicating low symmetry of europium environment which is consistent with the values reported in literature [214,218].

Table 5. Relative intensities of $^5D_0 \rightarrow ^7F_2/^5D_0 \rightarrow ^7F_1$ emission lines.

Eu	Composition					
mol–%	G1’	G2’	G3’	G4’	G5’	G6’
0.2	3.60	3.51	3.41	3.48	3.33	3.87
0.6	3.58	3.56	3.44	3.52	3.39	3.93
1	3.60	3.59	3.46	3.54	3.33	3.79

For certain applications (e.g., as a lasing material, in lighting applications where specific color purity in needed, etc.) decreasing all other emission wavelengths except 610 nm can be beneficial [216,219]. Calculated integral intensity ratios in percent of $^5D_0 \rightarrow ^7F_2$ emission line (605 nm – 630 nm compared to emission intensity in the range of 520 nm – 750 nm are given in Table 6. Note that in all cases the ratio value is over 50% and varies only slightly indicating the transition $^5D_0 \rightarrow ^7F_2$ is dominant irrespective of the type of tetrahedral phosphate sites in glasses.

Table 6. Relative integral intensities of $^5D_0 \rightarrow ^7F_2$ emission line expressed in percent of total emission.

Eu	Composition					
mol–%	G1’	G2’	G3’	G4’	G5’	G6’
0.2	53.0	51.4	50.9	52.8	50.3	53.0
0.6	53.7	52.4	51.7	52.4	51.9	54.2
1	54.2	53.5	52.2	53.6	51.4	55.2

In addition, the analysis of morphology and homogeneity of elemental distribution on the surface of the samples demonstrated that investigated elements are dispersed throughout all of the surface of the glass sample homogenously. Note that the clearly visible grooves on the surface of the glass were induced by the sanding procedure. The result of SEM micrographs and EDX mapping for the selected elements are presented in Figure 15. Different shades of grey in the images of selected elements represent their relative amount on the surface of the glass.

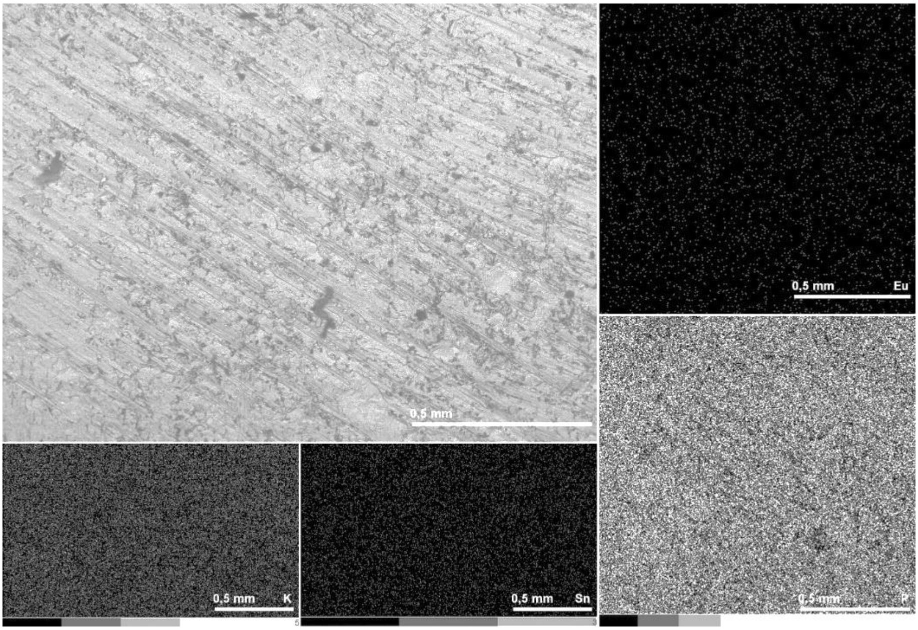

Figure 15**.** SEM micrograph and EDX mapping images for selected elements in G1: 1% Eu glass composition.

2.4.5. Glass Containing Cerium Dopants

A group of different glass compositions containing yttrium aluminum garnet doped with cerium were synthesized. To have homogenously distributed all of the compositional compounds within a glass structure the precursors must be melted at high temperature, which poses a risk and an inevitability of dissolution of garnet structure. Since the part of dopant within the glass composition is or must be negligible in order to have a transparent or at least transparent enough final composition not to completely disperse/reabsorb incident and also emitted light. These two proposed points make it necessary to perform synthesis at the lowest temperature possible, however there still remains another obstacle to overcome which is the inevitable dissolution of ambient gasses (also including moisture) in the precursor melt, thus completely oxidizing Ce(III) to Ce(IV) in the final stages. Since the ancient times some forms of reducing agents (possibly completely unknowingly) were used in the synthesis of red, dichroic, photochromic or avanturescent glass.

For this purpose, a reducing agent is needed to prevent cerium from oxidizing. It is known that i.e., metallic iron powder, copper(I) oxide, some chromium salts can act as reductants in glass melt, however, when incorporated into the glass structure, they have coloring properties. In this work tin(II) chloride was used to provide an easily distributable solid salt in the final precursor mixture (Table 2). From the XRD data presented (Figure 16) only the sample containing the largest molar fractions of SnO shows one (as in sample C4) or a few diffraction peaks (as in sample C1), which imply that it can be attributed to tin pyrophosphate (SnP_2O_7, PDF: 00-029-1352), same phenomena seen in glasses doped with europium.

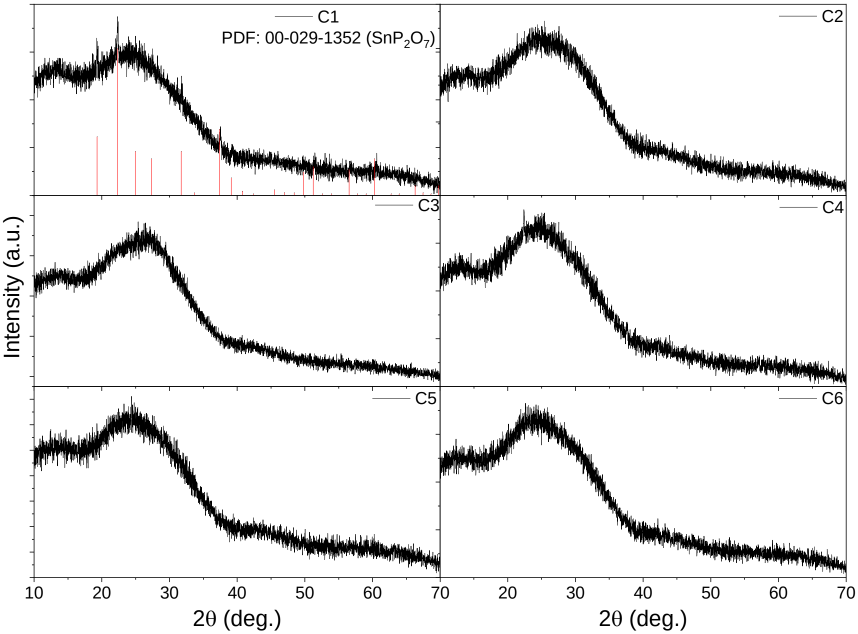

Figure 16. Powder X-ray diffraction patterns of different glasses doped with YAG:Ce^{3+}.

As can be seen (Figure 17) from the photoluminescence excitation and emission spectra without the reducing reagent, cerium easily oxidizes to its +4 state leaving majority of its emission intensity in the ultra-violet region. Some sharper lines in the emission spectra of C2 and C5 samples around 620 nm and around 700 nm show that at elevated temperatures (at the synthesis temperature) phosphate glasses tend to vaporize and deposit in the reaction chamber, since these exact compositions were synthesized after the Eu^{3+} doped ones.

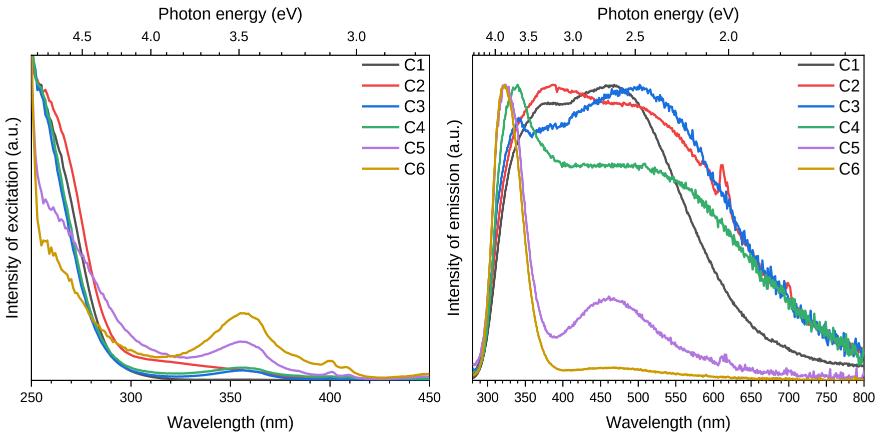

Figure 17. Normalized photoluminescence excitation (λ_{em} = 470 nm) and emission (λ_{ex} = 470 nm) spectra of different glass compositions doped with YAG:Ce^{3+}.

The addition of tin(II) salts prevent oxidation of Ce^{3+} up to a certain degree. There is a downside to this type of reducing environment however, tin(II) as it oxidizes to tin(IV) tends to distribute inhomogenously throughout the volume of the glass clearly seen in optical images of finished glass samples (Figure 18), tends to start to crystallize as was seen in XRD data and makes the resultant glass less transparent, sometimes causing an opalescent surface of the samples.

Figure 18. Examples of as synthesized glasses showing inhomogeneous distribution of glass components within finished samples.

2.5. Synthesis and Characterization Yttrium Iron Garnet Doped with Lanthanum, Cerium, Praseodymium and Neodymium Ions

2.5.1. X-Ray Characterization

Looking at the $Y_{3-x}La_xFe_5O_{12}$ garnet, different solubility limits are reported in literature such as x = 0.45 [220], x = 0.75 [45] or even x = 0.8 [221] which is consistent with the results demonstrated in this work. X-ray diffraction (XRD) patterns of lanthanum substituted yttrium iron garnets $Y_{3-x}La_xFe_5O_{12}$ are shown in Figure 19. As seen, when the molar substitution of yttrium by lanthanum is 25% only low intensity diffraction peak attributable to perovskite $LaFeO_3$ could be identified. With increasing substitutional level of La the amount of perovskite phase also increases, thus decreasing the relative part of garnet phase. Evidently, no garnet phase can be detected in the XRD pattern when reaching complete nominal substitution of yttrium. In this case, only $LaFeO_3$ and Fe_2O_3 have formed during sol-gel synthesis.

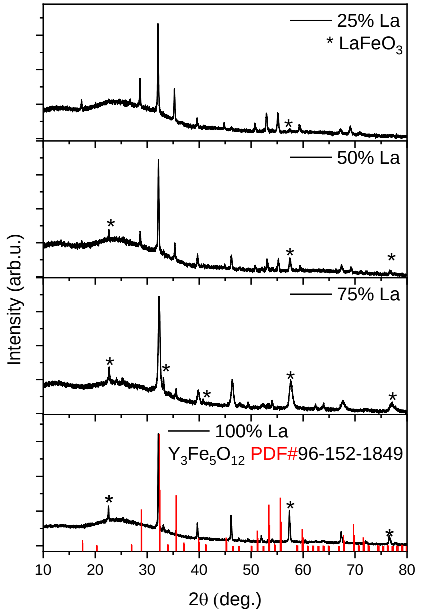

Figure 19. Powder X-Ray diffraction patterns of $Y_{3-x}La_xFe_5O_{12}$ samples with different lanthanum substitutional level. Vertical lines represent standard XRD pattern of YIG.

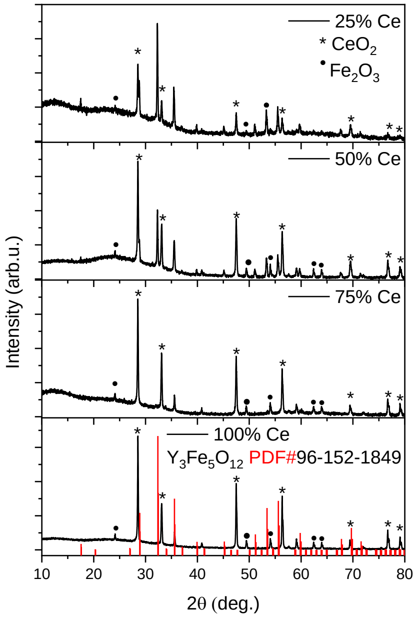

Figure 20. Powder X-Ray diffraction patterns of $Y_{3-x}Ce_xFe_5O_{12}$ samples with different cerium substitutional level. Vertical lines represent standard XRD pattern of YIG.

In the case of $Y_{3-x}Ce_xFe_5O_{12}$ system (see Figure 20), the formation of monophasic garnet does not proceed in whole substitutional range. Only minor amount of garnet phase could be identified in the samples with x = 0.25. The oxides such as CeO_2 and Fe_2O_3 are the main crystalline phases determined in all synthesized samples.

The XRD patterns of Pr and Nd substituted garnets ($Y_{3-x}Pr_xFe_5O_{12}$ and $Y_{3-x}Nd_xFe_5O_{12}$) are presented in Figure 21 and Figure 22, respectively. The results obtained in these cases are very similar. As seen, even the mixed-metal garnets $Y_{1.5}Pr_{1.5}Fe_5O_{12}$ and $Y_{1.5}Nd_{1.5}Fe_5O_{12}$ are monophasic compounds. However, the negligible amount of perovskite phase is formed in the case when 75% of yttrium is replaced by praseodymium. On the other hand, in the case of neodymium the synthesis product with such substitutional level still is monophasic garnet compound.

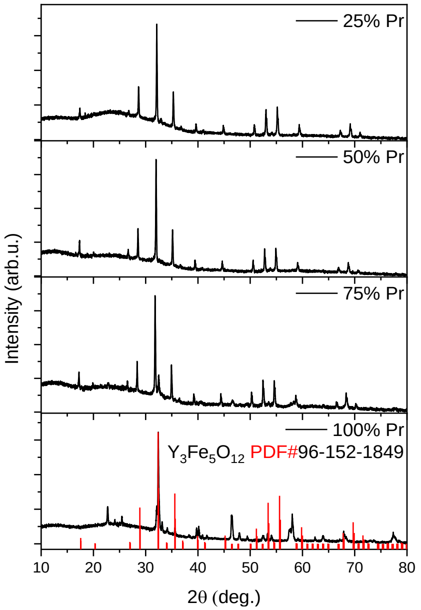

Figure 21. Powder X-Ray diffraction patterns of $Y_{3-x}Pr_xFe_5O_{12}$ samples with different praseodymium substitutional level. Vertical lines represent standard XRD pattern of YIG.

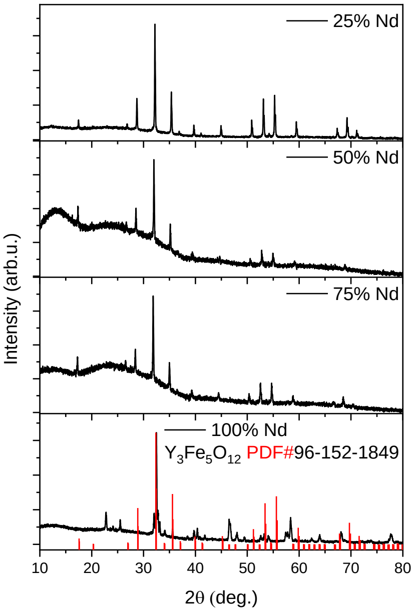

Figure 22. Powder X-ray diffraction patterns of $Y_{3-x}Nd_xFe_5O_{12}$ samples with different neodymium substitutional level. Vertical lines represent standard XRD pattern of YIG.

2.5.2. FTIR Spectroscopy

It is well known, that definite substances can be identified by their IR spectra, interpreted like fingerprints [222]. The FTIR spectra of sol-gel derived $Y_{3-x}Ln_xFe_5O_{12}$ specimens in the region of 850-400 cm^{-1} are depicted in Figure 23, Figure 24, Figure 25, and Figure 26. It is interesting to note, that FTIR spectroscopy results are in a good agreement with ones obtained using XRD measurements. For example, the FTIR spectra of $Y_{3-x}La_xFe_5O_{12}$ samples with lower substitutional level of La (25% and 50%) (Figure 23) contain absorption bands attributable to the M–O stretching frequencies at 645-644 cm^{-1}, 580-579 cm^{-1} and 549-548 cm^{-1}.

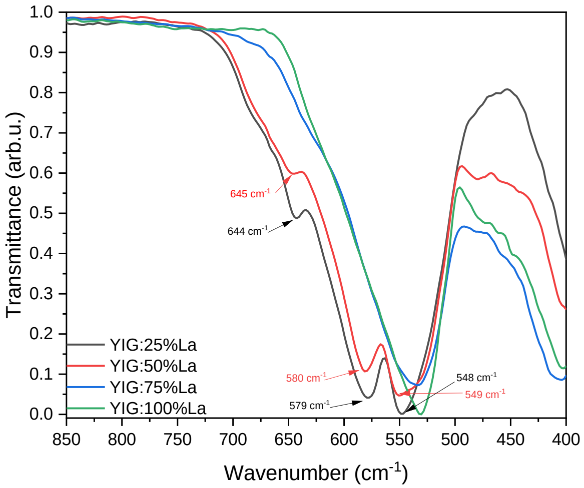

Figure 23. FTIR spectra of $Y_{3-x}La_xFe_5O_{12}$ samples with different lanthanum substitutional level.

Thus, it is already well known that the FTIR spectra of the garnets usually contain several intense peaks in the range of 1000–400 cm^{-1}. These bands are characteristic for garnet structures compounds and are attributable to the stretching mode of the tetrahedral units present in the garnet structure.

However, with increasing amount of lanthanum the broad absorption band in this region is not split anymore to several narrow ones. Such stretching frequencies are characteristic of perovskite orthorhombic and cubic stretching modes. So, these FTIR spectroscopy results clearly confirm formation of perovskite crystalline phase instead of garnet at higher substitutional level of La.

Very similar FTIR spectrum in the region of 850–500 cm^{-1} was obtained for $Y_{3-x}Ce_xFe_5O_{12}$ sample when 25% of yttrium was replaced by cerium (Figure 24). However, an additional band is observed as broad band at 471 cm^{-1} which could be attributed to M-O vibrations in the single oxides such like CeO_2 or Fe_2O_3. The origin of FTIR spectra of $Y_{3-x}Ce_xFe_5O_{12}$ samples gradually changes with increasing amount of Ce in the sample. Again, the broad absorption band in the region of 645-548 cm^{-1} is not split. Besides the maximum of this absorption band is shifted to the lower region of wavenumbers in comparison with FTIR spectra of $Y_{3-x}La_xFe_5O_{12}$ samples with higher substitutional level of La (75% and 100%). Besides, additional absorption bands detectable at around 430 cm^{-1} confirm the XRD results concerning the formation of single oxides CeO_2 or Fe_2O_3 during synthesis of these specimens.

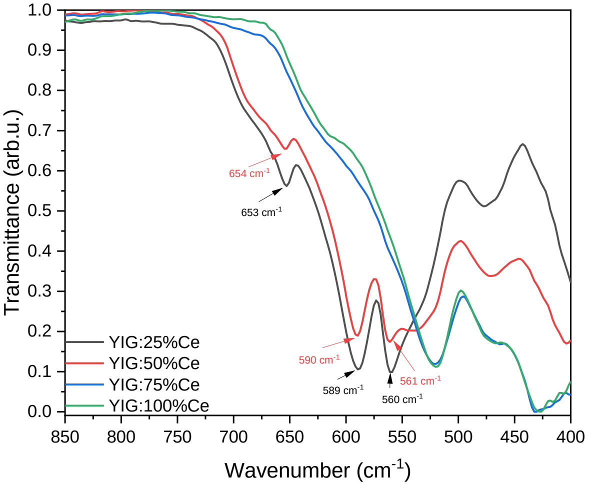

Figure 24. FTIR spectra of $Y_{3-x}Ce_xFe_5O_{12}$ samples with different cerium substitutional level.

The FTIR spectra of $Y_{3-x}Pr_xFe_5O_{12}$ and $Y_{3-x}Nd_xFe_5O_{12}$ garnets are presented in Figure 25 and Figure 26, respectively. Evidently, FTIR results show similar correlation with the results obtained using XRD analysis. The formation of garnet phases as the main crystalline phase could be clearly confirmed at 0-75% substitutional levels of Pr and Nd.

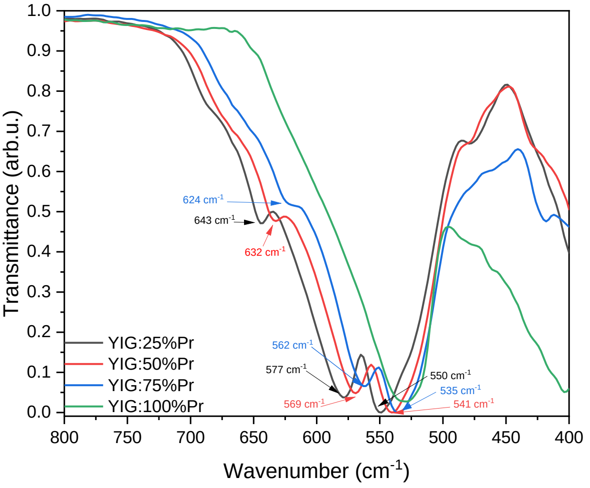

Figure 25. FTIR spectra of $Y_{3-x}Pr_xFe_5O_{12}$ samples with different praseodymium substitutional level.

The perovskite phases prevail when yttrium is completely replaced by praseodymium or neodymium. Once again, summarizing we can conclude that FTIR spectroscopy is an indispensable tool for the characterization of reaction products during the synthesis of garnet crystal structure compounds.

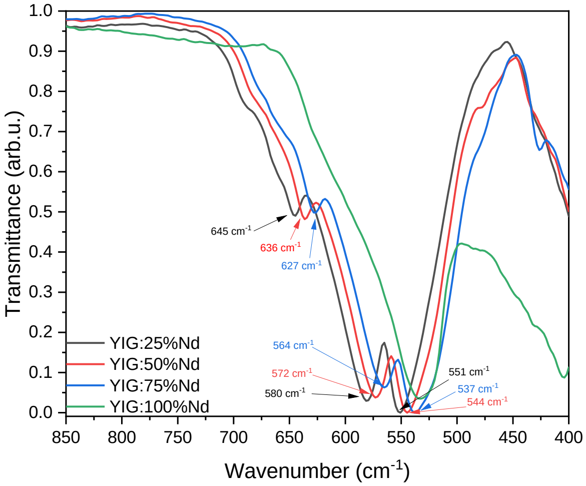

Figure 26. FTIR spectra of $Y_{3-x}Nd_xFe_5O_{12}$ samples with different neodymium substitutional level.

2.5.3. Magnetic Measurements

Magnetization hysteresis shown in Figure 27 has very different magnitudes of magnetization depending on composition of $Y_{3-x}M_xFe_5O_{12}$ samples.

Slightly smaller saturation magnetization of samples (Table 7) comparing with that of yttrium garnet $Y_3Fe_5O_{12}$ was obtained at the large (90-100%) content of ferrimagnetic garnet. It is noteworthy that some part of magnetic moments of rare earth ions Ce^{3+}, Pr^{3+} and Nd^{3+} which are antiferromagnetically coupled to resultant ferrimagnetic moment of iron ions may cause decrease in magnetization [223].

The other phases which may be found in the samples – rare earth perovskites $MFeO_3$ and hematite α-Fe_2O_3 have magnetic moments of iron atoms aligned antiferromagnetically resulting to magnetization of much smaller magnitude (Figure 27 d). Observed variation of coercivity may be related to changes in composition and structure of samples.

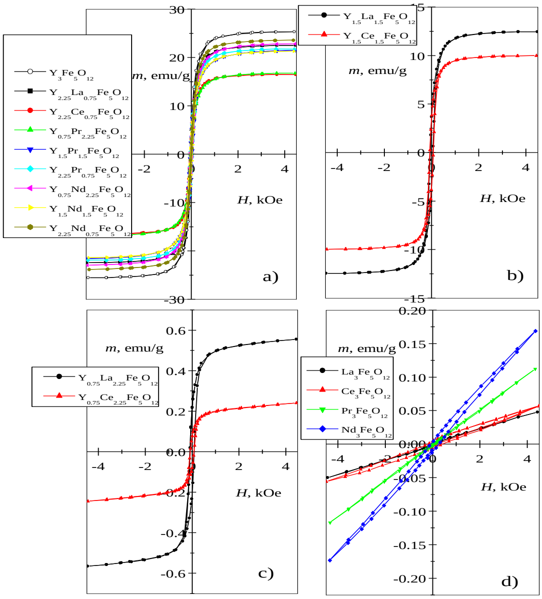

Figure 27. Magnetization hysteresis of $Y_{3-x}M_xFe_5O_{12}$ samples (M = La, Ce, Pr, Nd; x = 0.75, 1.5, 2.25, 3) having large (a), small amount (b, c) and without (d) garnet phase.

Table 7. Magnetization hysteresis parameters: saturation magnetization M_s (at H=4.4 kOe), coercive field H_c and percentage of garnet phase S_{gar} according to the area of Mössbauer spectra.

Sample	M_s (H=4.4 kOe), emu/g	H_c, Oe	S_{gar}, %
$Y_3Fe_5O_{12}$	25.3	19	100
$Y_{2.25}La_{0.75}Fe_5O_{12}$	22.5	31	93
$Y_{1.5}La_{1.5}Fe_5O_{12}$	12.4	60	57
$Y_{0.75}La_{2.25}Fe_5O_{12}$	0.55	88	0
$La_3Fe_5O_{12}$	0.048	35*	0
$Y_{2.25}Ce_{0.75}Fe_5O_{12}$	16.5	36	75
$Y_{1.5}Ce_{1.5}Fe_5O_{12}$	9.97	73	48
$Y_{0.75}Ce_{2.25}Fe_5O_{12}$	0.24	83	0
$Ce_3Fe_5O_{12}$	0.057	200*	0

Sample	M_s (H=4.4 kOe), emu/g	H_c, Oe	S_{gar}, %
$Y_{2.25}Pr_{0.75}Fe_5O_{12}$	21.7	38	96
$Y_{1.5}Pr_{1.5}Fe_5O_{12}$	21.4	59	95
$Y_{0.75}Pr_{2.25}Fe_5O_{12}$	16.8	31	74
$Pr_3Fe_5O_{12}$	0.11	45*	0
$Y_{2.25}Nd_{0.75}Fe_5O_{12}$	23.6	19	100
$Y_{1.5}Nd_{1.5}Fe_5O_{12}$	21.3	47	96
$Y_{0.75}Nd_{2.25}Fe_5O_{12}$	22.8	38	92
$Nd_3Fe_5O_{12}$	0.17	150*	0

* half of hysteresis loop at M=0

Mössbauer spectra of $Y_{3-x}M_xFe_5O_{12}$ samples (Figure 28 and Figure 29) show the phase contributions of the garnet, rare earth perovskites $MFeO_3$ and hematite α-Fe_2O_3. The sample $Y_3Fe_5O_{12}$ is completely garnet phase. The octahedral *a* and tetrahedral *d* positions of the iron in garnet result to sextets in the Mössbauer spectra which have different isomer shifts, 0.38±0.01 and 0.16±0.01 mm/s relatively to α-Fe, and hyperfine field, ≈49 and ≈40 T, respectively (Table 8).

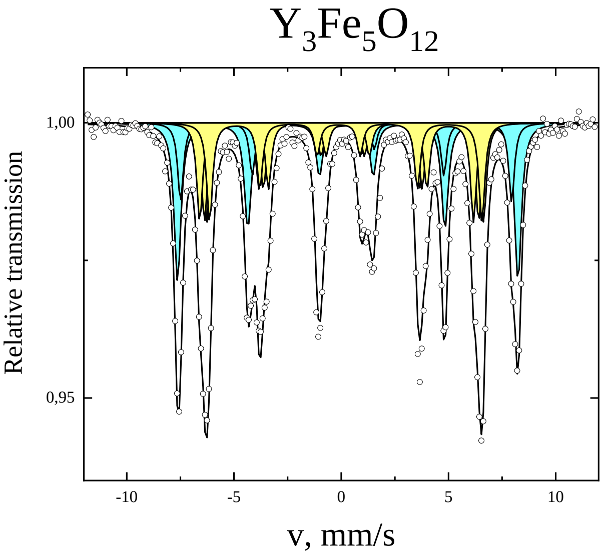

Figure 28. Mössbauer spectra of $Y_3Fe_5O_{12}$.

Six sextets according to the model presented in [224] were used to fit to Mössbauer spectra to obtain sufficient fitting quality of garnet contribution. Two sextets (with 1:3 area ratio) and four sextets (1:1:1:1 area ratio) for *a* and *d* iron sites, respectively, were applied. In each group the sextets had the same isomer shifts but differed by hyperfine field and quadrupole shifts (Table 8).

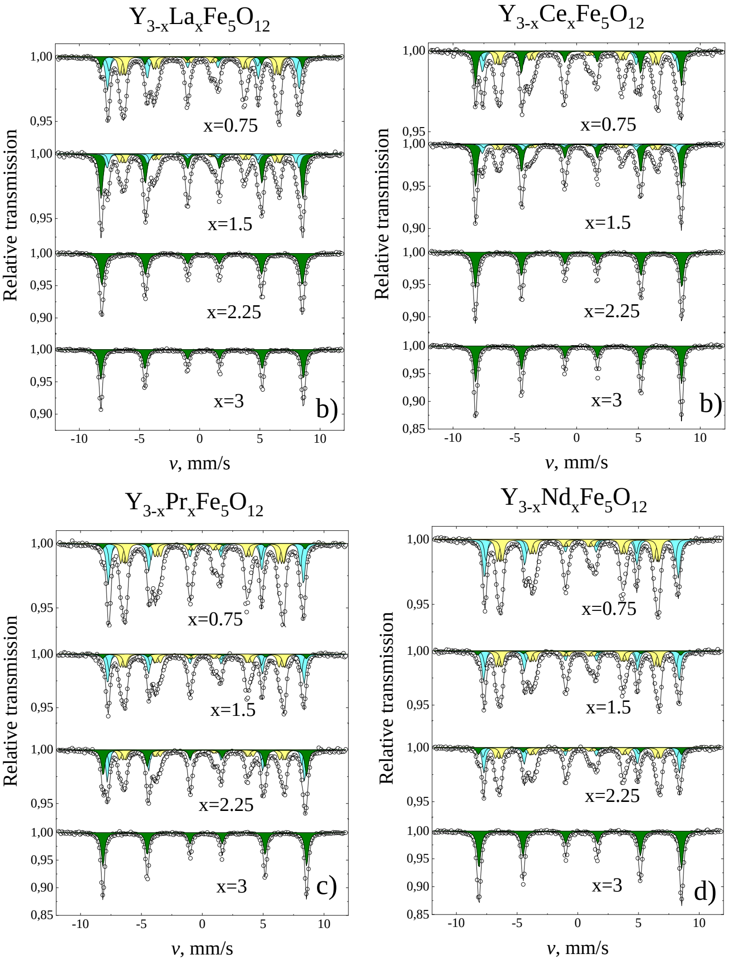

Figure 29. Mössbauer spectra $Y_{3-x}M_xFe_5O_{12}$ samples: M=La (a), Ce (b), Pr (c), Nd (d); x = 0,0.75,1.5,2.25,3, measured at room temperature. Subspectra colour: cyan – garnet a-sites, yellow – garnet d-sites, olive – rare earth orthoferrite + iron oxide.

The contribution of rare earth perovskite $MFeO_3$ and hematite α-Fe_2O_3 was fitted using additional sextet. The contributions of perovskite and hematite in samples can be easily distinguished only at higher than room temperature in Mössbauer measurements [225] taking advantage of their different Neel temperatures (Figure 30). In $M_3Fe_5O_{12}$ samples the ratio of areas of perovskite and hematite contributions corresponds well that obtained according to $M_3Fe_5O_{12}=3MFeO_3+\alpha\text{-}Fe_2O_3$ except Ce containing samples where perovskite $CeFeO_3$ apparently does not form (Table 8 and Table 9).

Table 8. Parameters of Mössbauer spectra at room temperature of $Y_{3-x}M_xFe_5O_{12}$ samples: *S* is the area attributable to garnet *a* and *d* sites or other phases, Γ is line width, δ is the isomer shift, 2ε–quadrupole shift, and *B* – hyperfine field.

Sample $Y_{3-x}M_xFe_5O_{12}$	Subsp.	*S*, %	Γ, mm/s ±0.01	δ, mm/s ±0.01	2ε, mm/s ±0.01	*B*, T ±0.04-0.1
x=0	*a*-sites	43	0.39; 0.32	0.38	0.07; -0.09	49.22;47.85
	d-sites	57	0.33	0.15	0.28;-0.05;-0.52;0.33	40.01;39.63; 39.57;39.36
M=La,	*a*-sites	39	0.36; 0.31	0.38	0.04; -0.08	49.37;48.16
x=0.75	*d*-sites	54	0.32	0.16	0.30;-0.04;-0.50;0.35	40.28;39.99; 39.87;39.55
	other	7	0.29	0.35	-0.12	51.88
x=1.5	*a*-sites	21	0.36;0.25	0.38	0.02;-0.12	49.39;48.19
	d-sites	32	0.32	0.17	0.28;-0.05;-0.54;0.38	40.28;40.06; 39.99;39.63
	other	47	0.36	0.36	-0.14	51.94
x=2.25	other	100	0.43	0.37	-0.12	51.65
x=3	other	100	0.35	0.37	-0.12	52.17
M=Ce,	*a*-sites	31	0.37; 0.31	0.38	0.08; -0.13	49.15;47.97
x=0.75	*d*-sites	44	0.32	0.15	0.27;-0.04;-0.49;0.41	39.75; 39.70; 39.57;39.57
	other	25	0.30	0.36	-0.20	51.65
x=1.5	*a*-sites	19	0.36;0.33	0.38	0.05;-0.15	49.14;47.85
	d-sites	29	0.33	0.16	0.32;-0.09;-0.54;0.34	40.02;39.62; 39.49;39.36
	other	52	0.33	0.37	-0.22	51.63
x=2.25	other	100	0.37	0.37	-0.21	51.77
x=3	other	100	0.32	0.37	-0.21	52.65

Sample $Y_{3-x}M_xFe_5O_{12}$	Subsp.	*S*, %	*Γ*, mm/s ±0.01	*δ*, mm/s ±0.01	2*ε*, mm/s ±0.01	*B*, T ±0.04-0.1
M=Pr,	*a*-sites	39	0.35; 0.27	0.38	0.04; -0.08	49.71; 48.47
x=0.75	*d*-sites	57	0.38	0.15	0.32;-0.06;-0.54;0.38	40.49; 40.20;40.09; 39.95;
	other	4	0.35*	0.37	-0.28	51.57
x=1.5	*a*-sites	37	0.33; 0.24	0.39	0.03; -0.05	50.04; 48.98
	d-sites	58	0.35	0.17	0.43;-0.05;-0.54;0.29	40.37; 40.54;40.40; 40.54;
	other	5	0.35*	0.39	-0.19	51.87
x=2.25	*a*-sites	28	0.28; 0.23	0.39	0.02; -0.05	50.23; 48.92
	d-sites	46	0.36	0.17	0.45;-0.04;-0.57;0.27	40.66; 40.81;40.82; 40.72;
	other	26	0.34	0.37	-0.11	51.82
x=3	other	100	0.33	0.37	-0.11	51.87
M=Nd,	*a*-sites	39	0.36; 0.27	0.38	0.05; -0.09	49.52; 48.33
x=0.75	*d*-sites	61	0.34	0.15	0.20;-0.04; -0.47;0.43	40.09; 40.16;39.98; 40.04;
x=1.5	*a*-sites	38	0.33; 0.26	0.39	0.03; -0.09	49.94; 48.79
	d-sites	58	0.32	0.16	0.23;-0.07;-0.52;0.45	40.57; 40.52;40.39; 40.38;
	other	4	0.35*	0.35	-0.25	51.87
x=2.25	*a*-sites	36	0.33; 0.30	0.39	0.04; -0.09*	50.01; 49.10
	d-sites	56	0.34	0.17	0.21;-0.06;-0.54;0.43	40.88; 40.75;40.77; 40.68;
	other	8	0.35*	0.35	-0.18	51.91
x=3	other	100	0.35	0.37	-0.12	51.74

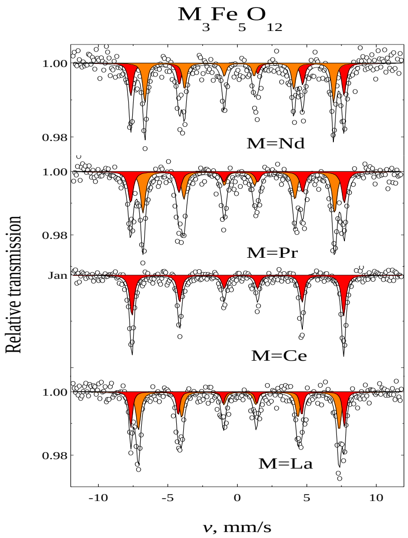

Figure 30. Mössbauer spectra of $M_3Fe_5O_{12}$ M=La, Ce, Pr, Nd measured at 200 °C temperature

Table 9. Parameters of Mössbauer spectra of $M_3Fe_5O_{12}$ (M=La, Ce, Pr, Nd) samples measured at 200 °C: S is the area of phases, Γ is the line width, δ-isomer shift, 2ε–quadrupole shift, and B – hyperfine field.

Sample	Subsp.	S, %	Γ, mm/s	δ, mm/s	2ε, mm/s	B, T
$La_3Fe_5O_{12}$	α-Fe_2O_3	34±3	0.30±0.03	0.21±0.01	-0.17±0.01	47.68±0.07
	$LaFeO_3$	66±3	0.40±0.03	0.25±0.01	-0.08±0.01	44.83±0.06
$Ce_3Fe_5O_{12}$	α-Fe_2O_3	100	0.38±0.01	0.25±0.01	-0.22±0.01	47.28±0.03
$Pr_3Fe_5O_{12}$	α-Fe_2O_3	45±2	0.44±0.03	0.24±0.01	-0.25±0.02	47.72±0.07
	$PrFeO_3$	55±2	0.42±0.02	0.24±0.01	-0.05±0.01	42.82±0.05
$Nd_3Fe_5O_{12}$	α-Fe_2O_3	49±2	0.38±0.03	0.24±0.02	-0.25±0.02	47.60±0.07
	$NdFeO_3$	51±2	0.35±0.03	0.24±0.01	-0.00±0.02	42.14±0.07

2.5.4. SEM Analysis

SEM micrographs of differently substituted yttrium iron garnets are depicted in Figure 31, Figure 32, Figure 33, Figure 34 for La, Ce, Pr and Nd respectively. All of the formed particles or particle agglomerates have irregular shape with size variance of few hundred micrometers of which the largest are comprised of an irregular array of porous structures. The surface morphology of these samples shows no real correlation between substitution level for the same substitutional ion or relationship between different lanthanide ions.

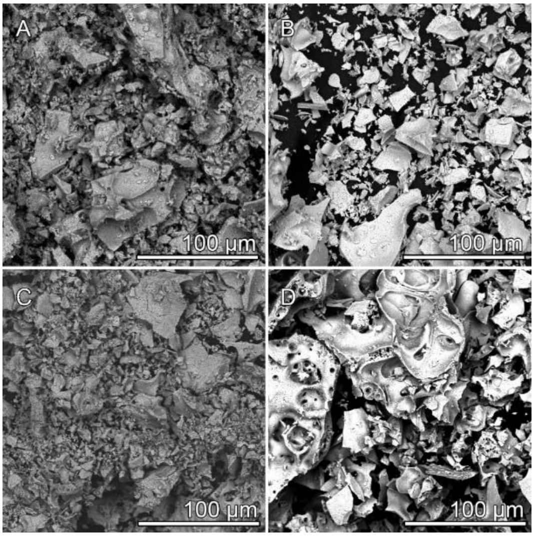

Figure 31. SEM micrographs of samples annealed at 1000 °C with theoretical compositions of $Y_{3-x}La_xFe_5O_{12}$ (A) x = 0.75, (B) x = 1.5, (C) x = 2.25, (D) x = 3.

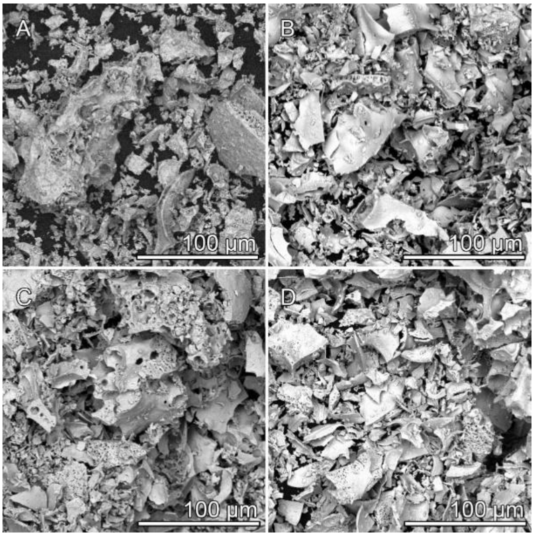

Figure 32. SEM micrographs of samples annealed at 1000 °C with theoretical compositions of $Y_{3-x}Ce_xFe_5O_{12}$ (A) x = 0.75, (B) x = 1.5, (C) x = 2.25, (D) x = 3.

As can be seen in Figure 35 from pure yttrium iron garnet micrograph, the same statements mentioned earlier hold true. It can be concluded that the proposed synthesis method does not permit control over the morphology at least to the extent when the annealing temperature is fixed.

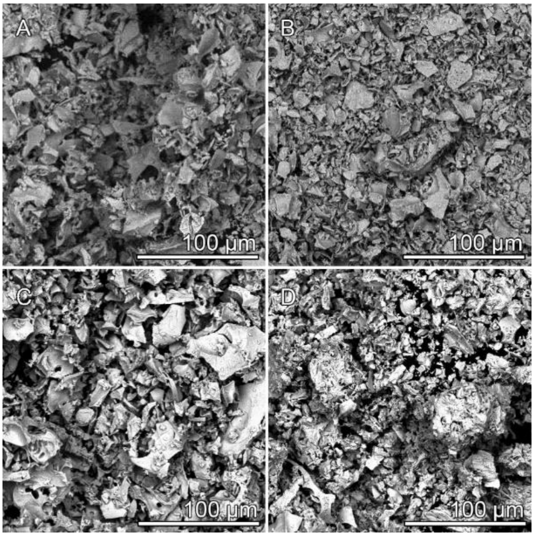

Figure 33. SEM micrographs of samples annealed at 1000 °C with theoretical compositions of $Y_{3-x}Pr_xFe_5O_{12}$ (A) x = 0.75, (B) x = 1.5, (C) x = 2.25, (D) x = 3.

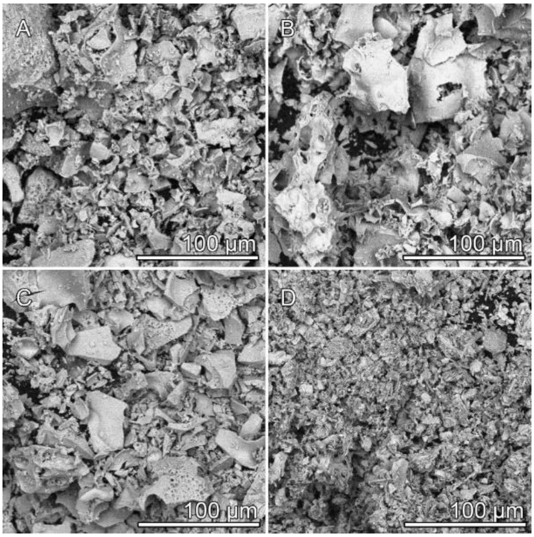

Figure 34. SEM micrographs of samples annealed at 1000 °C with theoretical compositions of $Y_{3-x}Nd_xFe_5O_{12}$ (A) x = 0.75, (B) x = 1.5, (C) x = 2.25, (D) x = 3.

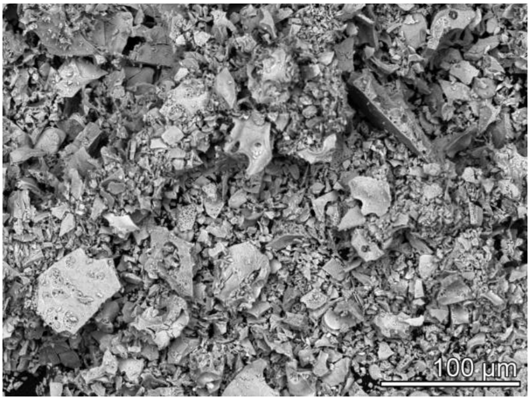

Figure 35. SEM micrograph of YIG sample annealed at 1000 °C.

2.6. Synthesis and Characterization Yttrium Aluminum Garnet Doped with Chromium Ions

2.6.1. Structural Analysis

The results of X-ray diffraction analysis are represented in Figure 36. It is evident that pure garnet structure compounds were obtained since every single peak might be attributed to the reference pattern of YAG (PDF#01-073-3185) having a space group I a -3 d of cubic crystal lattice. The garnet structure may be written in general terms as $A_3B_2C_3O_{12}$, where A has a coordination number of 8, B – 6, and C – 4. As it is known, the structure contains three types of coordination polyhedrons: dodecahedral, octahedral, and tetrahedral. Cr^{3+} ion radius is comparable to that of Al in a six-fold or octahedral coordination (0.535 angstroms for Al^{3+} and 0.615 angstroms for Cr^{3+}) from which can be implied that Cr^{3+} ions might replace Al^{3+} ions in the structure [226]. Note, that since only ppm amount of chromium has been inserted into the garnet structure there is no clear evidence of the peak shift. According to the Bragg's Law (27):

$$n\lambda = 2dsin\theta \tag{27}$$

and the Vegard's Law if smaller ions are replaced by larger ions the interplanar distance increases causing the peak shift to lower 2θ range. There are no extra peaks in the diffraction patterns even when the chromium molar part is the highest in the compound under our investigation conditions, therefore it is to be believed that chromium has been successfully introduced into the garnet matrix. Note that Rietveld refinement was also performed (see supplementary information, Appendix 4-10), however due to minute amounts of chromium a stricter approach using synchrotron radiation or even neutron diffraction might be deemed necessary to detect and explain structural effects and differences.

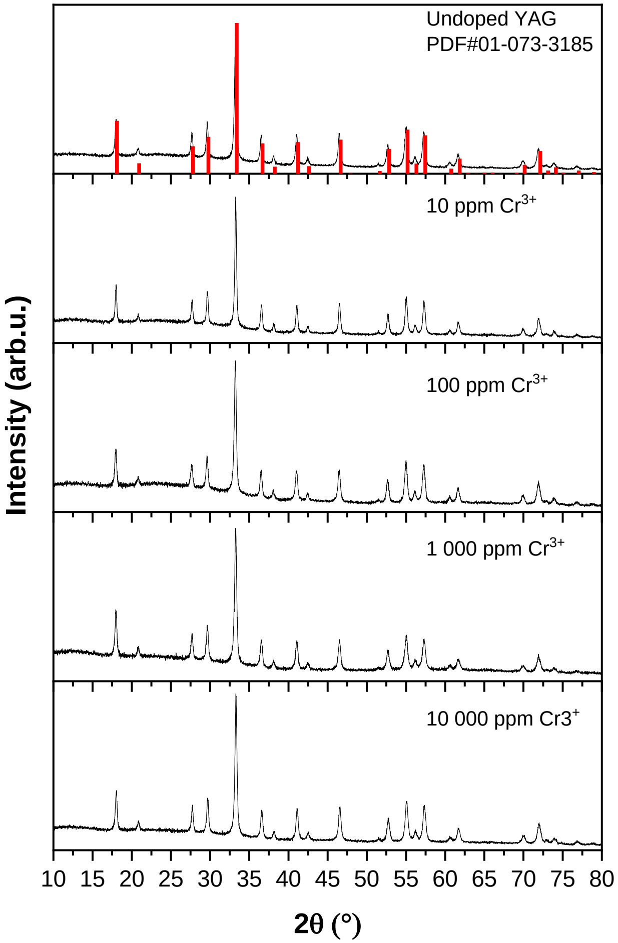

Figure 36. Powder X-ray diffraction patterns of undoped and doped samples.

2.6.2. FTIR Analysis

Additionally, all of the samples have been characterized by FTIR spectroscopy analysis. The FTIR spectrum of all doped and undoped samples shows prominent absorption peaks at 449, 508, 565 cm^{-1} (Figure 37) belonging to the bending motions of tetrahedral coordinated sites. Another set of vibrations at 685, 718, 785 cm^{-1} (Figure 37) are associated with the asymmetric stretching of AlO_4 tetrahedra which are typically only observed in garnet structure materials [227]. It should also be noted that no peaks that can be attributed to OH group vibrations might be seen in either of the samples which would quench the luminescence.

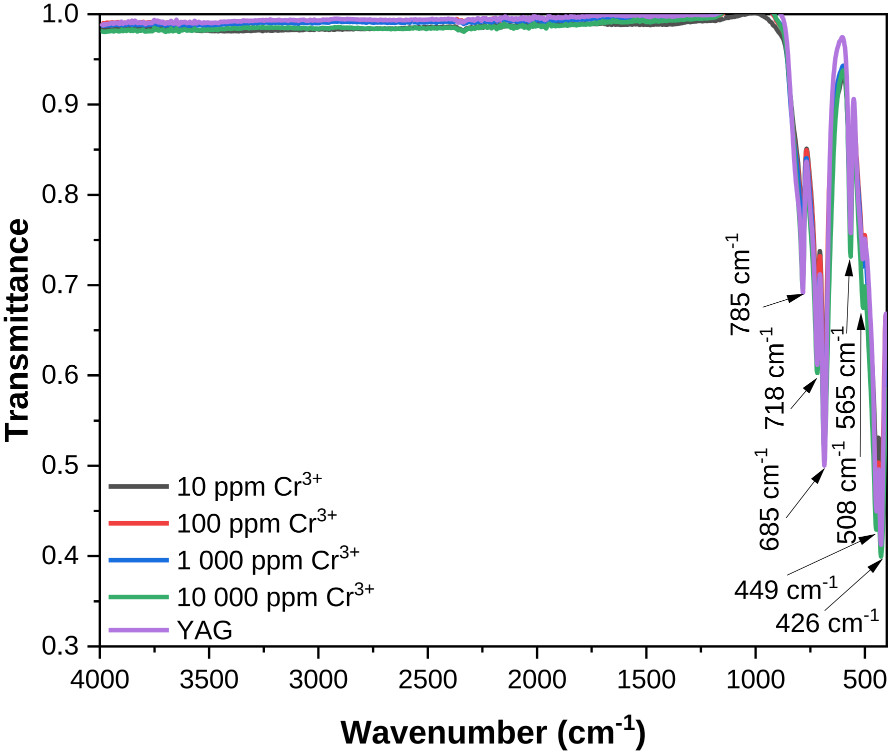

Figure 37. FTIR spectrum of undoped and doped garnet samples.

2.6.3. Photoluminescence

The optical properties of Cr^{3+} ions are directly dependent on the strength of the crystal field environment of the host lattice which is why in a weak crystal field Cr^{3+} shows a broadband emission line [228]. A broadband spin-allowed emission of $^4T_2 \rightarrow {}^4A_2$ transition arises in the range of 650 – 1600 nm whereas narrow emission lines around 700 nm are due to the spin forbidden $^2E \rightarrow {}^4A_2$ transition [229]. Generalizing, if Cr^{3+} ion is located at a strong crystal field the energy of ^2E level is lower than $^4T_2$ and sharp lines in the luminescence spectra can be seen, conversely, in a weaker crystal field ($^2E \rightarrow {}^4T_2$) only broad $^4T_2$ emission can be observed [229].

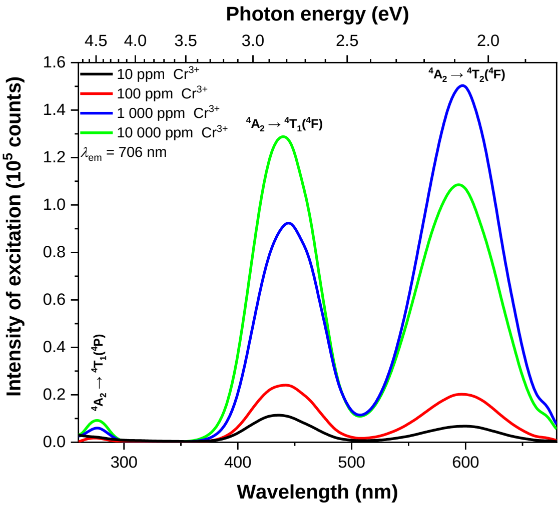

Figure 38. Photoluminescence excitation spectra of samples doped with Cr^{3+} under 706 nm emission.

The excitation spectra of doped samples (Figure 38) consist of three main peaks located at 275, 440, and 580 nm which are attributed to 3d intrashell transitions namely $^4A_2 \rightarrow {}^4T_1(^4P)$, $^4A_2 \rightarrow {}^4T_1(^4F)$, $^4A_2 \rightarrow {}^4T_2(^4F)$ respectively. It can be seen that the excitation absorbance increases with an increasing amount of dopant, however, the $^4A_2 \rightarrow {}^4T_2(^4F)$ peak intensity of 10 000 ppm sample is lower than the 1 000 ppm one suggesting that different samples have evidently different sites, the Cr^{3+} ions reside either in low-field sites or in high (or possibly - medium) field sites which is further reflected in the photoluminescence spectra shown in

Figure 39 and Figure 40.

Whether the samples are excited under 580 nm or 440 nm the narrow emission lines might be attributed to $^2E \rightarrow {}^4A_2$ spin forbidden transition.

As can be expected under 440 nm excitation the emission spectra show the typical trend of increasing luminescence intensity with a higher concentration of Cr^{3+} in the samples (Figure 41) meanwhile the sample containing 1000 ppm Cr^{3+} exhibit the most intensive emission under 580 nm excitation. The different splitting of energy levels of Cr^{3+} ions at octahedral position support an additional measurement of emission under 275 nm.

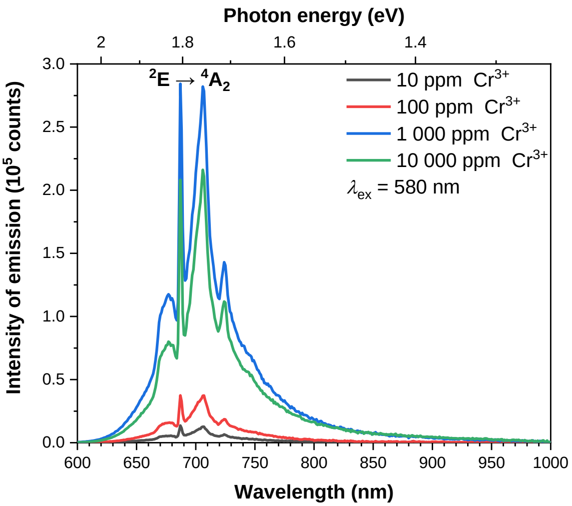

Figure 39. Photoluminescence emission spectra of samples doped with Cr^{3+} under 580 nm excitation.

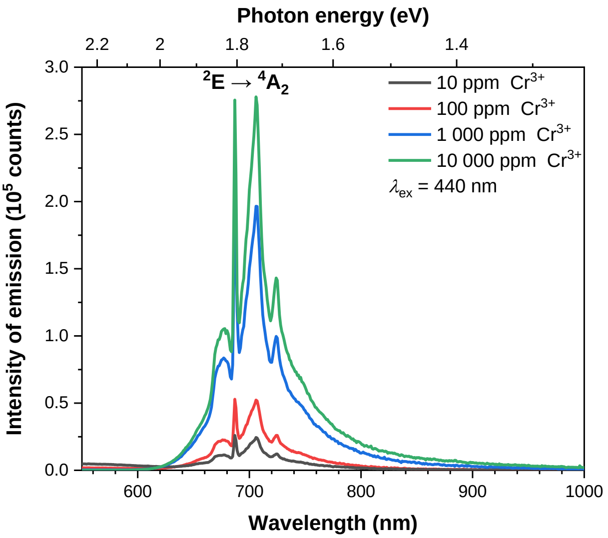

Figure 40. Photoluminescence emission spectra of samples doped with Cr^{3+} under 440 nm excitation.

If the samples are excited under 275 nm light, YAG:Cr emits a broad near-infrared band (Figure 41) with a peak position at about 800 nm (FWHM 100 nm) attributed to spin-allowed $^4T_2 \rightarrow {}^4A_2$ transition. As can be seen, the specific emission (inset of Figure 41) nearly exponentially decreases with increased dopant levels and almost vanishes when the content of chromium reaches 10 000 ppm. Moreover, if chromium concentration is 1 000 ppm or higher clear evidence of $^2E \rightarrow {}^4A_2$ is observed even under 275 nm excitation indicating the tiny change between ^2E and $^4T_2(^4F)$ energy levels of Cr^{3+} ions of different samples.

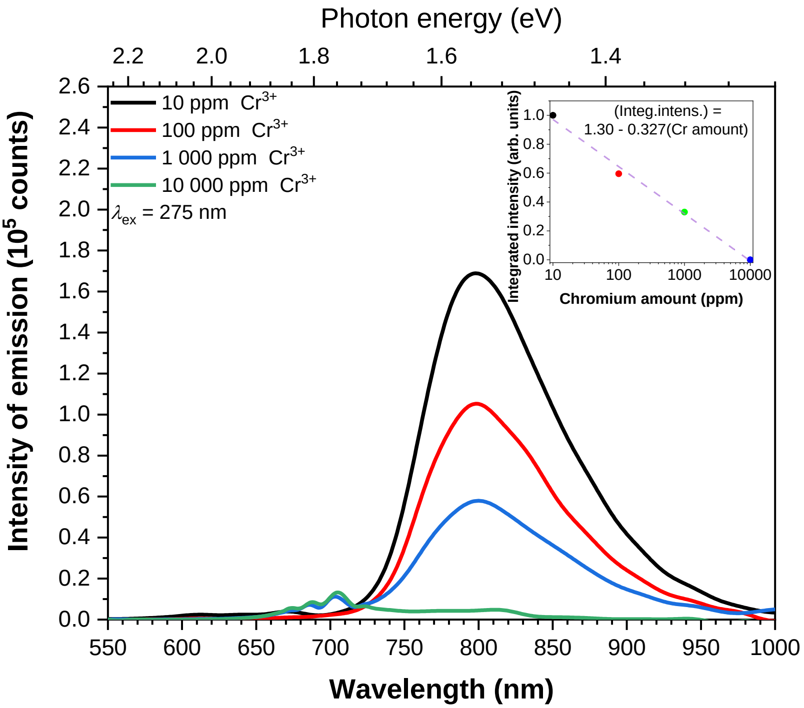

Figure 41. Photoluminescence emission spectra of samples doped with Cr^{3+} under 275 nm excitation, inset showing an exponential decrease in emission intensity with increasing concentration.

To the best of our knowledge, the concentration dependent $^4T_2 \rightarrow ^4A_2$ transitions of Cr^{3+} ions in yttrium aluminum garnet are discussed for the first time. The nature of different transitions of Cr^{3+} ions are discussed in the analysis of the works with other compounds. One way of interpreting the observation is that a part of Cr^{3+} ions might be located in a highly disordered environment e.g. amorphous or highly defective state to cause a large shift in the emission energies at room temperature [230]. The other might arise from Cr^{3+} - Cr^{3+} ion pair emission which existence as a separate phenomenon and not just energy transfer mechanism has been recently recorded in magnetoplumbite $Al_{11.88-x}Ga_xO_{19}$:$0.12Cr^{3+}$ material [231]. In our case, the change in dopant concentrations are very likely to change the local crystal environment, because of the electronegativity differences [232,233] between Al^{3+} and Cr^{3+} which are 1.513 and 1.587 respectively. The Tanabe-Sugano diagram suggests that the energy levels of Cr^{3+} in the investigated samples fluctuate around a dashed line in Figure 42. If chromium concentration is below 1000 ppm the samples exhibit emission caused by the splitting of the energy levels of dopant ions in figure assigned as type I (low crystal-field), meanwhile if the concentration of chromium ions is about 1000 ppm and more the splitting of energy levels assigned as type II (high crystal-field) predominates. Note, that the replacement of aluminum with chromium ions should slightly decrease the crystal field of the local environment causing $^4T_2 \rightarrow {}^4A_2$ transitions of Cr^{3+} ions. The observed phenomenon is quite opposite in fact, therefore additional detailed studies of the crystalline structure with synchrotron or neutron radiation are required.

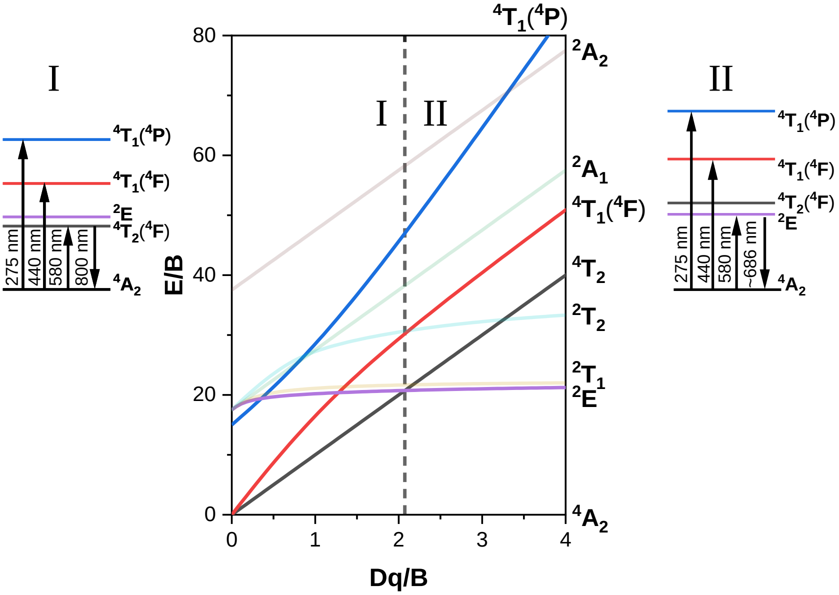

Figure 42. Tanabe-Sugano diagram and energy level diagram of chromium-doped garnets.

CONCLUSIONS

1. All of the sample glasses successfully doped with 0.2 mol–%, 0.6 mol–% and 1.0 mol–% of Eu^{3+}. It was determined that Eu^{3+} ions were positioned in low symmetry environment causing the dominant emission of $^5D_0 \rightarrow ^7F_2$ transitions. Irrespectively of the type of tetrahedral phosphate sites in glasses (Q_0, Q_1, Q_3 or Q_4) the aforementioned transition contributed more than 50% of the emission intensity in comparison the whole emission spectra.
2. As an notable composition of 50 P_2O_5 : 15 K_2O : 10 Li_2O: 10 CaO: 2 Al_2O_3: 10 ZnO : 2 B_2O_3: 1 SnO (G1) produced the highest photoluminescence intensity with all of the aforementioned dopant concentrations.
3. The study demonstrates that the substitution level in sol-gel-derived $Y_{3-x}Ln_xFe_5O_{12}$ systems depends on the lanthanide element's nature. Monophasic garnets were synthesized successfully with certain lanthanide substitutions (Pr and Nd).
4. It was demonstrated that two distinct types of chromium emission can be achieved in the yttrium aluminum garnet host by varying the dopant concentration and the wavelength of excitation. One type of emission, which is forbidden to spin, exhibits an increase in intensity with an increase in the concentration of luminescent centers. The other type of emission, which is broadband and exhibits an exponential decrease in intensity with an increase in the concentration of chromium ions, is designated as $^4T_2 \rightarrow ^4A_2$. The emission spectra can be employed to ascertain the degree of chromium contamination in YAG, given that the emission is highly sensitive to the concentration of chromium ions.

SUPPLEMENTARY MATERIAL

Appendix 1. Composition dependent Raman spectra of phosphate glasses with 1 mol -% of Eu (samples G1′−G6′). The excitation wavelength is 785 nm (3 mW).

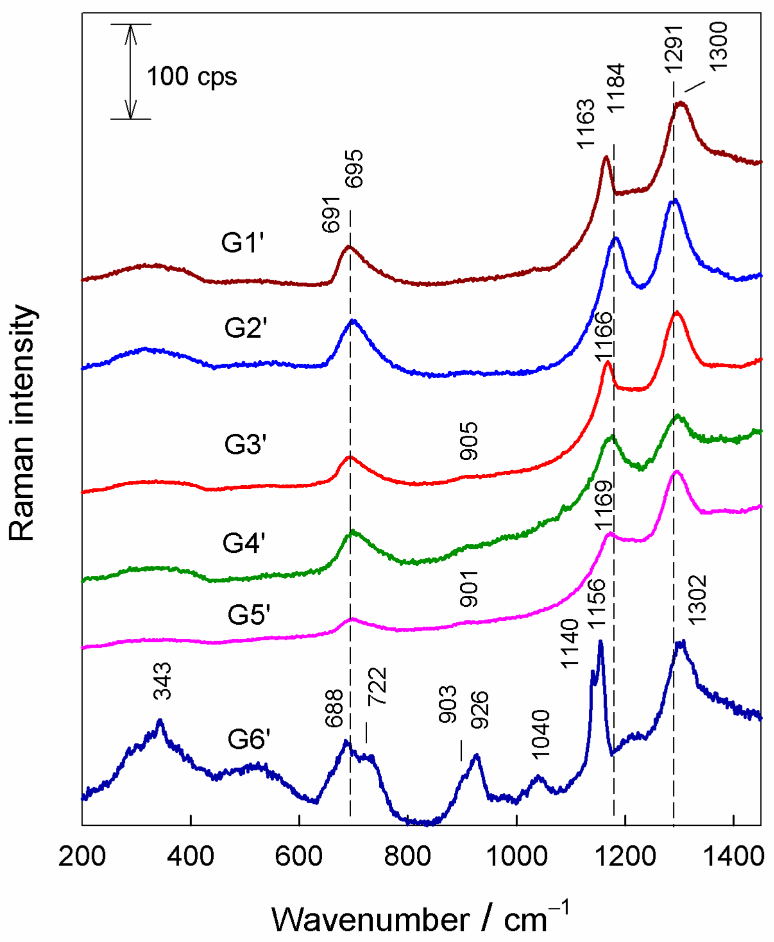

Appendix 2. Photoluminescence emission and excitation spectra where A, B, C, D, E corresponds to elemental compositions of G2’, G3’, G4’, G5’, G6’ (Table 1), respectively.

A

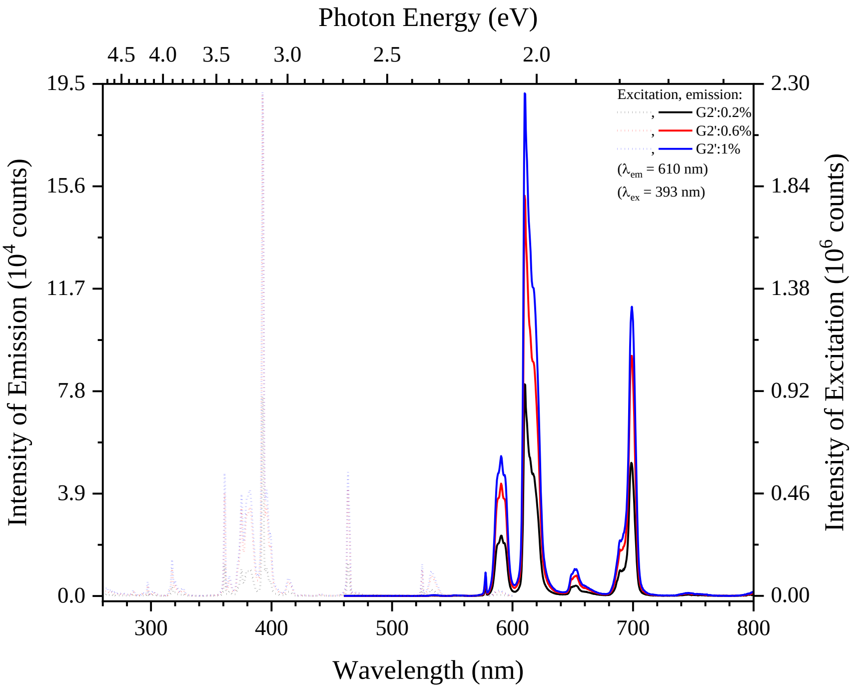

B

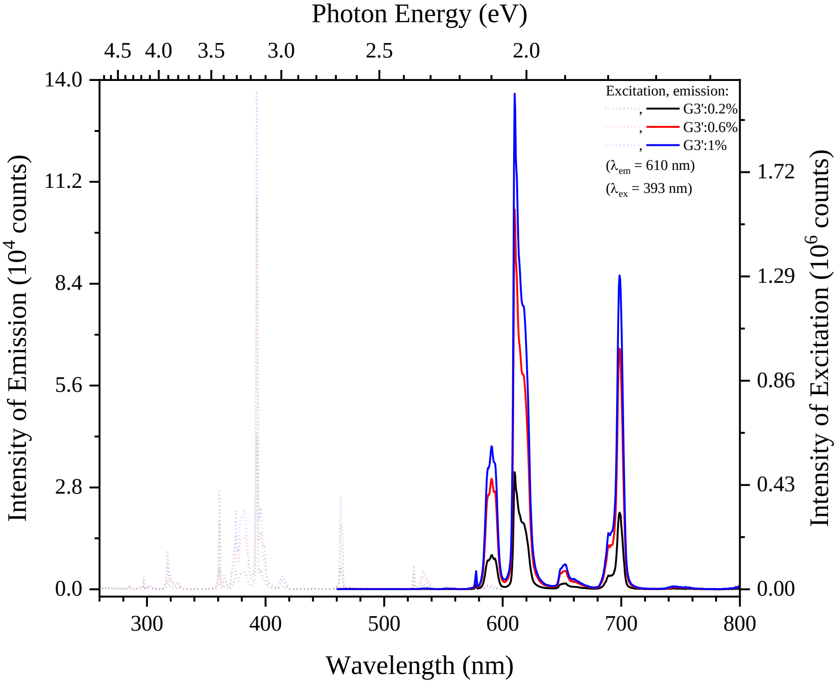

C

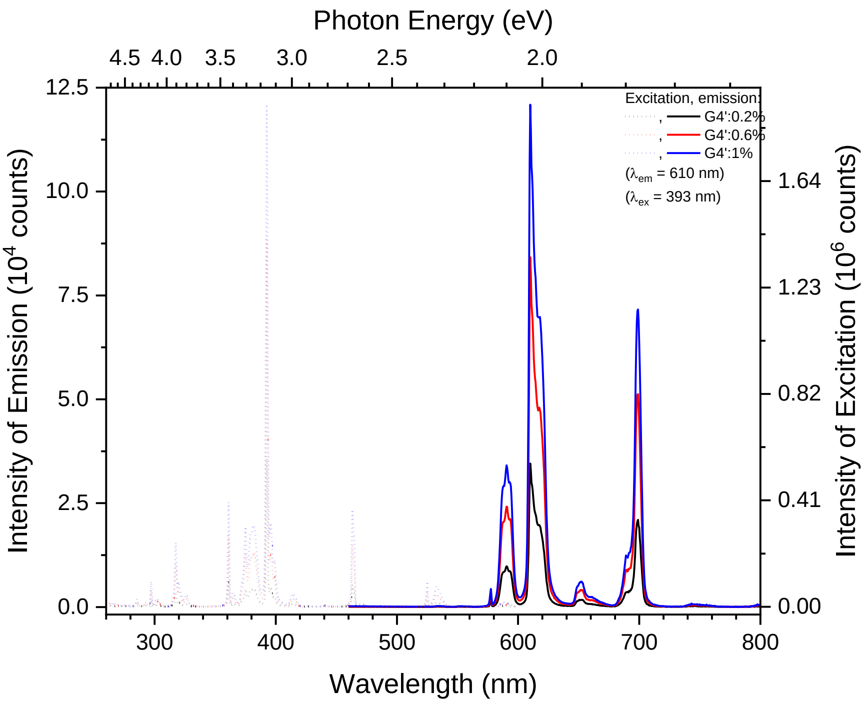
Photon Energy (eV)
4.5
4.0
3.5
3.0
2.5
2.0
Excitation, emission:
G4':0.2%
G4':0.6%
G4':1%
(λ_{em} = 610 nm)
(λ_{ex} = 393 nm)
Intensity of Emission (10^4 counts)
12.5
10.0
7.5
5.0
2.5
0.0
Intensity of Excitation (10^6 counts)
1.64
1.23
0.82
0.41
0.00
300
400
500
600
700
800
Wavelength (nm)

D

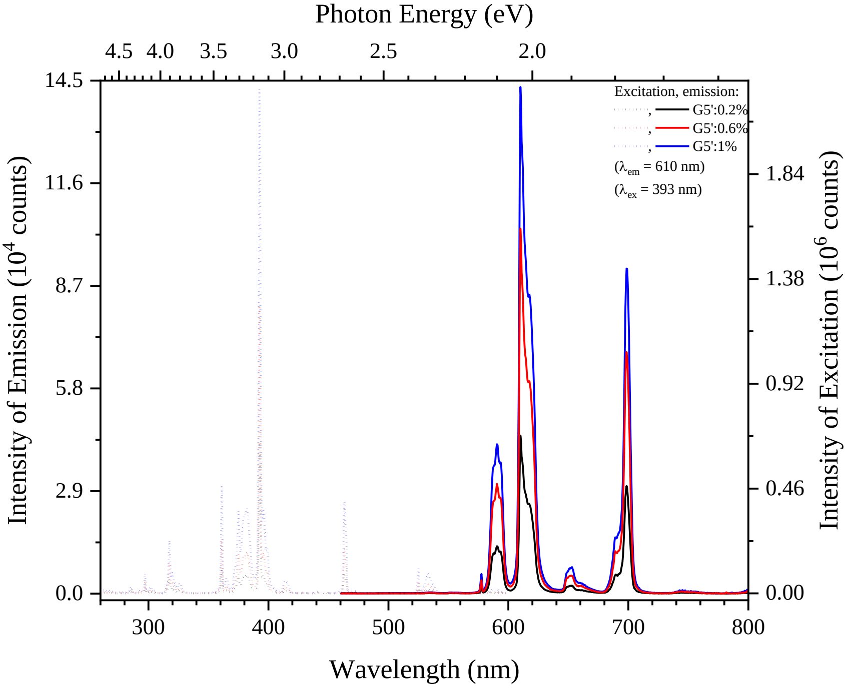
Photon Energy (eV)
4.5
4.0
3.5
3.0
2.5
2.0
Excitation, emission:
G5':0.2%
G5':0.6%
G5':1%
(λ_{em} = 610 nm)
(λ_{ex} = 393 nm)
Intensity of Emission (10^4 counts)
14.5
11.6
8.7
5.8
2.9
0.0
Intensity of Excitation (10^6 counts)
1.84
1.38
0.92
0.46
0.00
300
400
500
600
700
800
Wavelength (nm)

E

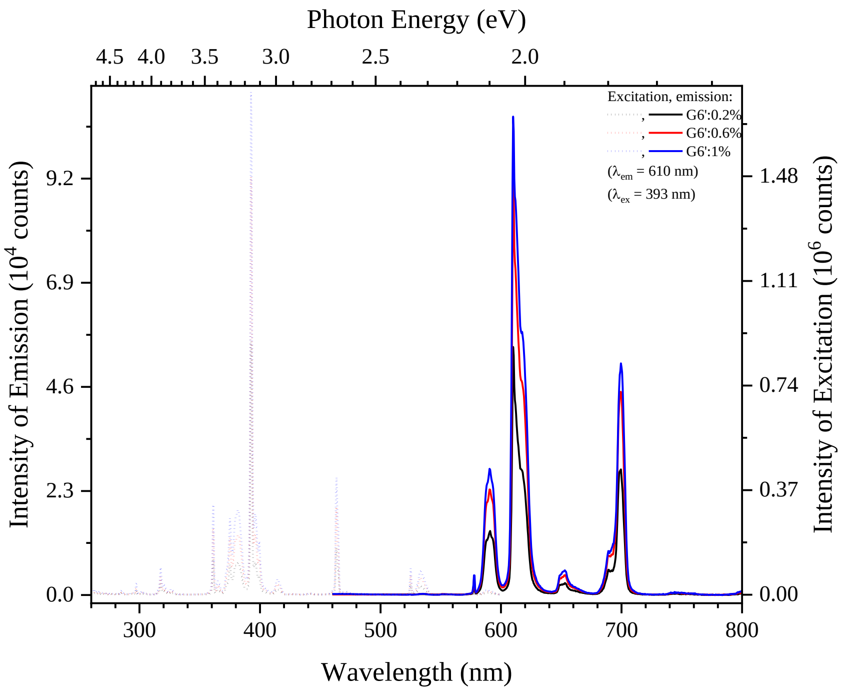

Appendix 3. XRD patterns of different glass compositions with varied Eu^{3+} amount

A

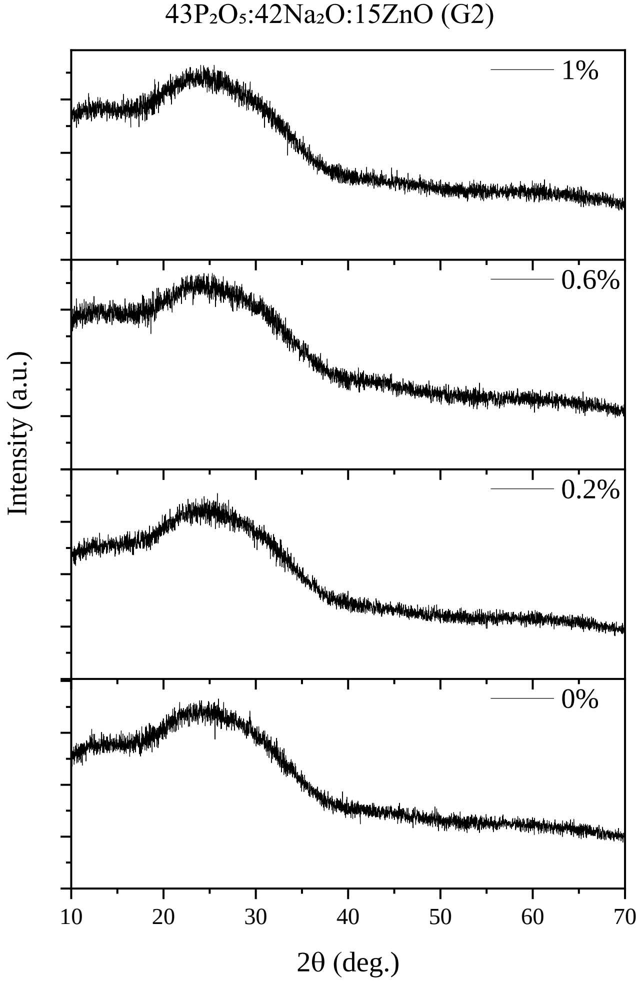
43P₂O₅:42Na₂O:15ZnO (G2)
1%
0.6%
0.2%
0%
Intensity (a.u.)
10
20
30
40
50
60
70
2θ (deg.)

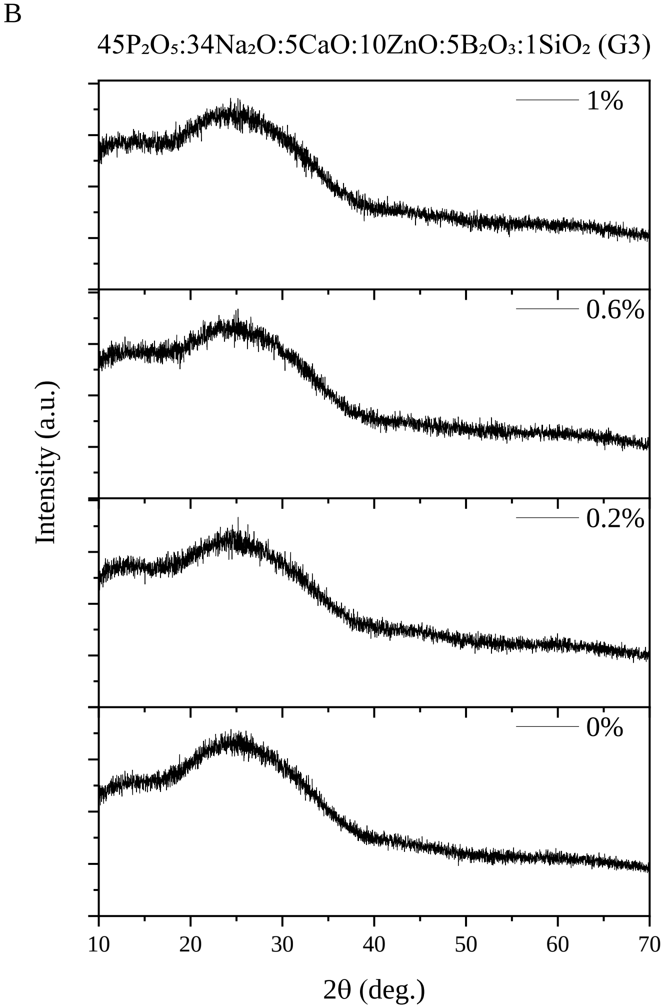
B
45P₂O₅:34Na₂O:5CaO:10ZnO:5B₂O₃:1SiO₂ (G3)
1%
0.6%
0.2%
0%
Intensity (a.u.)
10
20
30
40
50
60
70
2θ (deg.)

C

$45P_2O_5:28Na_2O:6Li_2O:1CaO:4Al_2O_3:10ZnO:5B_2O_3:1SiO_2$ (G4)

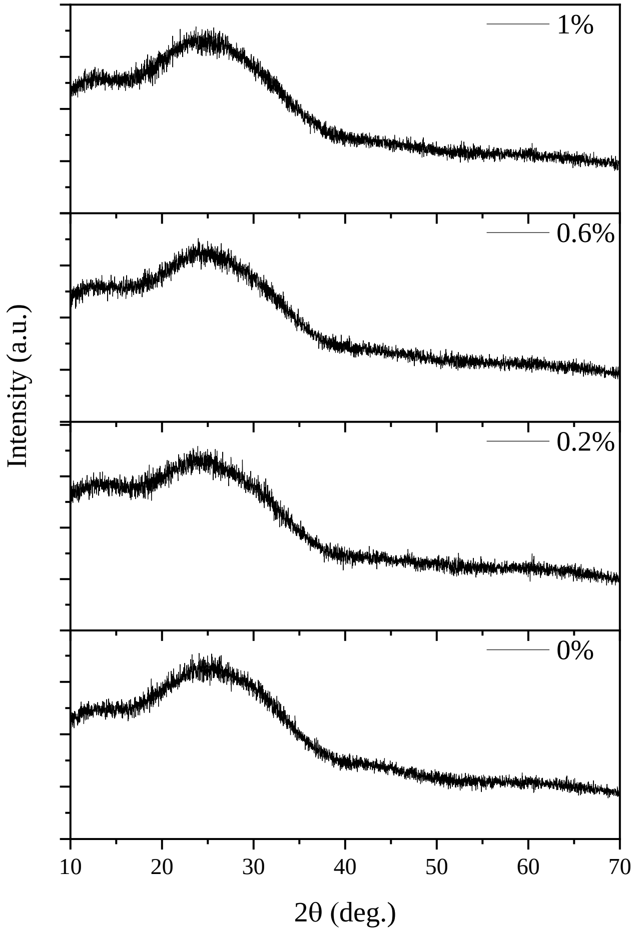

D

$45P_2O_5:28Na_2O:6\ Li_2O:4CaO:1Al_2O_3:10ZnO:5B_2O_3:1SiO_2$ (G5)

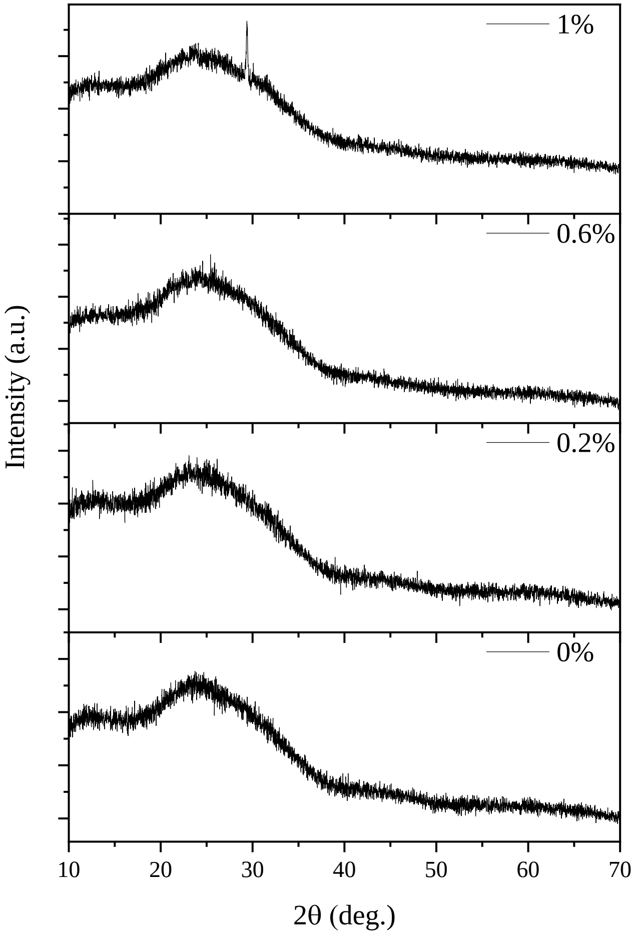

E

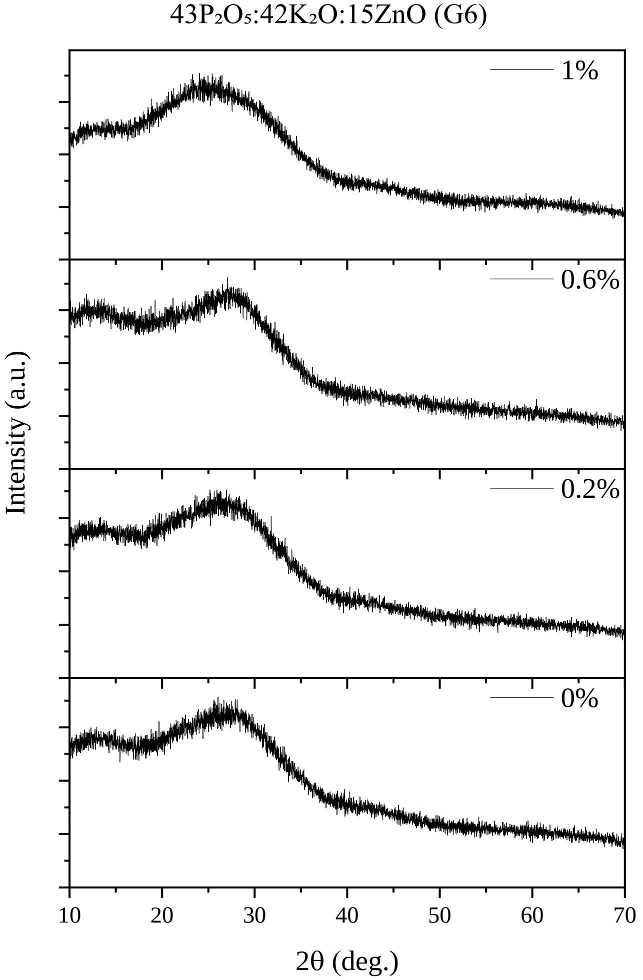

Appendix 4. Lattice parameters provided by Rietveld refinement data

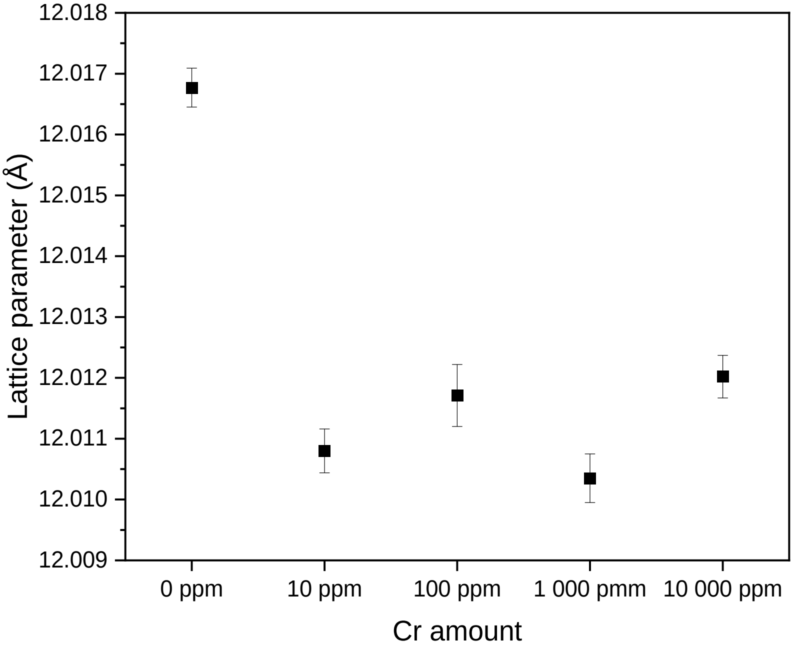

Appendix 5. Rietveld refinement data of undoped sample

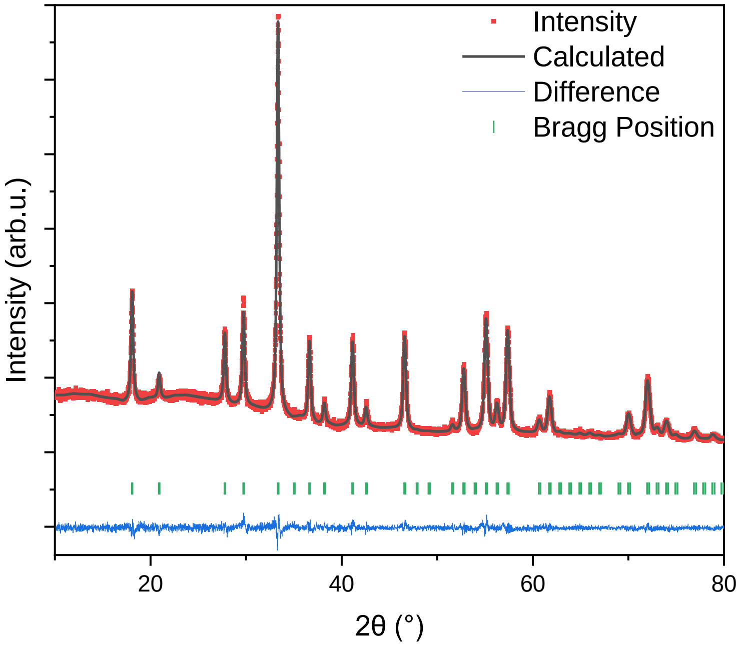

Appendix 6. Rietveld refinement data of sample doped with 10 ppm of Cr^{3+}

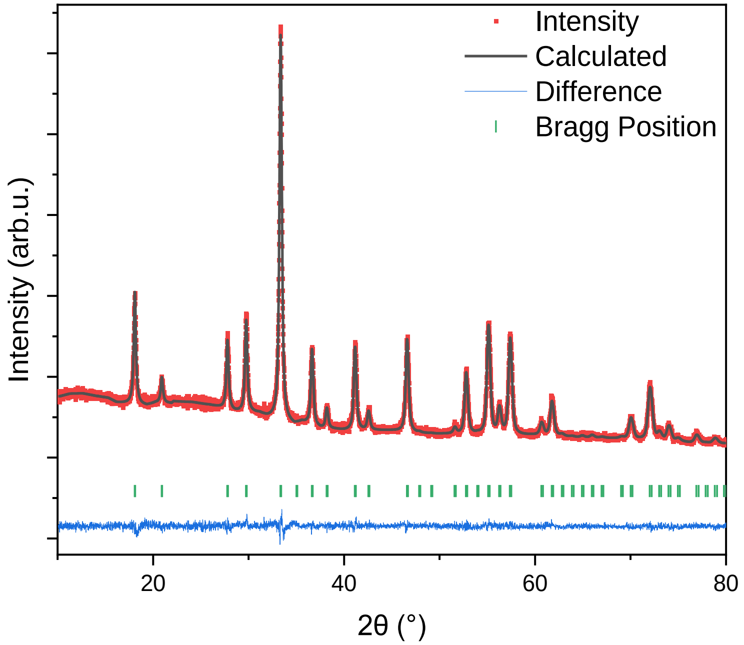

Appendix 7. Rietveld refinement data of sample doped with 100 ppm of Cr^{3+}

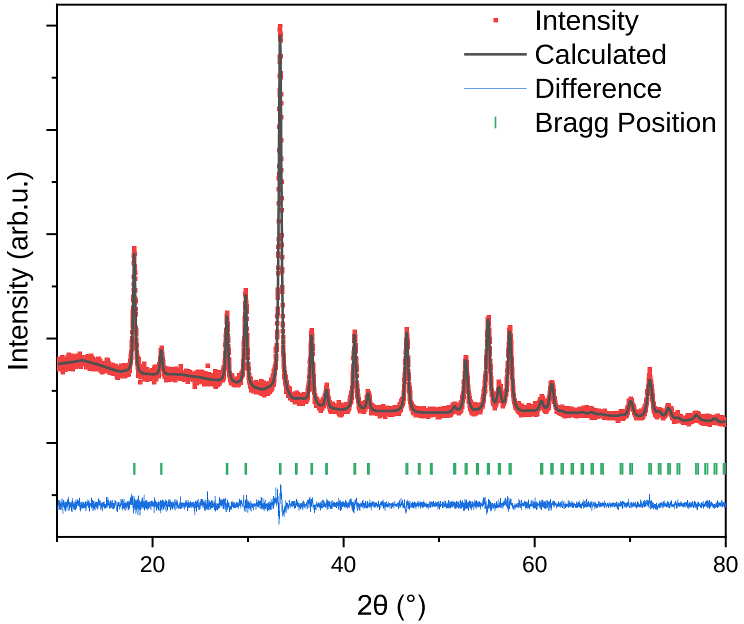

Appendix 8. Rietveld refinement data of sample doped with 1 000 ppm of Cr^{3+}

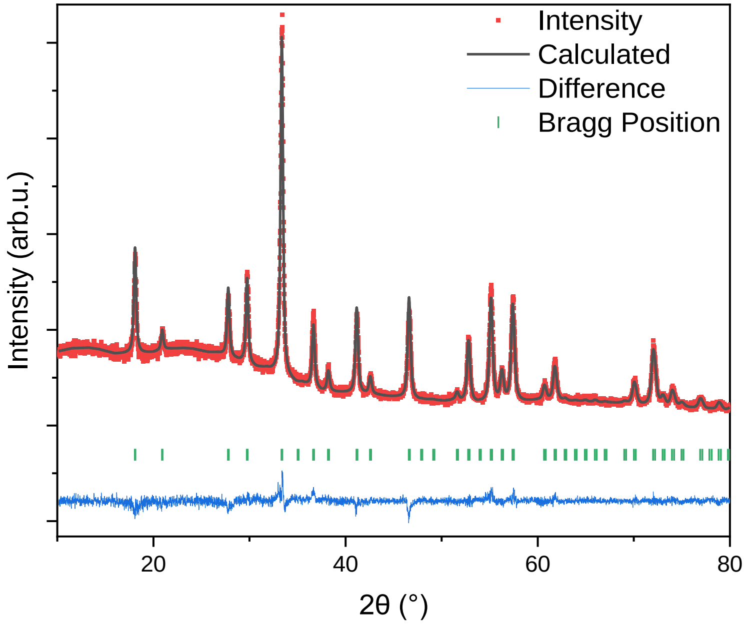

Appendix 9. Rietveld refinement data of sample doped with 10 000 ppm of Cr^{3+}

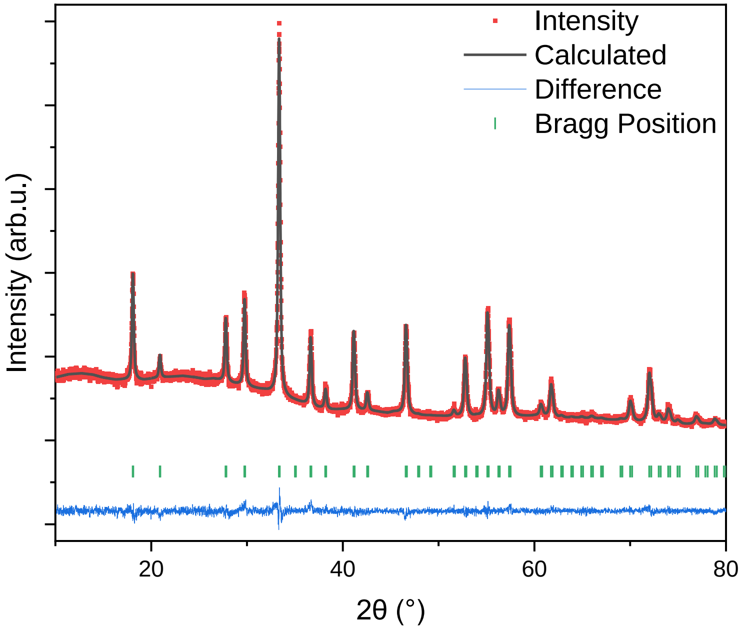

Appendix 10. Rietveld refinement data of bond lengths. Cr^{3+} amount in material is displayed in ppm

	0 ppm	10 ppm	100 ppm	1 000 ppm	10 000 ppm
Y-O	2.3252 Å 2.4404 Å	2.3243 Å 2.4407 Å	2.3064 Å 2.4446 Å	2.2955 Å 2.4732 Å	2.3169 Å 2.4456 Å
Al-O tetrahedral	1.7596 Å	1.7565 Å	1.7682 Å	1.7437 Å	1.7594 Å
Al(Cr)-O octahedral	1.9308 Å	1.9308 Å	1.9236 Å	1.9321 Å	1.9277 Å

ACKNOWLEDGEMENTS

I'm extremely grateful to academic supervisor Prof. Dr. Ramūnas Skaudžius for his patience and guidance without which this dissertation would have never been completed.

I'd like to acknowledge and express gratitude to Prof. Habil. Dr. Gediminas Niaura for Raman spectroscopy measurements, Dr. Kęstutis Mažeika and Habil. Dr. Dalis Baltrūnas for magnetic measurements.

I would like to extend my sincere thanks to all the wonderful colleagues and friends who were constantly bugging me with question will I ever finish the dissertation.

Finally, I would be remiss in not mentioning a bunch of special people (you know who you are) for helping me to get through the tough times and wish them all the best in their lives.

LIST OF PUBLICATIONS

Publications related to dissertation

1. Norkus, Mantas; Skaudžius, Ramūnas. Enhanced NIR region emission of chromium by changing the chromium concentration in yttrium aluminum garnet (YAG) host matrix // Journal of alloys and compounds. Lausanne: Elsevier Science. 2022, vol. 908, art. no. 164601, p. [1-5]. ISSN: 0925-8388; eISSN: 1873-4669; DOI: 10.1016/j.jallcom.2022.164601.
2. Norkus, Mantas; Laurikėnas, Andrius; Vištorskaja, Diana; Mažeika, Kęstutis; Baltrūnas, Dalis Antanas; Skaudžius, Ramūnas; Beganskienė, Aldona; Kareiva, Aivaras. Investigation of substitution effects of the first four lanthanides (La, Ce, Pr and Nd) in yttrium iron garnet // Journal of alloys and compounds. Lausanne: Elsevier Science BV. 2022, vol. 903, art. no. 163978, p. [1-12]. ISSN: 0925-8388; eISSN: 1873-4669; DOI: 10.1016/j.jallcom.2022.163978.
3. Norkus, Mantas; Skruodienė, Monika; Niaura, Gediminas; Šarakovskis, Anatolijs; Skaudžius, Ramūnas. New low-temperature phosphate glasses as a host for europium ions // Journal of non-crystalline solids. Amsterdam: Elsevier. 2021, vol. 569, art. no. 120966, p. [1-7]. ISSN: 0022-3093; eISSN: 1873-4812; DOI: 10.1016/j.jnoncrysol.2021.120966.

Other publications

4. Petrulionienė, Toma; Murauskas, Tomas; Norkus, Mantas; Naujalis, Evaldas. Emission of additives and degradation products from commercial polypropylene, polyethylene and their composite packages // Chemija. Vilnius: Lithuanian Academy of Sciences. 2023, vol. 34, no. 2, p. 99-111. ISSN: 0235-7216; eISSN: 2424-4538; DOI: 10.6001/chemija.2023.34.2.4.
5. Karalkevičienė, Rasa; Briedytė, Greta; Murauskas, Tomas; Norkus, Mantas; Žarkov, Aleksej; Yang, Jen-Chang; Kareiva, Aivaras. A novel method for the formation of bioceramic nano-calcium hydroxyapatite coatings using sol-gel and dissolution-precipitation processing // Chemija. Vilnius: Lietuvos mokslų akademijos leidykla. 2022, vol. 33, no. 2, p. 27-34. ISSN: 0235-7216; eISSN: 2424-4538; DOI: 10.6001/chemija.v33i2.4705.

LIST OF CONFERENCES

1. Norkus, Mantas; Aglinskaitė, Justina; Katelnikovas, Artūras; Vitta, Pranciškus; Skaudžius, Ramūnas. One-step phosphor in glass synthesis and characterization. Chemistry and chemical technology, 2019.
2. Norkus, Mantas; Niaura, Gediminas; Skaudžius, Ramūnas. One-Step Phosphor in Glass Synthesis and characterization // Functional Materials and Nanotechnologies, 2020
3. Norkus, Mantas; Niaura, Gediminas; Skaudžius, Ramūnas. Europium Doped Luminescent Glass Synthesis and Characterization. Nanostructured Bioceramic Materials, 2020.
4. Norkus, Mantas; Skaudžius, Ramūnas. Anomalous optical properties of yttrium aluminum garnet doped with chromium. Chemistry and chemical technology, 2021.
5. Norkus, Mantas; Skaudžius, Ramūnas. Novel phosphate glass matrices as a potential host for luminescent rare earth ions. Advanced materials and technologies, 2021.

CURRICULUM VITATE

Personal Information	
Name, Surname	Mantas Norkus
Education	
1999 September – 2009 May	Vinco Kudirkos Primary School
2009 September – 2011 May	Radviliskis Vaizgantas Gymnasium
2011 September – 2015 May	Bachelor of Chemistry, Faculty of Chemistry, Vilnius University
2015 September – 2017 May	Master‘s Degree in Physical Sciences, Faculty of Chemistry and Geosciences, Vilnius University
2017 October – 2021 September	Doctoral Studies, Faculty of Chemistry and Geosciences, Vilnius University
Work Experience	
2015 December – 2017 June	**Center for Physical Sciences and Technology** – Engineer
2017 September – 2019 June	**Vilnius University** – Laboratory assistant/senior specialist
2017 February – 2022 September	**National Public Health Laboratory** – Chemistry specialist
2022 September – Now	**National Public Health Laboratory** – The Head of Instrumental Testing Subdepartment in Chemical Testing Department
2023 March – Now	**Lithuanian Standards Board** – Officer of the Technical Committee TK75 Cosmetics and Surface Active Agents

SANTRAUKA

ĮVADAS

Nuolat besikeičiančioje pažangių keraminių medžiagų srityje liuminescencinio stiklo ir granatų sintezė bei tyrimai atsiduria mokslinių tyrimų dėmesio centre, nes naujai atrandamos šių medžiagų taikymo sritys. Žengiant į naująjį amžių, akivaizdu, kad telekomunikacijoms tenka esminis vaidmuo, ypač aštuntojo dešimtmečio pabaigoje perėjus nuo varinių laidų prie šviesolaidinių ryšių. Šis revoliucinis metodas, pradėjęs naują erą optinio stiklo, ekranų, optinių jutiklių ir kietakūnių lazerių taikymui optoelektronikos srityje, apima informacijos perdavimą infraraudonųjų spindulių impulsais šviesolaidžiais [1,2].

Vis didėjanti optikai tinkančių stiklų paklausa, ypač legiruotų retųjų žemių (RE) elementų jonais, rodo nuolatinę novatoriškų sprendimų paiešką. Optiniai stiklai, ypač fosfatiniai stiklai, tampa pageidaujama optinių medžiagų terpe dėl savo pranašumų kristalinių medžiagų atžvilgiu. Lengvas paruošimas, įvairios produkto formos ir galimybė įterpti liuminescenciją aktyvinančius RE jonus paverčia šias medžiagas neatsiejama optoelektroninio arsenalo dalimi [3-7]. Tačiau, nepaisant šių privalumų, plačiai naudoti RE jonus trukdo koncentracinis gesinimas. Kai virš tam tikros ribos padidėjus RE oksido koncentracijai, sumažėja fluorescencijos gyvavimo trukmė, o šis reiškinys turi neigiamą poveikį lazerinėms savybėms [3-7].

Iš įvairių metalų metafosfatų sudarytas fosfatinis stiklas yra unikalus savo sudėtimi. Tokio stiklo formuojantis struktūrinis pagrindas yra P_2O_5. Palyginti su boratiniais, silikatiniais ir kitais stiklais, išskirtines fosfatinių stiklų chemines ir fizikines savybes lemia skirtingi stiklo tinklą formuojantys elementai. Silikatiniai ir boratiniai stiklai, kurie tirpsta vandenilio fluorido rūgštyje, smarkiai skiriasi nuo fosfatinių stiklų, kurie yra labai atsparūs šiai rūgščiai. Kitas esminis skirtumas – lydymosi temperatūra, kur borosilikatinio stiklo temperatūrinė riba yra aukštesnė nei silikatinių ar fosfatinių stiklų [2,8-13].

Dėl puikių RE legiruoto fosfatinio stiklo savybių jis ypač tinka šviesolaidžių gamyboje. Šioje srityje, siekiant užtikrinti didelį lazerio patikimumą ir ilgalaikį stabilumą, būtinas kompaktiškumas, aukšta spindulio kokybė veikiant vienmodžiu režimu ir puikus šilumos išsklaidymas. Ieškoma aktyviosios terpės, pasižyminčios dideliu optiniu stiprinimu per trumpą ilgio vienetą. Tai itin svarbu efektyvių prietaisų sukūrimui. Kartu norima sumažinti netiesinius optinius efektus. Dažnas pasirinkimas legiravimui yra Eu^{3+} jonai, dėl $^5D_0 \rightarrow {}^7F_J$ perėjimų. Šie elektronų šuoliai pasižymi siauromis fluorescencijos smailėmis, ilga gyvavimo trukme, kuri priklauso nuo europio koncentracijos matricoje [14-17].

Kadangi pažangių keraminių medžiagų poreikis vis didėja, verta paminėti itrio aliuminio granatą. Jis naudojamas kaip keraminis optinis oksidas, kurio nominali sudėtis yra $Y_3Al_5O_{12}$ (YAG). Būdamas optiškai izotropinis, YAG virsta universalia medžiaga, kai yra legiruojamas įvairiais trivalenčiais jonais, ypač lantanoidais. Ši transformacija atvėrė kelią nepaprastai sėkmingiems moksliniams tyrimams ir komerciniam taikymui. Pavyzdžiui, YAG:Nd, YAG:Er naudojami kietojo kūno lazeriuose. YAG:Ce panaudojamas katodiniuose kineskopuose ir šviesos dioduose [18-21].

Monokristalinės lazerinės medžiagos kelia specifinius technologinius iššūkius. Tai siejama su lydalo temperatūros svyravimais ir nehomogenišku optiškai aktyvių jonų pasiskirstymu. Dalinai problemos išspręstos 1995 m. pradėjus naudoti polikristalinius YAG:Nd keramikos lazerius. Šis pasiekimas ne tik pademonstravo lygiavertiškumą ar net pranašumą monokristalių lazerių atžvilgiu, bet ir atvėrė kelius polikristalinio YAG, kaip perspektyvaus pakaitalo, tyrimams. Pradėta didesnio mastelio sudėtingos geometrijos daugiasluoksnių struktūrų gamyba [18,22].

Šis tyrimas apima chromu legiruoto YAG liuminescencines savybes ir pateikia išvadas, papildančias literatūroje aprašytus liuminescencijos dėsningumus, priklausomus nuo koncentracijos. YAG gerai žinomas kaip matrica, kur Cr^{3+} jonai pakeičia oktaedriškai koordinuotus Al^{3+} jonus. Tai smarkiai pakeičia liuminescencines savybes [23-31]. Derinant polikristalinius keramikos miltelius su priimančiąja stiklo matrica, praktiškai sprendžiamas produkto atsiperkamumo klausimas [32,33].

Darbe pateikiama ir trečia tyrimų sritis, apibūdinanti nanoferitus. Šios magnetinės nanodalelės pritaikomos elektronikos, biotechnologijų ir medicinos srityse. Jos pasižymi unikaliomis savybėmis, pavyzdžiui, ferimagnetizmu, puikiu atsparumu radiaciniams pažeidimams bei energijos perdavimo efektyvumu. Itrio geležies granatas ($Y_3Fe_5O_{12}$; YIG), turintis kubinę granato struktūrą, yra plačiai tiriamas dėl savo magnetinių, magnetooptinių, šiluminių, elektrinių ir mechaninių savybių. Dėl lantanoidais pakeistų granatų ($Ln_3Fe_5O_{12}$) universalumo, jie yra tinkami įvairių prietaisų gamybai. Taip pat naudojami jutikliuose, lazeriuose, fosforescencinių šaltinių ir mikrobangų prietaisuose [34-42].

Itrio geležies granatų savybės, priklauso nuo valentiškai nekompensuoto legiravimo, geležies pakeitimo tetraedrinėse ir oktaedrinėse pozicijose arba itrio pakeitimo dodekaedrinėse pozicijose. Geležis arba itris pakeičiamas kitais įvairiais metalų katijonais. Ši galimybė modifikuoti struktūrą yra labai svarbi norint pritaikyti geležies granatų savybes konkrečioms reikmėms.

Geležies granatams gauti buvo ištirti įvairūs sintezės metodai – nuo kietosios būsenos reakcijų iki zolių-gelių sintezės. Sintezės metodo pasirinkimas yra labai svarbus, nes nuo jo priklauso gaunamos magnetinės savybės: soties įmagnetėjimas ir Neel temperatūra [43-47].

Disertacijos tikslas – sukurti liuminescencinio stiklo, kurio struktūroje yra Eu^{3+} jonų, ir susintetinti keraminius granatus (YAG:Cr, YIG, legiruotą La, Ce, Pr, Nd) bei ištirti jų savybes.

Šio tyrimo uždaviniai yra šie:

- nustatyti galimą fosfatinio stiklo, legiruoto retųjų žemių jonais, struktūrą;
- apibūdinti legiruoto YIG savybes, įvertinant įterpiamų elementų koncentracijos įtaką faziniam grynumui;
- nustatyti ir apibūdinti YAG:Cr liuminescencijos priklausomybę nuo legiruojančio jono koncentracijos.

Šiame darbe aprašomas sudėtingas liuminescencinių stiklų ir granatų sintezės procesas bei pabrėžiama didžiulė jų svarba platesniame pažangiųjų keraminių medžiagų kontekste. Sujungiant optinio stiklo, YAG ir nanoferitų sritis, siekiama prisidėti prie optoelektroninių technologijų kūrimo plėtros. Kruopščiai tiriant šias medžiagas siekiama atskleisti naujas taikymo galimybes, spręsti iššūkius ir skatinti mokslines inovacijas. Tai praplečia įprastinių medžiagų galimybių ribas ir suformuoja kitokį požiūrį į dirbtines medžiagas.

Siekiant išsiaiškinti, ar stiklas nesikristalizuoja po greito lydalo atšaldymo atlikti rentgeno spindulių difrakciniai tyrimai. 43 paveiksle pateiktose nelegiruotų bandinių rentgeno difraktogramose nenustatyta smailių, kurias būtų galima priskirti tam tikram kristalinės fazės susidarymui. Didelio intensyvumo fono linija taip pat leidžia numanyti amorfinę bandinių prigimtį. Išskirtinai tik nelegiruotame G1 mėginyje, galima stebėti vieną nedidelio intensyvumo ir gerai apibrėžtą difrakcijos maksimumą ties 2θ = 22,28°, kurį, kaip galima numanyti pagal stiklo sudėtį, galima priskirti alavo pirofosfato (SnP_2O_7, PDF: 00-029-1352) kristalizacijai (43 paveikslas).

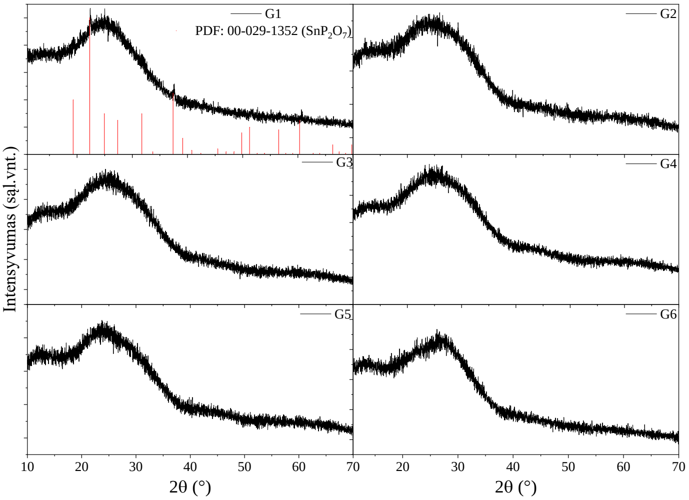

43 paveikslas. Skirtingų nelegiruoto stiklo sudėčių rentgeno spindulių difraktogramos.

Kadangi stiklai yra amorfinės medžiagos, detalesnei jų struktūrai nustatyti reikalingas papildomas metodas, toks kaip Ramano spektroskopija. Šis metodas gali suteikti išsamios informacijos apie trumpojo nuotolio molekulinę struktūrą arba vietinę simetriją. Pagrindinius fosfatinių stiklų struktūrinius elementus sudaro P-O-P tinklas ir PO_n grupės. Pagal deguonies atomų skaičių fosfato grupėje, dalyvaujančių tinklo susidaryme, galima išskirti keturis skirtingus tetraedrinius struktūrinius vienetus (44 paveikslas) [197-199].

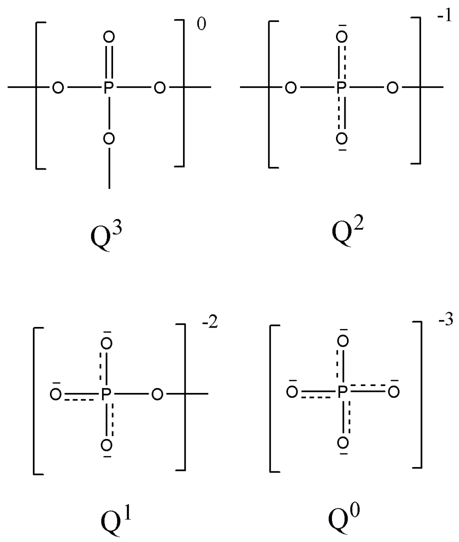

44 paveikslas. Tetraedriniai struktūriniai vienetai fosfatiniuose stikluose.

Q^0 vieta sudaryta iš $(PO_4)^{3-}$ struktūros be deguonies atomų, susijungusių su fosfatiniu tinklu, Q^1 vieta sudaryta iš $[-(O)PO_3]^{2-}$ struktūros su vienu deguonies atomu, susijungusiu su fosfatiniu tinklu. Q^2 vieta sudaryta iš $[-(O)_2PO_2]^-$ struktūros su dviem deguonies atomais, susijungusiais su fosfatiniu tinklu, o Q^3 vieta sudaryta iš $[-(O)_3PO]$ struktūros su trimis deguonies atomais, susijungusiais su fosfatiniu tinklu. Skirtingos sudėties nelegiruotų fosfatinių stiklų (Lentelė 10) Ramano spektrai pateikti 45 paveikslase. Intensyvi ir gana plati juosta, matoma G1-G6 bandinių aukštųjų dažnių srityje ties 1291-1305 cm^{-1}, priklauso Q^3 tetraedrinės struktūros terminalinės P=O grupės simetriniam valentiniam virpesiui, $\nu_s(P{=}O)$ [197], prie kurio šiek tiek prisideda Q^2 tetraedrinės vietos nesurištos PO_2 grupės asimetrinis valentinis virpesys, $\nu_{as}(PO_2)$ [198,200]. Dėl fosfatinio tinklo depolimerizacijos ši juosta pasislenka į žemesnes bangas, o tai nulemia P=O ryšio ilgio padidėjimą, nes sumažėja vidutinis π ryšio laipsnis [197,200]. Todėl gryname P_2O_5 stikle $\nu_s(P{=}O)$ juosta gali būti matoma ties 1390 cm^{-1} [197].

Lentelė 10. Pradinės stiklo sudėtys išreikštos mol % kiekvieno elemento oksidu. Stiklai buvo legiruoti 0,2%, 0,6%, ir 1,0% of Eu^{3+} priklausomai nuo pradinės jų sudėties

Mėg. pavad.	P_2O_5 mol %	Na_2O mol %	K_2O mol %	Li_2O mol %	CaO mol %	Al_2O_3 mol %	ZnO mol %	B_2O_3 mol %	SiO_2 mol %	SnO mol %
G1	50	–	15	10	10	2	10	2	–	1
G2	43	42	–	–	–	–	15	–	–	–
G3	45	34	–	–	5	–	10	5	1	–

Mėg. pavad.	P_2O_5 mol %	Na_2O mol %	K_2O mol %	Li_2O mol %	CaO mol %	Al_2O_3 mol %	ZnO mol %	B_2O_3 mol %	SiO_2 mol %	SnO mol %
G4	45	28	–	6	1	4	10	5	1	–
G5	45	28	–	6	4	1	10	5	1	–
G6	43	–	42	–	–	–	15	–	–	–

Šiuo atveju, į stiklus pridėjus šarminių metalų katijonų, juosta pasislenka daugiau kaip 80 cm^{-1} (45 paveikslas). G1-G5 bandinių spektruose matoma plati ir asimetriška juosta ties 692-696 cm^{-1} yra susijusi su P-O-P tinklo simetriniu valentiniu virpesiu ν_s(POP) [197]. Aukštesnio dažnio pusėje esantis petys priklauso tos pačios grupės asimetriniam valentiniam virpesiui, ν_{as}(POP) [197]. Grandinės viduje esančio ν_s(POP) režimo viršūnės padėtis nėra labai jautri bandinių sudėčiai (45 paveikslas).

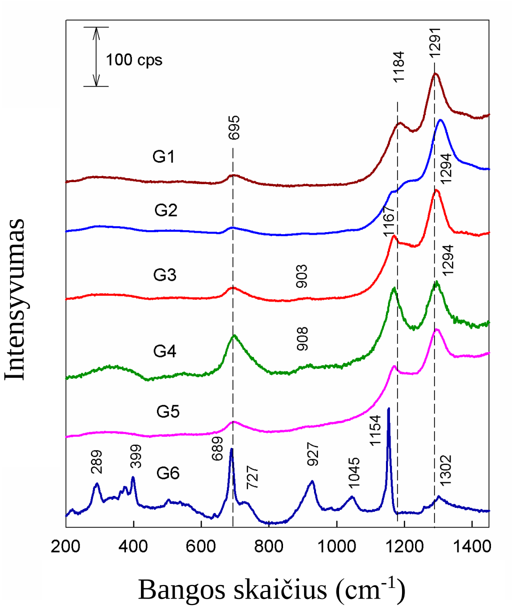

45 paveikslas. Ramano spinduliuotės spektrų priklausomybė nuo stiklo, nelegiruoto Eu (mėginiai G1−G6), sudėties. Sužadinimo bangos ilgis 785 nm (3 mW).

Labai jautri struktūrai juosta yra susijusi su tinklo neformuojančių deguonies PO_2 grupių simetriniais valentiniais virpesiais Q^2 tetraedro vietoje, $\nu_s(PO_2)$ [197]. Šios modos padėtis priklauso nuo katijono: mažėjant katijono elektroneigiamumui, dažnis mažėja [197,201]. Galima išskirti du $\nu_s(PO_2)$ modų tipus; aukštesnio dažnio juostos įtemptoje tetraedrinėje struktūroje (1180-1219 cm^{-1}) ir žemesnio dažnio modos neįtemptoje Q^2 tetraedrinėje struktūroje (1154-1171 cm^{-1}) [197,202]. Vibracinių juostų priskyrimai, pagrįsti ankstesniais tyrimais aprašytais literatūroje [197-210]. Nagrinėjamų bandinių Ramano smailių padėtys pateiktos 11 lentelėje. Sudėties nulemti fosfatinės grupės valentinių virpesių juostų parametrų pokyčiai aiškiau matomi 46 paveiksle. Ramano spektrai atskleidžia įtemptą Q^2 struktūrą G1, G2 ir G3 bandiniuose. Čia $\nu_s(PO_2)$ juostų smailės yra atitinkamai 1184, 1207 ir 1219 cm^{-1}. G2-G5 pavyzdžiai pasižymi neįtempta $\nu_s(PO_2)$ juosta ties 1160-1170 cm^{-1} (Lentelė 11). Taigi G2 ir G3 bandiniai pasižymi tiek įtempta, tiek neįtempta Q^2 tetraedrine struktūra, o G4 ir G5 bandiniuose aptikta tik neįtempta struktūra. Analizuojant ν_s(P=O) juostą matyti, kad G2 bandinyje yra terminalinė fosfatinė grupė Q^3 tetraedrinėje vietoje su trumpiausiu P=O ryšio ilgiu, nes stebimas didžiausias atitinkamas valentinio virpesio dažnis (1305 cm^{-1}) (11 lentelė).

Lentelė 11. Ramano juostų viršūnių padėtys (cm^{-1}) skirtingos sudėties fosfatinių stiklų spektruose.

Vibracinė moda	Fosfatinio stiklo mėginys					
	G1	G2	G3	G4	G5	G6
ν_s(P=O) terminalinio Q^3 tetraedre; $\nu_{as}(PO_2)$ į tinklo struktūrą neįeinančių deguonies atomų Q^2 tetraedro.	1291 vs (1300 vs)	1305 vs (1290 vs)	1294 vs (1294 vs)	1294 vs (1295 s)	1294 vs (1294 vs)	1302 w (1302 vs)
$\nu_s(PO_2)$ patiriantys įtempimus, į tinklo struktūrą neįeinančių deguonies atomų Q^2 tetraedre	1184 vs (1217 w)	1207 w (1180 vs)	1219 w	–	–	–
$\nu_s(PO_2)$ į tinklo struktūrą neįeinančių deguonies atomų Q^2 tetraedre	– (1163) vs	1160 w	1167 m (1166 m)	1166 vs (1171 vs)	1170 m (1169 m)	1154 vs, 1139 vw (1156 vs, 1140 s)
ν_{as}(POP); $\nu_s(PO_4^{3-})$ į tinklo struktūrą neįeinančių deguonies atomų Q^0 tetraedre	–	–	903 w (905 w)	908 w	899 vw (901 vw)	927 s (926 m, 903 w)
ν_s(POP)	695 m (691 m)	692 m (699 m)	693 m (694 m)	697 m (700 m)	696 m (697 m)	689 s (688 m)

Priskyrimai remiantis nuorodomis: [2–4,8–14,211–213]; Sutrumpinimai: vs, labai stiprus; s, stiprus; m, vidutinis; w, silpnas; vw, labai silpnas; ν_s, simetriniai valentiniai virpesiai; ν_{as}, asimetriniai valentiniai virpesiai.

G6 mėginio Ramano spektre (45 paveikslas) matomos kelios siauros juostos, esančios ties 1154, 689 ir 399 cm^{-1}. Čia nematyti intensyvaus ir plataus ruožo ties 1290 cm^{-1}, susijusio su ν_s(P=O) moda. Vietoj to matomos kelios labai mažo intensyvumo smailės ties 1260 ir 1302 cm^{-1}. Šios juostos greičiausiai yra susijusios su nesurištų PO_2 grupių asimetriniais valentiniais virpesiais. Taigi šiam bandiniui būdingos Q^3 tetraedrinės vietos nėra. Mažo intensyvumo juosta ties 1045 cm^{-1} yra susijusi su nesurištos PO_3 grupės simetriniais valentiniais virpesiais [203]. Ši juosta rodo, kad šiame bandinyje yra Q^1 tetraedrinė pozicija. Nedidelio kiekio nesurištų fosfato grupių buvimas Q^0 tetraedrinėse pozicijose gali būti matomas iš simetrinių valentinių virpesių $\nu s(PO_4^{3-})$ juostos ties 927 cm^{-1} (45 paveikslas) [203-205,210]. Arba ši juosta gali būti susijusi su asimetriniais P-O-P tinklo valentiniais virpesiais [203,209]. G6 bandinio fosfatų Ramano juostos, lyginant su kitais bandiniais, yra siauresnės (45 paveikslas). Pavyzdžiui, G4 bandinio $\nu s(PO_2)$ juostos, esančios 1166 cm^{-1}, pusplotis (FWHM) yra 58,8 cm^{-1}. G6 bandinio atveju (46 paveikslas) juostos ties 1154 cm^{-1} FWHM vertė sumažėja iki 10,6 cm^{-1}. Tai rodo, kad susidaro kristalinė fazė, kurioje yra pirofosfato anijonų [198,209].

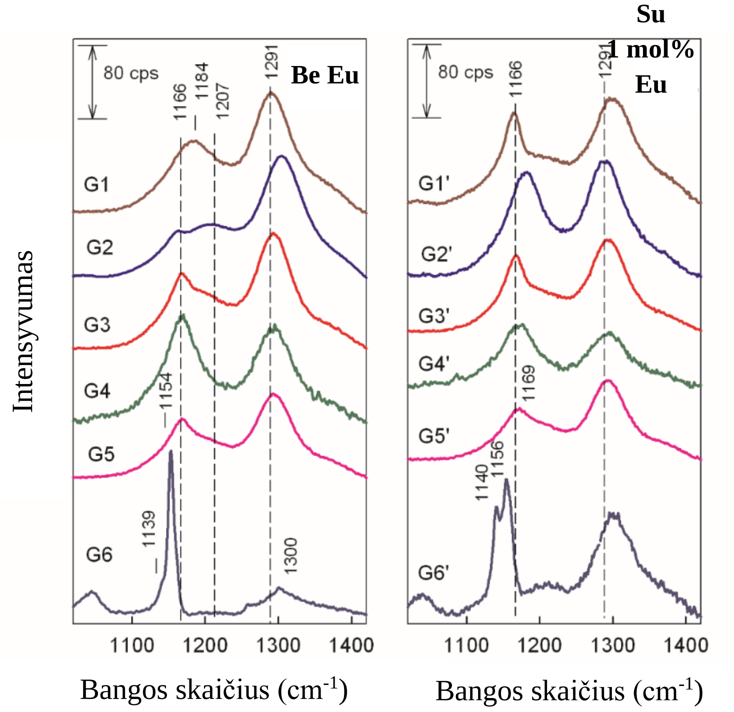

46 paveikslas. Nuo stiklo sudėties priklausantys ramano spinduliuotės spektrai: nelegiruoto stiklo (mėginiai G1−G6) ir legiruoti Eu (mėginiai G1′−G6′). Spektrų fonui pritaikyta polinominės funkcijos korekcija. Sužadinančios bangos ilgis 785 nm (3 mW).

Europio jonais legiruojant skirtingos sudėties fosfatinius stiklus, pastebimi Ramano spektrų skirtumai. Jie palyginti 46 paveikslase. G1´ bandinio atveju aiškiai matomos dvi Eu sukeltos perturbacijos. Pirma ryški νs(P=O) juosta pasislenka 9 cm^{-1} į didesnį bangos skaičių, o tai rodo, kad vidutinis ryšio laipsnis padidėja dėl padidėjusios π ryšio lokalizacijos Q^3 tetraedrinėje vietoje [197]. Antra νs(PO2) juosta pasislenka 21 cm^{-1} link mažesnių bangų skaičiaus, o modos plotis gerokai susiaurėja (FWHM sumažėja nuo 85,0 iki 43,5 cm^{-1}) (46 paveikslas ir Lentelė 11). Dažnio sumažėjimas rodo, kad, esant europio jonams, keičiasi nesurištų PO_2 grupių sąveika su katijonais. Dėl to Q^2 tetraedrinių pozicijų struktūra tampa homogeniškesnė (mažesnis FWHM). Ryšio νs(P=O) dažnio padidėjimas pastebėtas tik G1´ bandinyje. G3´ ir G4´ bandiniuose pastebimų pokyčių nenustatyta. Tuo tarpu G2´ bandinyje vyksta priešingas procesas - νs(P=O) juostos dažnis gerokai sumažėja (15 cm^{-1}). Iš to galima spręsti, kad didėja π ryšio delokalizacija, mažėja P=O ryšio laipsnis ir didėja ryšio ilgis. Be to, gerokai padidėja įtemptos $\nu s(PO_2)$ modos intensyvumas ties 1180 cm^{-1}. Esant europio jonų, susidaro daugiau Q^2 tetraedrinės struktūros pozicijų. G6´ bandinio atveju (46 paveikslas), įvedus europio jonų, labai padidėja ν_s(P=O) juostos, esančios ties 1302 cm^{-1} intensyvumas, susidaro daugiau Q^3 tetraedrinės struktūros pozicijų. Apie kristalinės struktūros fosfatinių pozicijų buvimą šiame bandinyje galima spręsti iš siauros juostos ties 1140 cm^{-1} (FWHM=12,4 cm^{-1}) ir 1156 cm^{-1} (FWHM=16,1). Ši juosta yra susijusi su $\nu_s(PO_2)$ vibracine moda, kurią sudaro Q^2 tetraedrinėse pozicijose esantys nesusiję deguonies atomai.

Vienas iš šio tyrimo tikslų – sukurti naujas žemos temperatūros stiklo sudėtis, galinčias Eu^{3+} jonus integruoti į savo struktūrą. Fotoliuminescencijos spektrai, gauti sužadinant 393 nm bangos ilgio šviesa, atitinka literatūroje aprašytas tendencijas pastebimas Eu^{3+} jonais legiruotose stiklo matricose [214-217]. Kaip matyti iš 47 paveikslaso, fosfatinių stiklų emisijos spektrus sudaro $^5D_0\rightarrow{}^7F_J$ perėjimų smailės: $^5D_0\rightarrow{}^7F_0$, $^5D_0\rightarrow{}^7F_1$, $^5D_0\rightarrow{}^7F_2$, $^5D_0\rightarrow{}^7F_3$ ir $^5D_0\rightarrow{}^7F_4$ perėjimai yra atitinkamai 580-600 nm, 605-629 nm, 646-658 nm ir 680-710 nm intervaluose. Magnetinį dipolinį perėjimą $^5D_0\rightarrow{}^7F_1$ (maksimumas ties 596 nm) leidžia atrankos taisyklės. Priešingai nei elektrinį dipolinį perėjimą $^5D_0\rightarrow{}^7F_2$ (maksimumas ties 616 nm), kurio intensyvumas didėja mažėjant Eu^{3+} vietinės aplinkos simetrijai. Kadangi europis elgiasi panašiai kaip ir mažos simetrijos kristaluose, deformuoto kubo kristalinio lauko centrą užima Eu^{3+} jonai, o kiekvieną iš viršūnių užima deguonis.Dvi iš jų paprastai sudaro briauną, priklausančią tam pačiam fosfatinės grupės tetraedrui. Tai tiesiogiai atsispindi europio ligandų lauke. Čiafosfatinės grupės gali patirti nehomogeniškus įtempimus, atsiradusius dėl to, kaip jos yra sujungtos su stiklo tinklu. Tai savo ruožtu taip pat atsispindi kintančiuose ligandų laukuose, atsirandančiuose dėl skirtingų deguonies ir europio ryšių ilgio. Lyginant skirtingų stiklo sudėčių $^5D_0\rightarrow{}^7F_1$, $^5D_0\rightarrow{}^7F_2$, $^5D^0\rightarrow{}^7F_4$ perėjimų emisijos intensyvumą, kai legiruojančios medžiagos koncentracija yra pastovi (1 % Eu), G1 stiklo sudėties emisijos intensyvumas yra daugiau nei du kartus didesnis nei mažiausio intensyvumo (G6) (47 paveikslas).

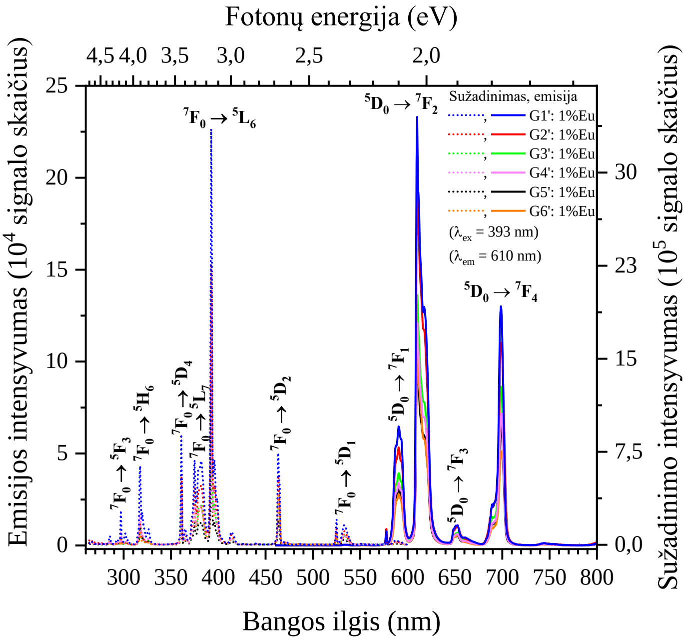

47 paveikslas. Emisijos ir sužadinimo intensyvumo palyginimas, kai skrtinga stiklo sudėtis, tačiau legiruojančio jono kiekis išlieka pastovus.

Taip pat buvo tiriama ir europio kiekio įtaka liuminescencijos savybėms. Šiuo tikslu į stiklų pirmtakų seriją atskirai buvo dedama 0,2 %, 0,6 % arba 1 % Eu^{3+} (mol- %). Kaip galima matyti 48 paveiksle, stiklo mėginių spalva vizualiai skyrėsi (keitėsi nuo rožinės iki oranžinės). Išsamūs liuminescencijos rezultatai pateikti 49 paveikslase. Kaip galima tikėtis, didėjant Eu kiekiui stikluose, didėja ir emisijos intensyvumas (λ_{ex} = 395 nm). Pavyzdžiui, liuminescencijos intensyvumas esant 610 nm bangos ilgiui, pereinant nuo 0,2 % prie 0,6 %, o vėliau - prie 1 % Eu, G1 sudėties stikle padidėja atitinkamai 2,0 ir 2,8 karto.

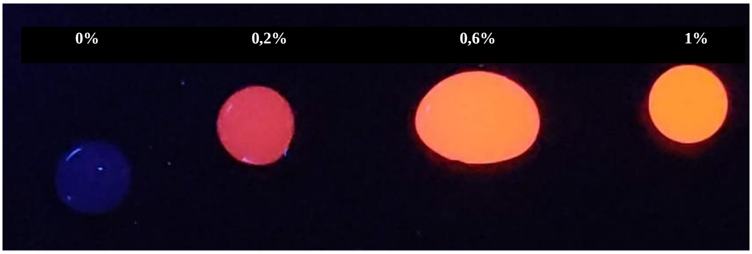

48 paveikslas. G1 sudėties stiklo optinis vaizdas, kuriame matyti europio koncentracijos įtaka spalvai liuminescencijai (λ_{ex} = 395 nm).

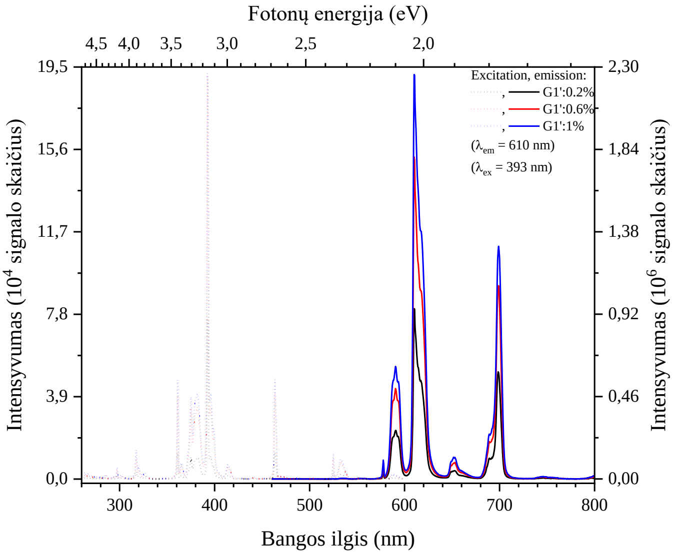

49 paveikslas. G1 sudėties stiklo fotoliuminescencijos emisijos ir sužadinimo spektrai.

Literatūroje nurodoma, kad europio emisijos santykis $^5D_0 \rightarrow {}^7F_2/{}^5D_0 \rightarrow {}^7F_1$ didelės simetrijos aplinkoje yra mažesnis arba lygus vienetui, ir atvirkščiai, kuo santykis didesnis, tuo mažesnės simetrijos pozicijose yra europis [218]. Bandinių sudėties skirtumai lemia koordinacinio skaičiaus, ligandų atstumų ir ryšių kampų skirtumus. Šie skirtumai taip pat turi įtakos ligandų lauko stiprumui, todėl skiriasi jonų energijos lygiai. Lyginant santykinius intensyvumus $^5D_0 \rightarrow {}^7F_2/{}^5D_0 \rightarrow {}^7F_1$ (Lentelė 12) visos vertės patenka į 3-4 intervalą. Tai rodo mažą europio aplinkos simetriškumą, kuris atitinka literatūroje [214,218] pateiktas vertes.

Lentelė 12. Santykiniai emisijos linijų intensyvumai

Eu	Sudėtis					
mol%	G1’	G2’	G3’	G4’	G5’	G6’
0,2	3,60	3,51	3,41	3,48	3,33	3,87
0,6	3,58	3,56	3,44	3,52	3,39	3,93
1	3,60	3,59	3,46	3,54	3,33	3,79

Tam tikrais atvejais (pvz., taikymui lazeriuose, apšvietimui, kai reikalingas specifinis spalvos grynumas ir t. t.) visų kitų emisijos bangos ilgių, išskyrus 610 nm, sumažinimas gali būti naudingas [216,219]. Apskaičiuoti $^5D_0 \rightarrow ^7F_2$ emisijos linijos (605 nm – 630 nm) integralinio intensyvumo santykiai procentais, palyginti su emisijos intensyvumu 520 nm - 750 nm intervale (Lentelė 13). Pastebėtina, kad visais atvejais santykio vertė yra didesnė nei 50 % ir kinta nežymiai, o tai rodo, kad perėjimas $^5D_0 \rightarrow ^7F_2$ yra dominuojantis, nepriklausomai nuo tetraedrinių fosfatinių vietų stikluose.

Lentelė 13. $^5D_0 \rightarrow ^7F_2$ emisijos linijos santykinis integralinis intensyvumas, išreikštas procentais

Eu	Sudėtis					
mol%	G1’	G2’	G3’	G4’	G5’	G6’
0.2	53,0	51,4	50,9	52,8	50,3	53,0
0.6	53,7	52,4	51,7	52,4	51,9	54,2
1	54,2	53,5	52,2	53,6	51,4	55,2

Elementų pasiskirstymo bandinių paviršiuje morfologijos ir homogeniškumo analizė parodė, kad tiriami elementai yra homogeniškai pasklidę visame stiklo bandinio paviršiuje. Aiškiai matomi grioveliai stiklo paviršiuje atsirado dėl šlifavimo procedūros. SEM vaizdų ir EDX žemėlapių, kuriuose matomi atrinkti elementai, rezultatai pateikti 50 paveikslase. Skirtingi pilkos spalvos atspalviai pasirinktų elementų vaizduose rodo jų santykinį kiekį stiklo paviršiuje.

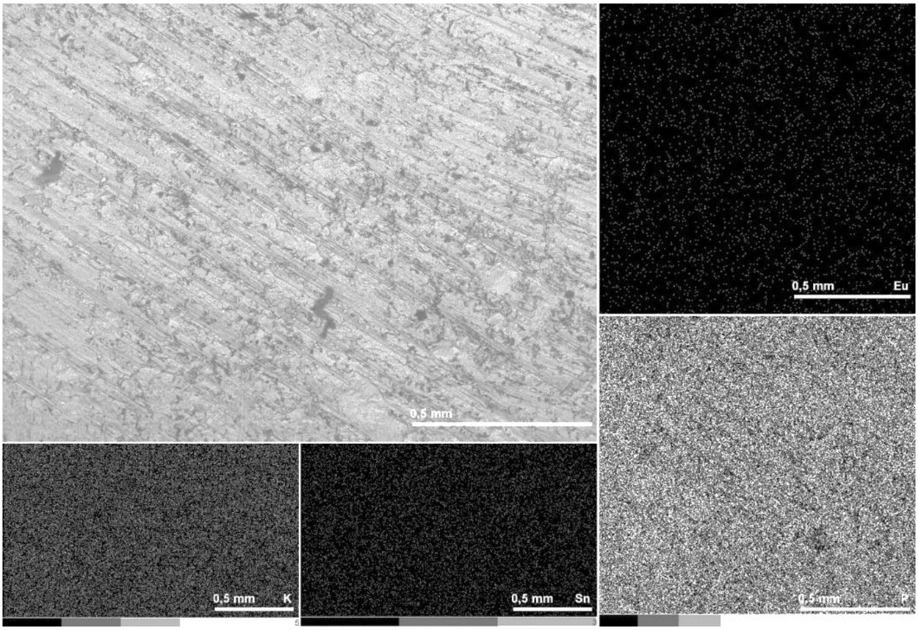

50 paveikslas. SEM nuotraukos ir EDX žemėlapiai atrinktiems elementams G1: 1% Eu sudėties stikle.

Nagrinėjant $Y_{3-x}La_xFe_5O_{12}$ granatą, literatūroje pateikiamos įvairios legiravimo ribos, pavyzdžiui, x = 0,45 [220], x = 0,75 [45] ar net x = 0,8 [221], kurios atitinka šioje disertacijoje aptariamus rezultatus. Rentgeno spinduliuotės difrakcijos (XRD) paveikslai lantanu pakeistuose itrio geležies granatuose $Y_{3-x}La_xFe_5O_{12}$ pavaizduoti 51 paveikslase. Kaip matyti, kai itrio molinis pakeitimas lantanu yra 25%, galima nustatyti tik nedidelio intensyvumo difrakcinę smailę, priskiriamą perovskitui $LaFeO_3$. Didėjant La pakaitiniam kiekiui, didėja ir perovskitinės fazės kiekis, todėl mažėja santykinė granato fazės dalis. Akivaizdu, kad, pasiekus visišką itrio pakeitimą, XRD paveiksle negalima aptikti jokios granato fazės. Šiuo atveju zolių-gelių sintezės metodika susidaro tik $LaFeO_3$ ir Fe_2O_3.

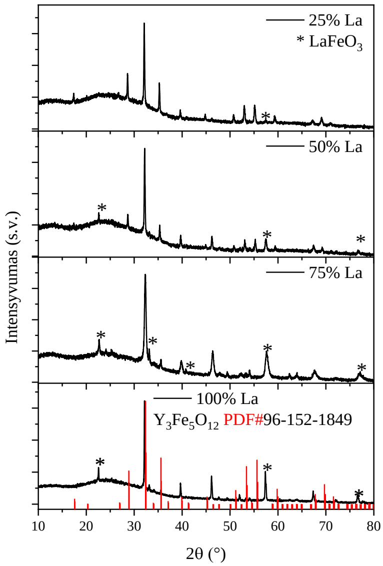

51 paveikslas. $Y_{3-x}La_xFe_5O_{12}$ bandinių su skirtingu lantano kiekiu rentgeno spinduliuotės difraktoramos. Vertikaliomis linijomis pavaizduota standartinė YIG XRD difraktograma.

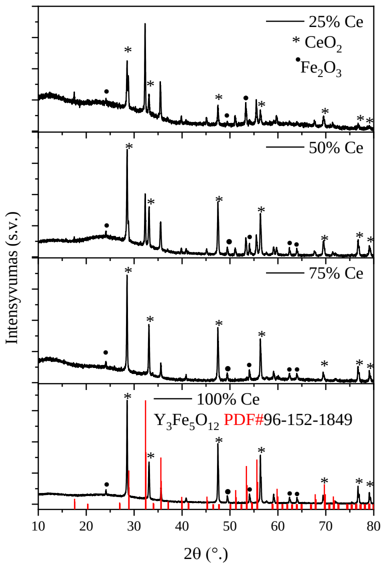

52 paveikslas. $Y_{3-x}Ce_xFe_5O_{12}$ bandinių su skirtingu cerio kiekiu miltelių rentgeno spinduliuotės difraktogramos. Vertikaliomis linijomis pavaizduota standartinė YIG XRD difraktograma.

$Y_{3-x}Ce_xFe_5O_{12}$ atveju (žr. 52 paveikslasą) vienfazio granato formavimasis vyksta ne visame pakeičiamumo intervale. Mėginiuose, kurių x = 0,25, galima nustatyti tik nedidelį granato fazės kiekį. Oksidai, tokie kaip CeO_2 ir Fe_2O_3, yra pagrindinės kristalinės fazės, nustatytos visuose susintetintuose bandiniuose.

Pr ir Nd pakeistų granatų ($Y_{3-x}Pr_xFe_5O_{12}$ ir $Y_{3-x}Nd_xFe_5O_{12}$) XRD paveikslai pateikti atitinkamai 53 paveikslase ir 54 paveikslase. Šiais atvejais gauti rezultatai yra labai panašūs. Kaip matyti, net ir mišrių metalų granatai $Y_{1,5}Pr_{1,5}Fe_5O_{12}$ ir $Y_{1,5}Nd_{1,5}Fe_5O_{12}$ yra vienfaziai junginiai. Tačiau nereikšmingas perovskito fazės kiekis susidaro tuo atveju, kai 75 % itrio pakeičiama prazeodimiu. Neodimio atveju, sintezės produktas su tokiu pačiu pakeitimo lygiu vis dar yra vienfazis granato junginys.

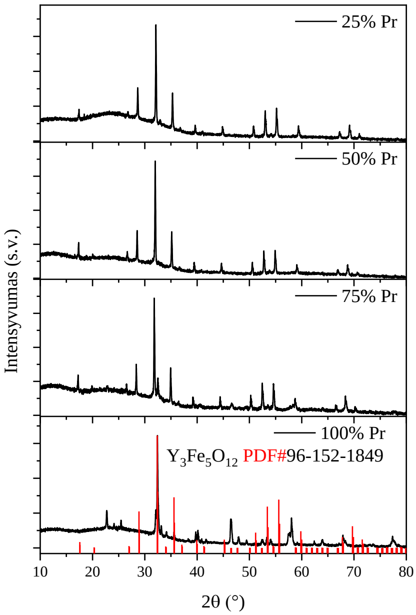

53 paveikslas. $Y_{3-x}Pr_xFe_5O_{12}$ bandinių su skirtingu praseodimo kiekiu miltelių rentgeno spinduliuotės difraktogramos. Vertikalios linijomis pavaizduota standartinė YIG XRD difraktograma.

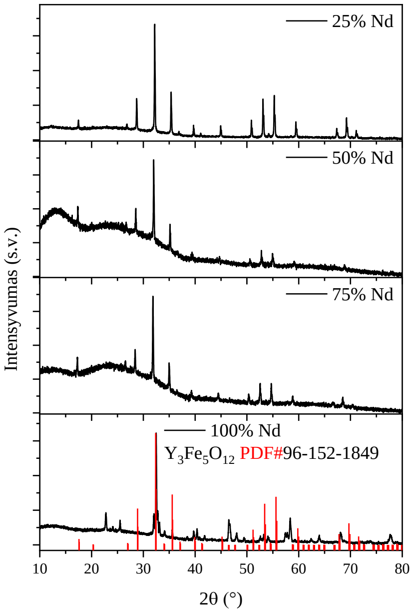

54 paveikslas.$Y_{3-x}Nd_xFe_5O_{12}$ bandinių su skirtingu neodimio kiekiu miltelių rentgeno spindulių difraktogramos. Vertikalios linijos pavaizduota standartinė YIG XRD difraktograma.

Įvairias medžiagas galima identifikuoti pagal jų IR spektrus, interpretuotinus kaip „pirštų atspaudus“ [222]. Zolių-gelių metodu gautų $Y_{3-x}Ln_xFe_5O_{12}$ bandinių FTIR spektrai 850-400 cm^{-1} srityje pavaizduoti 55–58 paveiksluose. FTIR spektroskopijos rezultatai gerai sutampa su XRD rezultatais. Pavyzdžiui, $Y_{3-x}La_xFe_5O_{12}$ bandinių su mažesniu pakaitiniu La kiekiu (25 % ir 50 %) FTIR spektruose (55 paveikslas) yra absorbcijos juostų, priskiriamų M-O valentiniams virpesiams 645-644 cm^{-1}, 580-579 cm^{-1} ir 549-548 cm^{-1}. Kaip skelbiama mokslinėje literatūroje, granatų FTIR spektruose paprastai būna kelios intensyvios smailės 1000-400 cm^{-1} intervale. Šios juostos būdingos granatų struktūros junginiams ir yra priskiriamos granato struktūroje esančių tetraedrinių struktūrinių vienetų valentiniams virpesiams.

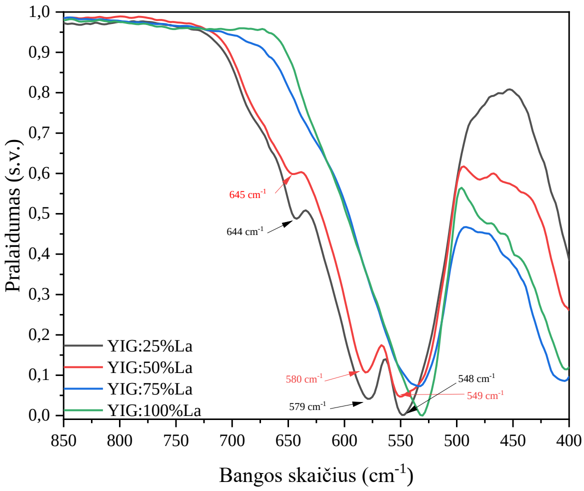

55 paveikslas. $Y_{3-x}La_xFe_5O_{12}$ bandinių su skirtingu lantano kiekiu FTIR spektrai.

Didėjant lantano kiekiui plati sugerties juosta šioje srityje nebeskyla į kelias siauras. Tokie ruožų dažniai būdingi perovskito ortorhombinėms ir kubinėms valentinių virpesių modoms. Šie FTIR spektroskopijos rezultatai aiškiai patvirtina, kad esant aukštesniam La pakeitimo lygiui, vietoj granato susidaro perovskito kristalinė fazė.

Labai panašus FTIR spektras 850-500 cm^{-1} srityje gautas $Y_{3-x}Ce_xFe_5O_{12}$ bandiniui, kai 25 % itrio buvo pakeista ceriu (56 paveikslas). Stebima papildoma plati juosta ties 471 cm^{-1}, kuri gali būti priskirta M-O virpesiams atskiruose oksiduose. Pavyzdžiui, CeO_2 arba Fe_2O_3. $Y_{3-x}Ce_xFe_5O_{12}$ bandinių FTIR spektrų prigimtis palaipsniui kinta didėjant Ce kiekiui bandinyje. Plati sugerties juosta 645-548 cm^{-1} srityje neišsiskaido, o šios sugerties juostos maksimumas pasislenka į žemesnių bangų sritį, lyginant su $Y_{3-x}La_xFe_5O_{12}$ mėginiais, kuriuose yra didesnis pakaitinis La kiekis (75 % ir 100%). Be to, papildomos absorbcijos juostos, aptinkamos ties 430 cm^{-1}, patvirtina XRD rezultatus, susijusius su pavienių CeO_2 arba Fe_2O_3 oksidų susidarymu sintetinant šiuos mėginius.

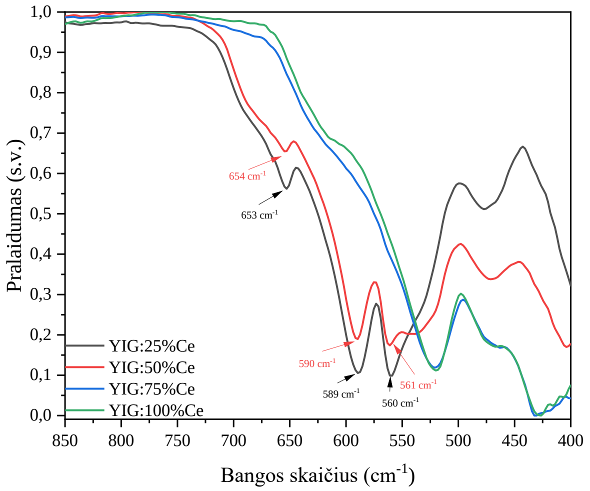

56 paveikslas. $Y_{3-x}Ce_xFe_5O_{12}$ bandinių su skirtingu cerio pakaitiniu lygiu FTIR spektrai.

$Y_{3-x}Pr_xFe_5O_{12}$ ir $Y_{3-x}Nd_xFe_5O_{12}$ granatų FTIR spektrai pateikti atitinkamai 57 paveikslase ir 58 paveikslase. Čia vėl matoma, kad FTIR rezultatai panašiai koreliuoja su rezultatais, gautais naudojant XRD analizę. Granato, kaip pagrindinės kristalinės fazės, susidarymą galima aiškiai patvirtinti esant 0-75% Pr ir Nd pakeitimui. Perovskito fazės pradeda vyrauti, kai itris visiškai pakeičiamas prazeodimiu arba neodimiu. Galima daryti išvadą, kad FTIR spektroskopija yra nepakeičiama priemonė reakcijos produktams apibūdinti, sintetinant granato kristalinės struktūros junginius.

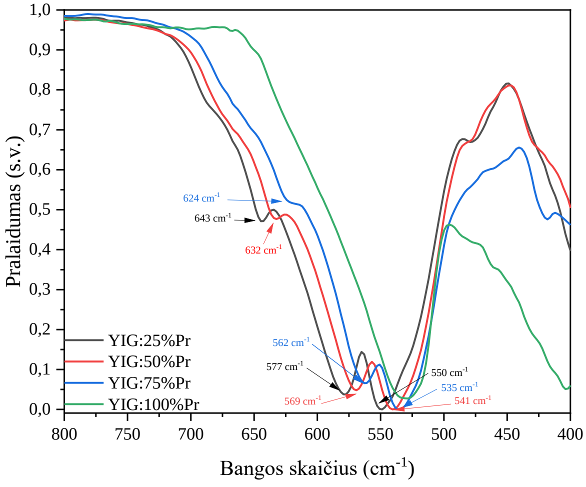

57 paveikslas. $Y_{3-x}Pr_xFe_5O_{12}$ bandinių su skirtingu prazeodimio pakaitiniu lygiu FTIR spektrai.

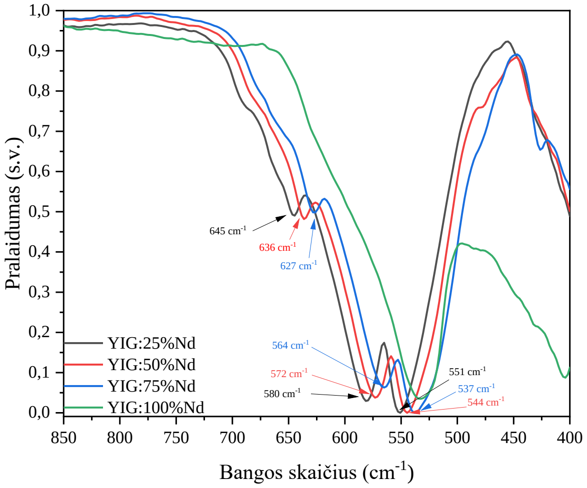

58 paveikslas. $Y_{3-x}Nd_xFe_5O_{12}$ bandinių su skirtingu neodimio pakaitiniu lygiu FTIR spektrai.

Rentgeno spindulių difrakcinės analizės rezultatai pateikti 59 paveikslase. Buvo gauti grynos granato struktūros junginiai. Kadangi kiekviena smailė gali būti priskiriama YAG (PDF#01-073-3185), kubinės kristalinės gardelės I a -3 d erdvinės grupės granato struktūrai. Bendrai granato struktūrą galima užrašyti taip: $A_3B_2C_3O_{12}$, kur A koordinacinis skaičius yra 8, B – 6, o C – 4. Kaip žinoma, struktūroje esama trijų tipų koordinacinių geometrijų: dodekaedrinių, oktaedrinių ir tetraedrinių. Cr^{3+} jonų spindulys yra panašus į Al heksagoninės arba oktaedrinės koordinacijos spindulį (0,535 angstremo Al^{3+} ir 0,615 angstremo Cr^{3+}). Iš to galima daryti prielaidą, kad Cr^{3+} jonai gali pakeisti Al^{3+} jonus struktūroje [226]. Turint omenyje, kad į granato struktūrą buvo įterptas tik nedidelis ppm chromo kiekis, nėra aiškių smailių poslinkių, kurie turėtų matytis pagal Braggo dėsnį:

$$n\lambda = 2dsin\theta \tag{28}$$

ir Vegardo dėsnį (jei mažesni jonai pakeičiami didesniais, tarpplokštuminis atstumas padidėja, todėl smailė pasislenka į mažesnių 2θ intervalą), jeigu būtų ženklesni struktūriniai pakitimai. Difraktogramose nėra jokių papildomų priemaišinių struktūrų smailių net ir tada, kai chromo molinė dalis tyrimo sąlygomis yra didžiausia junginyje. Tai leidžia manyti, kad chromas buvo sėkmingai įterptas į granato struktūrinę matricą. Reikia pastebėti, kad taip pat buvo atliktas Rietveldo patikslinimas. Tiesa, dėl nedidelių chromo kiekių, siekiant nustatyti ir paaiškinti struktūrinių efektų skirtumus, reikėtų naudoti sinchrotroninę spinduliuotę ar neutronų difrakciją.

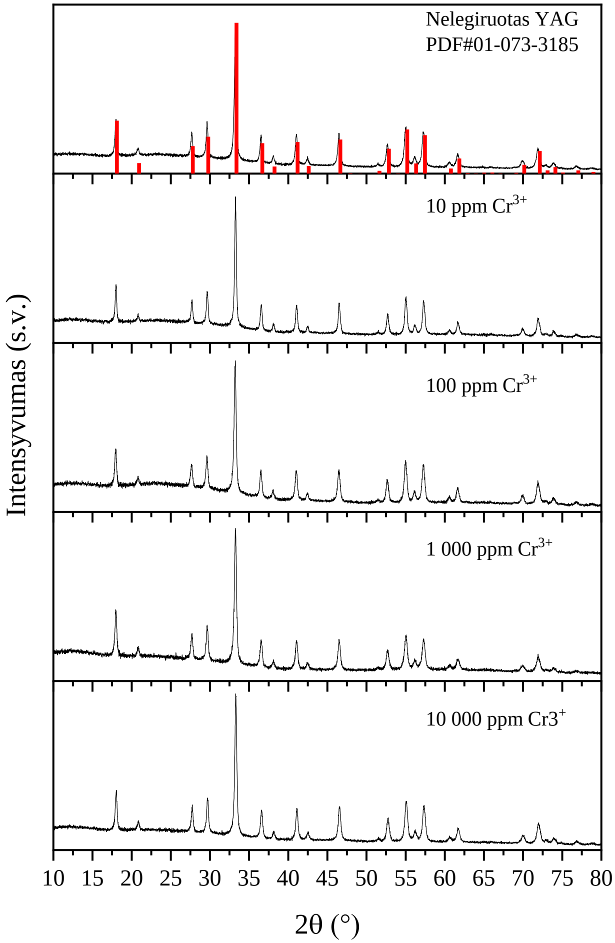

59 paveikslas. Gryno ir legiruotų bandinių rentgeno spinduliuotės difraktogramos.

Visi bandiniai taip pat buvo apibūdinti FTIR spektroskopijos analize. Visų legiruotų ir nelegiruotų bandinių FTIR spektruose matomos ryškios absorbcijos smailės ties 449, 508, 565 cm^{-1} (60 paveikslas). Jos priklauso tetraedrinių koordinuotų vietų valentiniams virpesiams. Kitas virpesių rinkinys ties 685, 718, 785 cm^{-1} (60 paveikslas) yra susijęs su asimetriniais AlO_4 tetraedrų valentiniais virpesiais. Šie įprastai stebimi tik granato struktūros medžiagose [227]. Taip pat reikėtų pažymėti, kad nė viename iš bandinių negalima pastebėti jokių smailų, kurias būtų galima priskirti OH grupės virpesiams, gesinantiems liuminescenciją.

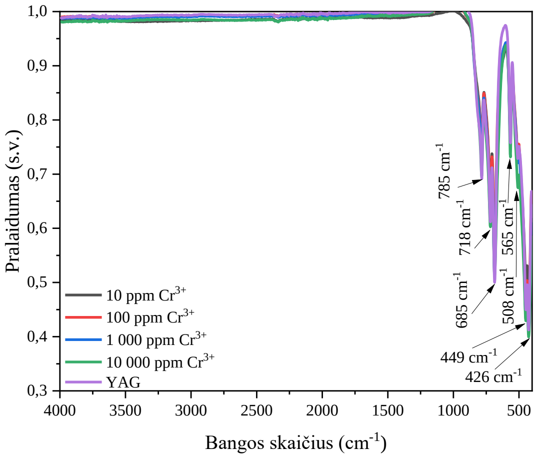

60 paveikslas. Gryno ir legiruoto granato bandinių FTIR spektras.

Cr^{3+} jonų optinės savybės tiesiogiai priklauso nuo legiruojamosios gardelės kristalinio lauko aplinkos stiprio, todėl esant silpnam kristaliniam laukui Cr^{3+} rodo plačiajuostę emisijos liniją [228]. Plačiajuostė sukiniui leidžiamo perėjimo $^4T_2 \rightarrow ^4A_2$ spinduliuotė atsiranda 650-1600 nm intervale, o siauros spinduliuotės linijos apie 700 nm atsiranda dėl sukinio draudžiamo perėjimo $^2E \rightarrow ^4A_2$ [229]. Apibendrinant galima teigti, kad jei Cr^{3+} jonas yra stipriame kristaliniame lauke, ^2E lygmens energija yra mažesnė už $^4T_2$ ir liuminescencijos spektruose matomos aštrios linijos. Ir atvirkščiai, esant silpnesniam kristaliniam laukui ($^2E \rightarrow ^4T_2$) galima stebėti tik plačią $^4T_2$ emisiją [229].

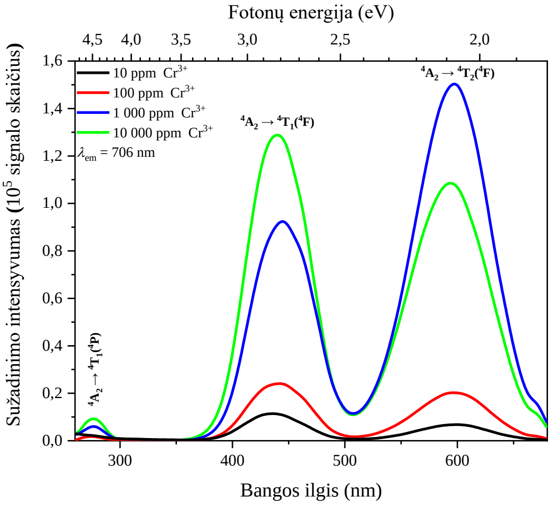

61 paveikslas. Bandinių, legiruotų Cr^{3+}, fotoliuminescencijos sužadinimo spektrai esant 706 nm bangos ilgio spinduliuotei.

Legiruotų bandinių sužadinimo spektrus (61 paveikslas) sudaro trys pagrindinės viršūnės, esančios ties 275, 440 ir 580 nm bangos ilgiu. Jos priskiriamos 3d vidiniams perėjimams, t. y. atitinkamai ${}^4A_2 \rightarrow {}^4T_1(4P)$, ${}^4A_2 \rightarrow {}^4T_1(4F)$, ${}^4A_2 \rightarrow {}^4T_2(4F)$. Galima pastebėti, kad didėjant legiruojančios medžiagos kiekiui didėja sužadinimo absorbcija. Tačiau 10 000 ppm mėginio ${}^4A_2 \rightarrow {}^4T_2(4F)$ smailės intensyvumas yra mažesnis nei 1 000 ppm mėginio, o tai rodo, kad skirtinguose mėginiuose yra skirtingos struktūrinės pozicijos. Cr^{3+} jonai yra arba žemo lauko pozicijose, arba aukšto (arba galbūt - vidutinio) lauko pozicijose. Tai atsispindi ir fotoliuminescencijos spektruose, pateiktuose 62 bei 63 paveiksluose. Nepriklausomai nuo to, ar bandiniai sužadinti esant 580 nm, ar 440 nm bangos ilgiui, siauros emisijos linijos gali būti siejamos su ${}^2E \rightarrow {}^4A_2$ sukinio draudžiamu perėjimu. Kaip galima tikėtis, sužadinus 440 nm bangos ilgiu, emisijos spektrai rodo tipišką liuminescencijos intensyvumo didėjimo tendenciją didėjant Cr^{3+} koncentracijai bandiniuose (64 paveikslas). Tuo tarpu bandinys, kuriame yra 1000 ppm Cr^{3+}, intensyviausiai spinduliuoja sužadinus 580 nm bangos ilgiu. Skirtingas Cr^{3+} jonų energijos lygmenų skilimas oktaedrinėje padėtyje patvirtina papildomą emisijos matavimą esant 275 nm bangos ilgiui.

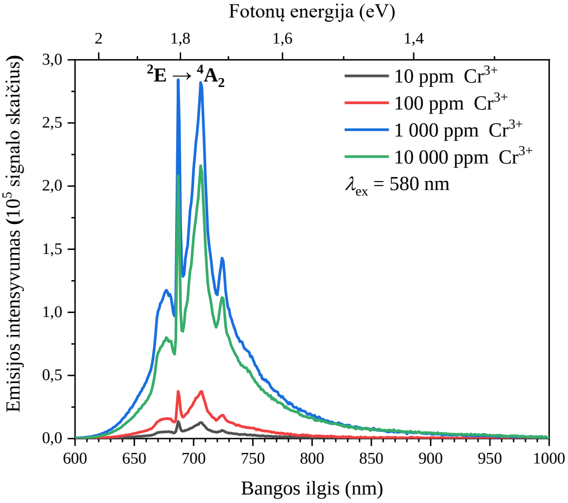

62 paveikslas. Bandinių, legiruotų Cr^{3+}, fotoliuminescencinės emisijos spektrai, kai sužadinimo bangos ilgis 580 nm.

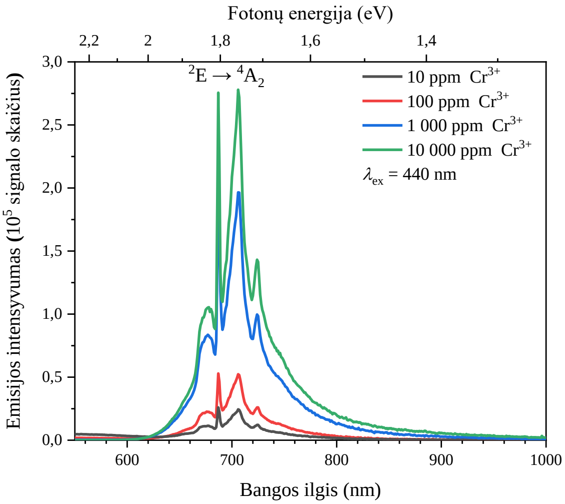

63 paveikslas. Bandinių, legiruotų Cr^{3+}, fotoliuminescencinės emisijos spektrai, esant 440 nm sužadinimui.

Jei bandiniai sužadinami 275 nm šviesa, YAG:Cr spinduliuoja plačią artimojo infraraudonojo spektro juostą (64 paveikslas). Šios juostos maksimumas yra apie 800 nm (FWHM 100 nm) ir ji yra priskiriama sukiniui leidžiamam $^4T_2 \rightarrow {}^4A_2$ perėjimui. Kaip matyti, specifinis spinduliavimas (64 paveikslaso intarpas) beveik eksponentiškai mažėja didėjant legiruojančio jono kiekiui ir beveik išnyksta, kai chromo kiekis pasiekia 10 000 ppm. Be to, jei chromo koncentracija yra 1 000 ppm ar didesnė, aiškus $^2E \rightarrow {}^4A_2$ perėjimo įrodymas pastebimas net ir esant 275 nm sužadinimui. Tai rodo nedidelį skirtingų bandinių Cr^{3+} jonų ^2E ir $^4T^2(4F)$ energijos lygmenų pokytį.

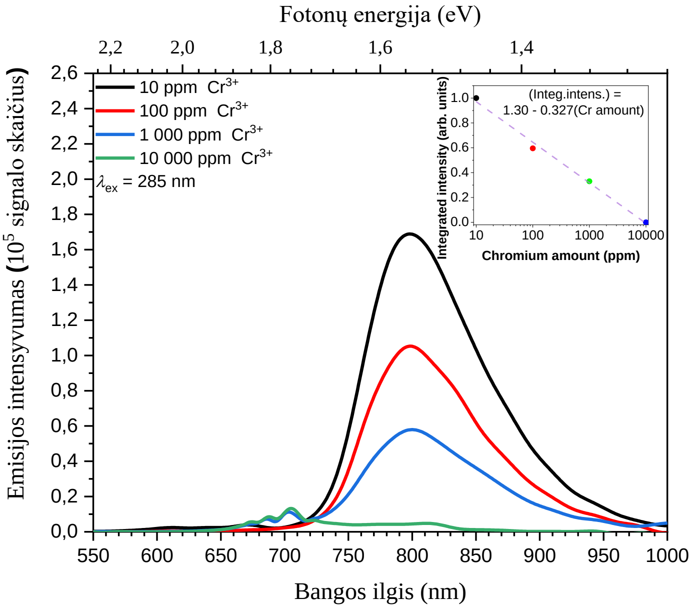

64 paveikslas. Bandinių, legiruotų Cr^{3+}, fotoliuminescencijos emisijos spektrai esant 275 nm bangos ilgio sužadinimui. Intarpe parodytas eksponentinis emisijos intensyvumo mažėjimas didėjant koncentracijai.

Nuo koncentracijos priklausomi $^4T_2 \rightarrow {}^4A_2$ Cr^{3+} jonų perėjimai itrio aliuminio granate aptarti pirmą kartą. Skirtingų Cr^{3+} jonų perėjimų pobūdis aptariamas analizuojant kitus junginius tiriančius darbus. Šį stebėjimą galima interpretuoti atsižvelgiant į tai, kad dalis Cr^{3+} jonų gali būti labai netvarkingoje aplinkoje, pavyzdžiui, amorfinėje ar stipriai defektinėje būsenoje. Tai kambario temperatūroje sukeltų didelį emisijos energijų poslinkį [230]. Kita priežastis gali būti siejama su Cr^{3+} - Cr^{3+} jonų porų emisija. Jos egzistavimas kaip atskiras reiškinys, o ne tik energijos perdavimo mechanizmas, neseniai užfiksuotas magnetoplumbito $Al_{11,88-x}Ga_xO_{19}$:0,12Cr^{3+} medžiagoje [231]. Šiuo atveju labai tikėtina, kad pasikeitus legiruojančio jono koncentracijai, pasikeičia vietinė kristalo aplinka(Al^{3+} ir Cr^{3+} elektroneigiamumo skirtumai [232,233] yra atitinkamai 1,513 ir 1,587). Tanabės-Sugano diagrama rodo, kad Cr^{3+} energijos lygmenys tirtuose bandiniuose svyruoja apie brūkšninę liniją, pavaizduotą 65 paveiksle. Jei chromo koncentracija yra mažesnė nei 1000 ppm, bandiniuose stebima emisija, kurią sukelia I tipui (žemas kristalinis laukas) priskiriamas legiruojančių jonų energijos lygmenų skilimas. Tuo tarpu jei chromo jonų koncentracija yra apie 1000 ppm ir daugiau, vyrauja II tipui (aukštas kristalinis laukas) priskiriamas energijos lygmenų skilimas. Reikėtų atkreipti dėmesį, kad aliuminio pakeitimas chromo jonais turėtų šiek tiek sumažinti vietinės aplinkos kristalinį lauką, todėl sukeliami Cr^{3+} jonų perėjimai $^4T_2 \rightarrow {}^4A_2$.

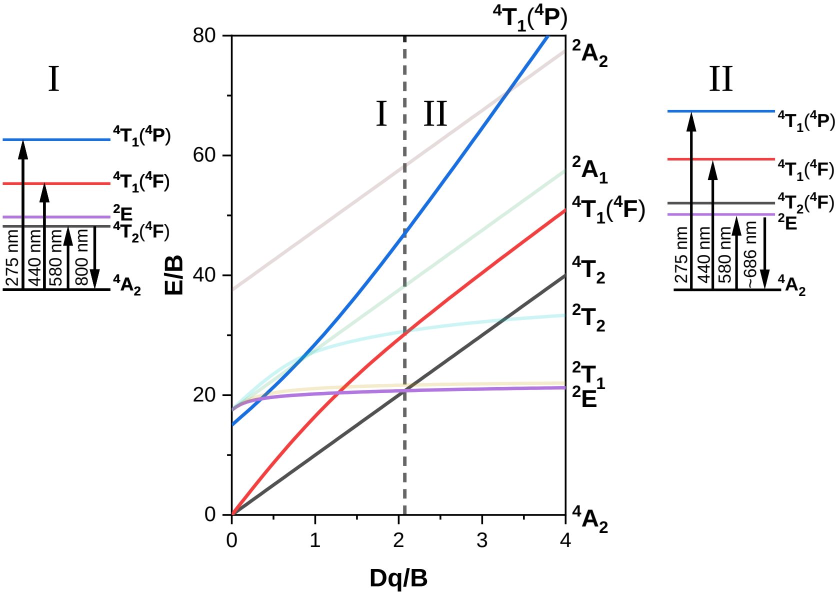

65 paveikslas. Chromu legiruotų granatųTanabe-Sugano ir energijos lygių diagramos.

IŠVADOS

1. Visi bandinių stiklai legiruoti 0,2 mol-%, 0,6 mol-% ir 1,0 mol-% Eu^{3+}. Nustatyta, kad Eu^{3+} jonai buvo išsidėstę žemos simetrijos aplinkoje, todėl vyravo $^5D_0 \rightarrow {}^7F_2$ perėjimų emisija. Nepriklausomai nuo tetraedrinių fosfatinių vietų tipo stikluose (Q^0, Q^1, Q^3 arba Q^4), palyginti su visais emisijos spektrais, minėtasis perėjimas sudarė daugiau kaip 50 % emisijos intensyvumo.

2. Kaip pastebima, 50 P_2O_5 : 15 K_2O : 10 Li_2O : 10 CaO : 2 Al_2O_3 : 10 ZnO : 2 B_2O_3 : 1 SnO (G1) sudėtis pasižymi didžiausiu fotoliuminescencijos intensyvumu su visomis minėtomis legiruojančių jonu koncentracijomis.

3. Atliktas tyrimas rodo, kad pakeitimo lygis zolių-gelių būdu gautose $Y_{3-x}Ln_xFe_5O_{12}$ sistemose priklauso nuo lantanoido elemento prigimties. Sėkmingai susintetinti vienfaziai granatai su tam tikrais lantanoidų pakaitais (Pr ir Nd).

4. Buvo įrodyta, kad itrio aliuminio granato matricoje, keičiant legiruojančios medžiagos koncentraciją ir sužadinimo bangos ilgį, galima pasiekti du skirtingus chromo emisijos tipus. Vieno tipo spinduliuotė, kuriai draudžiama sukinio momento emisija, intensyvumas didėja didėjant liuminescencinių centrų koncentracijai. Kitas emisijos tipas, kuris yra plačiajuostis ir pasižymi eksponentiniu intensyvumo mažėjimu didėjant chromo jonų koncentracijai, žymimas kaip $^4T_2 \rightarrow {}^4A_2$. Pagal emisijos spektrus galima nustatyti YAG priemaišinio chromo kiekį, nes emisija yra labai jautri chromo jonų koncentracijai.

BIBLIOGRAPHY

[1] S. Damodaraiah, V. Reddy Prasad, R.P. Vijaya Lakshmi, Y.C. Ratnakaram, Luminescence behaviour and phonon sideband analysis of europium doped Bi2O3 based phosphate glasses for red emitting device applications, Optical Materials 92 (2019) 352–358. https://doi.org/10.1016/j.optmat.2019.04.060.

[2] D. Shajan, P. Murugasen, S. Sagadevan, Studies on structural, optical and spectral properties of Europium oxide doped phosphate glasses, Optik 136 (2017) 165–171. https://doi.org/10.1016/j.ijleo.2017.02.013.

[3] C. Nico, R. Fernandes, M.P.F. Graça, M. Elisa, B.A. Sava, R.C.C. Monteiro, L. Rino, T. Monteiro, Eu3+ luminescence in aluminophosphate glasses, Journal of Luminescence 145 (2014) 582–587. https://doi.org/10.1016/j.jlumin.2013.08.041.

[4] M. Elisa, B.A. Sava, I.C. Vasiliu, R.C.C. Monteiro, J.P. Veiga, L. Ghervase, I. Feraru, R. Iordanescu, Optical and structural characterization of samarium and europium-doped phosphate glasses, Journal of Non-Crystalline Solids 369 (2013) 55–60. https://doi.org/10.1016/j.jnoncrysol.2013.03.024.

[5] H. Ebendorff-Heidepriem, D. Ehrt, Formation and UV absorption of cerium, europium and terbium ions in different valencies in glasses, Optical Materials 15 (2000) 7–25. https://doi.org/10.1016/S0925-3467(00)00018-5.

[6] A. Herrmann, S. Fibikar, D. Ehrt, Time-resolved fluorescence measurements on Eu3+- and Eu2+-doped glasses, Journal of Non-Crystalline Solids 355 (2009) 2093–2101. https://doi.org/10.1016/j.jnoncrysol.2009.06.033.

[7] R.T. Karunakaran, K. Marimuthu, S. Surendra Babu, S. Arumugam, Structural, optical and thermal studies of Eu^{3+} ions in lithium fluoroborate glasses, Solid State Sciences 11 (2009) 1882–1889. https://doi.org/10.1016/j.solidstatesciences.2009.08.001.

[8] B. Aktas, M. Albaskara, S. Yalcin, K. Dogru, Optical Properties of Soda-Lime-Silica Glasses Doped with Eggshell Powder, Acta Phys. Pol. A 132 (2017) 442–444. https://doi.org/10.12693/APhysPolA.132.442.

[9] S. Yalcin, B. Aktas, D. Yilmaz, Radiation shielding properties of Cerium oxide and Erbium oxide doped obsidian glass, Radiation Physics and Chemistry 160 (2019) 83–88. https://doi.org/10.1016/j.radphyschem.2019.03.024.

[10] D. Yılmaz, B. Aktaş, Ş. Yalçın, M. Albaşkara, Erbium oxide and Cerium oxide-doped borosilicate glasses as radiation shielding material, Radiation Effects and Defects in Solids 175 (2020) 458–471. https://doi.org/10.1080/10420150.2019.1674301.

[11] B. Aktas, S. Yalcin, K. Dogru, Z. Uzunoglu, D. Yilmaz, Structural and radiation shielding properties of chromium oxide doped borosilicate

glass, Radiation Physics and Chemistry 156 (2019) 144–149. https://doi.org/10.1016/j.radphyschem.2018.11.012.

[12] R.T. Karunakaran, K. Marimuthu, S. Surendra Babu, S. Arumugam, Structural, optical and thermal studies of Eu^{3+} ions in lithium fluoroborate glasses, Solid State Sciences 11 (2009) 1882–1889. https://doi.org/10.1016/j.solidstatesciences.2009.08.001.

[13] A. Herrmann, S. Fibikar, D. Ehrt, Time-resolved fluorescence measurements on Eu^{3+}- and Eu^{2+}-doped glasses, Journal of Non-Crystalline Solids 355 (2009) 2093–2101. https://doi.org/10.1016/j.jnoncrysol.2009.06.033.

[14] X. Jiang, Z. Li, H. Zhuang, D. Tang, K. Chen, T. Zhang, Stable phosphate-based glass for low-temperature sealing applications: Effect of Si_3N_4 dopant, Ceramics International 44 (2018) 20227–20231. https://doi.org/10.1016/j.ceramint.2018.08.007.

[15] N. Chanthima, Y. Tariwong, H.J. Kim, J. Kaewkhao, N. Sangwaranatee, Effect of Eu^{3+} Ions on the Physical, Optical and Luminescence Properties of Aluminium Phosphate Glasses, Key Engineering Materials 766 (2018) 122–126. https://doi.org/10.4028/www.scientific.net/KEM.766.122.

[16] M. Sołtys, J. Janek, L. Żur, J. Pisarska, W.A. Pisarski, Compositional-dependent europium-doped lead phosphate glasses and their spectroscopic properties, Optical Materials 40 (2015) 91–96. https://doi.org/10.1016/j.optmat.2014.11.052.

[17] T.Y. Wei, Y. Hu, L.G. Hwa, Structure and elastic properties of low-temperature sealing phosphate glasses, Journal of Non-Crystalline Solids 288 (2001) 140–147. https://doi.org/10.1016/S0022-3093(01)00612-3.

[18] A. Ikesue, Y.L. Aung, T. Yoda, S. Nakayama, T. Kamimura, Fabrication and laser performance of polycrystal and single crystal Nd:YAG by advanced ceramic processing, Optical Materials 29 (2007) 1289–1294. https://doi.org/10.1016/j.optmat.2005.12.013.

[19] A. Ikesue, T. Kinoshita, K. Kamata, K. Yoshida, Fabrication and Optical Properties of High-Performance Polycrystalline Nd:YAG Ceramics for Solid-State Lasers, Journal of the American Ceramic Society 78 (1995) 1033–1040. https://doi.org/10.1111/j.1151-2916.1995.tb08433.x.

[20] G. Blasse, A. Bril, A New Phosphor for Flying-Spot Cathode-Ray Tubes For Color Television: Yellow-Emitting $Y_3Al_5O_{12}$–Ce^{3+}, Applied Physics Letters 11 (2004) 53–55. https://doi.org/10.1063/1.1755025.

[21] A.C. Berends, M.A. van de Haar, M.R. Krames, YAG:Ce^{3+} Phosphor: From Micron-Sized Workhorse for General Lighting to a Bright Future on the Nanoscale, Chem. Rev. 120 (2020) 13461–13479. https://doi.org/10.1021/acs.chemrev.0c00618.

[22] P. Bowen, C. Carry, From powders to sintered pieces: forming, transformations and sintering of nanostructured ceramic oxides, Powder

Technology 128 (2002) 248–255. https://doi.org/10.1016/S0032-5910(02)00183-3.

[23] G. Bilir, G. Ozen, M. Bettinelli, F. Piccinelli, M. Cesaria, B. Di Bartolo, Broadband Visible Light Emission From Nominally Undoped and Cr^{3+} Doped Garnet Nanopowders, IEEE Photonics Journal 6 (2014) 1–11. https://doi.org/10.1109/JPHOT.2014.2337873.

[24] M. Skruodiene, M. Misevicius, M. Sakalauskaite, A. Katelnikovas, R. Skaudzius, Doping effect of Tb3+ ions on luminescence properties of $Y_3Al_5O_{12}$:Cr^{3+} phosphor, Journal of Luminescence 179 (2016) 355–360. https://doi.org/10.1016/j.jlumin.2016.07.041.

[25] B. Bai, P. Dang, D. Huang, H. Lian, J. Lin, Broadband Near-Infrared Emitting $Ca_2LuScGa_2Ge_2O_{12}$:Cr^{3+} Phosphors: Luminescence Properties and Application in Light-Emitting Diodes, Inorg. Chem. 59 (2020) 13481–13488. https://doi.org/10.1021/acs.inorgchem.0c01890.

[26] L. Zhang, S. Zhang, Z. Hao, X. Zhang, G. Pan, Y. Luo, H. Wu, J. Zhang, A high efficiency broad-band near-infrared $Ca_2LuZr_2Al_3O_{12}$:Cr^{3+} garnet phosphor for blue LED chips, J. Mater. Chem. C 6 (2018) 4967–4976. https://doi.org/10.1039/C8TC01216D.

[27] M. Skruodiene, A. Katelnikovas, L. Vasylechko, R. Skaudzius, Tb^{3+} to Cr^{3+} energy transfer in a co-doped $Y_3Al_5O_{12}$ host, Journal of Luminescence 208 (2019) 327–333. https://doi.org/10.1016/j.jlumin.2018.12.048.

[28] M. Back, J. Ueda, M.G. Brik, T. Lesniewski, M. Grinberg, S. Tanabe, Revisiting Cr^{3+}-Doped $Bi_2Ga_4O_9$ Spectroscopy: Crystal Field Effect and Optical Thermometric Behavior of Near-Infrared-Emitting Singly-Activated Phosphors, ACS Appl. Mater. Interfaces 10 (2018) 41512–41524. https://doi.org/10.1021/acsami.8b15607.

[29] R. Skaudzius, J. Pinkas, R. Raudonis, A. Selskis, R. Juskenas, A. Kareiva, On the limitary radius of garnet structure compounds $Y_3Al_{5-x}M_xO_{12}$ (M = Cr, Co, Mn, Ni, Cu) and $Y_3Fe_{5-x}Co_xO_{12}$ ($0 \leq x \leq 2.75$) synthesized by sol–gel method, Materials Chemistry and Physics 135 (2012) 479–485. https://doi.org/10.1016/j.matchemphys.2012.05.011.

[30] T. Zhou, L. Zhang, Z. Li, S. Wei, J. Wu, L. Wang, H. Yang, Z. Fu, H. Chen, C. Wong, Q. Zhang, Enhanced conversion efficiency of Cr^{4+} ion in Cr: YAG transparent ceramic by optimizing the annealing process and doping concentration, Journal of Alloys and Compounds 703 (2017) 34–39. https://doi.org/10.1016/j.jallcom.2017.01.338.

[31] H. Lin, G. Bai, T. Yu, M.-K. Tsang, Q. Zhang, J. Hao, Site Occupancy and Near-Infrared Luminescence in $Ca_3Ga_2Ge_3O_{12}$: Cr^{3+} Persistent Phosphor, Advanced Optical Materials 5 (2017) 1700227. https://doi.org/10.1002/adom.201700227.

[32] E. Mobini, S. Rostami, M. Peysokhan, A. Albrecht, S. Kuhn, S. Hein, C. Hupel, J. Nold, N. Haarlammert, T. Schreiber, R. Eberhardt, A. Tünnermann, M. Sheik-Bahae, A. Mafi, Laser cooling of ytterbium-

doped silica glass, Commun Phys 3 (2020) 1–6. https://doi.org/10.1038/s42005-020-00401-6.

[33] S. Lin, H. Lin, G. Chen, B. Wang, X. Yue, Q. Huang, J. Xu, Y. Cheng, Y. Wang, Stable $CsPbBr_3$-Glass Nanocomposite for Low-Étendue Wide-Color-Gamut Laser-Driven Projection Display, Laser & Photonics Reviews 15 (2021) 2100044. https://doi.org/10.1002/lpor.202100044.

[34] R.L. Streever, Exchange interactions in rare-earth iron garnets, Journal of Magnetism and Magnetic Materials 241 (2002) 137–143. https://doi.org/10.1016/S0304-8853(01)00938-6.

[35] J.C. Waerenborgh, D.P. Rojas, A.L. Shaula, V.V. Kharton, F.M.B. Marques, Defect formation in $Gd_3Fe_5O_{12}$-based garnets: a Mössbauer spectroscopy study, Materials Letters 58 (2004) 3432–3436. https://doi.org/10.1016/j.matlet.2004.05.081.

[36] S.C. Parida, S.K. Rakshit, Z. Singh, Heat capacities, order–disorder transitions, and thermodynamic properties of rare-earth orthoferrites and rare-earth iron garnets, Journal of Solid State Chemistry 181 (2008) 101–121. https://doi.org/10.1016/j.jssc.2007.11.003.

[37] D. Petrov, Lattice enthalpies and magnetic loops in lanthanide iron garnets, $Ln_3Fe_5O_{12}$, The Journal of Chemical Thermodynamics 87 (2015) 136–140. https://doi.org/10.1016/j.jct.2015.03.005.

[38] O. Opuchovic, D. Niznansky, A. Kareiva, Thermoanalytical (TG/DSC/EVG–GC–MS) characterization of the lanthanide (Ho) iron garnet formation in sol–gel, J Therm Anal Calorim 130 (2017) 1085–1094. https://doi.org/10.1007/s10973-017-6492-0.

[39] V. Sharma, B.K. Kuanr, Magnetic and crystallographic properties of rare-earth substituted yttrium-iron garnet, Journal of Alloys and Compounds 748 (2018) 591–600. https://doi.org/10.1016/j.jallcom.2018.03.086.

[40] M. Nath, C. L. Sharma, N. Bharti, Rare Earth – Iron Mixed Oxides: A Review, Reviews in Inorganic Chemistry 20 (2000) 137–186. https://doi.org/10.1515/REVIC.2000.20.2.137.

[41] J.D. Adam, L.E. Davis, G.F. Dionne, E.F. Schloemann, S.N. Stitzer, Ferrite devices and materials, IEEE Transactions on Microwave Theory and Techniques 50 (2002) 721–737. https://doi.org/10.1109/22.989957.

[42] Y. Yang, T. Liu, L. Bi, L. Deng, Recent advances in development of magnetic garnet thin films for applications in spintronics and photonics, (2021). https://doi.org/10.1016/J.JALLCOM.2020.158235.

[43] D.L. Leslie-Pelecky, R.D. Rieke, Magnetic Properties of Nanostructured Materials, Chem. Mater. 8 (1996) 1770–1783. https://doi.org/10.1021/cm960077f.

[44] X. Batlle, A. Labarta, Finite-size effects in fine particles: magnetic and transport properties, J. Phys. D: Appl. Phys. 35 (2002) R15–R42. https://doi.org/10.1088/0022-3727/35/6/201.

[45] C.S. Kim, Y.R. Uhm, S.B. Kim, J.-G. Lee, Magnetic properties of $Y_{3-x}La_xFe_5O_{12}$ thin films grown by a sol–gel method, Journal of Magnetism and Magnetic Materials 215–216 (2000) 551–553. https://doi.org/10.1016/S0304-8853(00)00217-1.

[46] H. Xu, H. Yang, Magnetic properties of Ce,Dy-substituted yttrium iron garnet ferrite powders fabricated using a sol–gel method, Physica Status Solidi (a) 204 (2007) 1203–1209. https://doi.org/10.1002/pssa.200622524.

[47] Structural, Magnetic, Optical Properties and Photocatalytic Activity of Nanocrystalline Cobalt Ferrite Prepared by Three Different Methods, Biointerface Res Appl Chem 12 (2021) 1335–1351. https://doi.org/10.33263/BRIAC121.13351351.

[48] S.H. Choi, S.B. Kwon, J.H. Yoo, M. Na, B.Y. Kim, H. Yoon, S.H. Park, I. Kinski, B.K. Kang, D.H. Yoon, Y.H. Song, Fabrication of phosphor in glass using waste glass for automotive lighting application, Sci Rep 13 (2023) 4456. https://doi.org/10.1038/s41598-023-27685-2.

[49] E.B. Jones, V. Stevanović, The glassy solid as a statistical ensemble of crystalline microstates, Npj Comput Mater 6 (2020) 1–6. https://doi.org/10.1038/s41524-020-0329-2.

[50] Th.M. Nieuwenhuizen, Thermodynamics of the Glassy State: Effective Temperature as an Additional System Parameter, Phys. Rev. Lett. 80 (1998) 5580–5583. https://doi.org/10.1103/PhysRevLett.80.5580.

[51] B.E. Warren, X-ray Diffraction Study of the Structure of Glass., ACS Publications (2002). https://doi.org/10.1021/cr60084a007.

[52] B.E. Warren, J. Biscce, The Structure of Silica Glass by X-Ray Diffraction Studies, Journal of the American Ceramic Society 21 (1938) 49–54. https://doi.org/10.1111/j.1151-2916.1938.tb15742.x.

[53] R. Fulchiron, I. Belyamani, J.U. Otaigbe, V. Bounor-Legaré, A simple method for tuning the glass transition process in inorganic phosphate glasses, Sci Rep 5 (2015) 8369. https://doi.org/10.1038/srep08369.

[54] G. Tammann, Der glaszustand, L. Voss, 1933. https://books.google.lt/books?id=iqVPAQAAIAAJ.

[55] G. Tammann, W. Hesse, Die Abhängigkeit der Viscosität von der Temperatur bie unterkühlten Flüssigkeiten, Zeitschrift Für Anorganische Und Allgemeine Chemie 156 (1926) 245–257. https://doi.org/10.1002/zaac.19261560121.

[56] N.H. Ray, The structure and properties of inorganic polymeric phosphates, British Polymer Journal 11 (1979) 163–177. https://doi.org/10.1002/pi.4980110402.

[57] K.E. Gonsalves, Inorganic polymers. By J. E. Mark, H. R. Allcock and R. West, Prentice Hall, Englewood Cliffs, NJ 1992, 272 pp., ISBN 0-13-465881-7, Advanced Materials 5 (1993) 63–63. https://doi.org/10.1002/adma.19930050116.

[58] A. Kovacs, Glass transition in amorphous polymers: a phenomenological study, Adv. Polym. Sci 3 (1963) 394–507.

[59] C. Austen Angell, S. Sivarajan, Glass Transition, in: Reference Module in Materials Science and Materials Engineering, Elsevier, 2017. https://doi.org/10.1016/B978-0-12-803581-8.03155-6.

[60] T.V. Tropin, J.W.P. Schmelzer, C. Schick, On the dependence of the properties of glasses on cooling and heating rates II: Prigogine–Defay ratio, fictive temperature and fictive pressure, Journal of Non-Crystalline Solids 357 (2011) 1303–1309. https://doi.org/10.1016/j.jnoncrysol.2010.12.005.

[61] W.H. Zachariasen, The Atomic Arrangement in Glass, J. Am. Chem. Soc. 54 (1932) 3841–3851. https://doi.org/10.1021/ja01349a006.

[62] B.E. Warren, X-ray Diffraction Study of the Structure of Glass., Chem. Rev. 26 (1940) 237–255. https://doi.org/10.1021/cr60084a007.

[63] R.L. Mozzi, B.E. Warren, The structure of vitreous boron oxide, J Appl Cryst 3 (1970) 251–257. https://doi.org/10.1107/S0021889870006143.

[64] A.I. Priven, Evaluation of the fraction of fourfold-coordinated boron in oxide glasses from their composition, Glass Phys Chem 26 (2000) 441–454. https://doi.org/10.1007/BF02732065.

[65] G.E. Jellison, P.J. Bray, A structural interpretation of B^{10} and B^{11} NMR spectra in sodium borate glasses, Journal of Non-Crystalline Solids 29 (1978) 187–206. https://doi.org/10.1016/0022-3093(78)90113-8.

[66] M. Abdel-Baki, F. El-Diasty, Role of oxygen on the optical properties of borate glass doped with ZnO, Journal of Solid State Chemistry 184 (2011) 2762–2769. https://doi.org/10.1016/j.jssc.2011.08.015.

[67] W.J. Dell, P.J. Bray, S.Z. Xiao, 11B NMR studies and structural modeling of $Na_2O{\cdot}B_2O_3{\cdot}SiO_2$ glasses of high soda content, Journal of Non-Crystalline Solids 58 (1983) 1–16. https://doi.org/10.1016/0022-3093(83)90097-2.

[68] M.M. Smedskjaer, J.C. Mauro, R.E. Youngman, C.L. Hogue, M. Potuzak, Y. Yue, Topological Principles of Borosilicate Glass Chemistry, J. Phys. Chem. B 115 (2011) 12930–12946. https://doi.org/10.1021/jp208796b.

[69] J. Wu, J.F. Stebbins, Temperature and modifier cation field strength effects on aluminoborosilicate glass network structure, Journal of Non-Crystalline Solids 362 (2013) 73–81. https://doi.org/10.1016/j.jnoncrysol.2012.11.005.

[70] P.N. Sen, M.F. Thorpe, Phonons in AX_2 glasses: From molecular to band-like modes, Phys. Rev. B 15 (1977) 4030–4038. https://doi.org/10.1103/PhysRevB.15.4030.

[71] A.C. Hannon, B. Vessal, J.M. Parker, The structure of alkali silicate glasses, Journal of Non-Crystalline Solids 150 (1992) 97–102. https://doi.org/10.1016/0022-3093(92)90102-P.

[72] D.W. Matson, S.K. Sharma, J.A. Philpotts, The structure of high-silica alkali-silicate glasses. A Raman spectroscopic investigation, Journal of Non-Crystalline Solids 58 (1983) 323–352. https://doi.org/10.1016/0022-3093(83)90032-7.

[73] Y. Onodera, Y. Takimoto, H. Hijiya, T. Taniguchi, S. Urata, S. Inaba, S. Fujita, I. Obayashi, Y. Hiraoka, S. Kohara, Origin of the mixed alkali effect in silicate glass, NPG Asia Mater 11 (2019) 1–11. https://doi.org/10.1038/s41427-019-0180-4.

[74] C. Huang, A.N. Cormack, Structural differences and phase separation in alkali silicate glasses, The Journal of Chemical Physics 95 (1991) 3634–3642. https://doi.org/10.1063/1.460814.

[75] G.S. Henderson, The structure uf silicate melts: a glass perspective, The Canadian Mineralogist 43 (2005) 1921–1958. https://doi.org/10.2113/gscanmin.43.6.1921.

[76] R.K. Brow, Review: the structure of simple phosphate glasses, Journal of Non-Crystalline Solids 263–264 (2000) 1–28. https://doi.org/10.1016/S0022-3093(99)00620-1.

[77] F. Muñoz, J. Rocherullé, I. Ahmed, L. Hu, Phosphate Glasses, in: J.D. Musgraves, J. Hu, L. Calvez (Eds.), Springer Handbook of Glass, Springer International Publishing, Cham, 2019: pp. 553–594. https://doi.org/10.1007/978-3-319-93728-1_16.

[78] U. Hoppe, A structural model for phosphate glasses, Journal of Non-Crystalline Solids 195 (1996) 138–147. https://doi.org/10.1016/0022-3093(95)00524-2.

[79] U. Hoppe, G. Walter, R. Kranold, D. Stachel, Structural specifics of phosphate glasses probed by diffraction methods: a review, Journal of Non-Crystalline Solids 263–264 (2000) 29–47. https://doi.org/10.1016/S0022-3093(99)00621-3.

[80] M. Karabulut, E. Melnik, R. Stefan, G.K. Marasinghe, C.S. Ray, C.R. Kurkjian, D.E. Day, Mechanical and structural properties of phosphate glasses, Journal of Non-Crystalline Solids 288 (2001) 8–17. https://doi.org/10.1016/S0022-3093(01)00615-9.

[81] R.K. Brow, C.A. Click, T.M. Alam, Modifier coordination and phosphate glass networks, Journal of Non-Crystalline Solids 274 (2000) 9–16. https://doi.org/10.1016/S0022-3093(00)00178-2.

[82] K.S. Andrikopoulos, A.G. Kalampounias, O. Falagara, S.N. Yannopoulos, The glassy and supercooled state of elemental sulfur: Vibrational modes, structure metastability, and polymer content, The Journal of Chemical Physics 139 (2013) 124501. https://doi.org/10.1063/1.4821592.

[83] B. Meyer, T.V. Oommen, D. Jensen, Color of liquid sulfur, ACS Publications (2002). https://doi.org/10.1021/j100677a012.

[84] R.G. Brandes, F.P. Laming, A.D. Pearson, Optically Formed Dielectric Gratings in Thick Films of Arsenic–Sulfur Glass, Appl. Opt., AO 9 (1970) 1712–1714. https://doi.org/10.1364/AO.9.001712.

[85] Y. Huang, F. Chen, R. Lin, X. Zhang, S. Dai, Q. Nie, X. Zhang, Glass formation and mid-infrared optical nonlinearities of chalcogenide glasses in germanium-tin-sulfur ternary system, Opt. Mater. Express, OME 6 (2016) 3053–3062. https://doi.org/10.1364/OME.6.003053.

[86] A. Morvan, N. Delpouve, A. Vella, A. Saiter-Fourcin, Physical aging of selenium glass: Assessing the double mechanism of equilibration and the crystallization process, Journal of Non-Crystalline Solids 570 (2021) 121013. https://doi.org/10.1016/j.jnoncrysol.2021.121013.

[87] J.-P. Guin, T. Rouxel, J.-C. Sanglebœuf, I. Melscoët, J. Lucas, Hardness, Toughness, and Scratchability of Germanium–Selenium Chalcogenide Glasses, Journal of the American Ceramic Society 85 (2002) 1545–1552. https://doi.org/10.1111/j.1151-2916.2002.tb00310.x.

[88] S. Cui, R. Chahal, C. Boussard-Plédel, V. Nazabal, J.-L. Doualan, J. Troles, J. Lucas, B. Bureau, From Selenium- to Tellurium-Based Glass Optical Fibers for Infrared Spectroscopies, Molecules 18 (2013) 5373–5388. https://doi.org/10.3390/molecules18055373.

[89] P.M. Smith, A.J. Leadbetter, A.J. Apling, The structures of orthorhombic and vitreous arsenic, The Philosophical Magazine: A Journal of Theoretical Experimental and Applied Physics 31 (1975) 57–64. https://doi.org/10.1080/14786437508229285.

[90] J.D. Musgraves, P. Wachtel, S. Novak, J. Wilkinson, K. Richardson, Composition dependence of the viscosity and other physical properties in the arsenic selenide glass system, Journal of Applied Physics 110 (2011) 063503. https://doi.org/10.1063/1.3638122.

[91] A.J. Leadbetter, A.J. Apling, Diffraction studies of glass structure: (V). The structure of some arsenic chalcogenide glasses, Journal of Non-Crystalline Solids 15 (1974) 250–268. https://doi.org/10.1016/0022-3093(74)90052-0.

[92] R.C.E. Jr, Vitreous Phosphorus, ACS Publications (2002). https://doi.org/10.1021/ic50005a006.

[93] G.M. Jenkins, K. Kawamura, Structure of Glassy Carbon, Nature 231 (1971) 175–176. https://doi.org/10.1038/231175a0.

[94] S. Sharma, Glassy Carbon: A Promising Material for Micro- and Nanomanufacturing, Materials 11 (2018) 1857. https://doi.org/10.3390/ma11101857.

[95] T. Noda, M. Inagaki, The Structure of Glassy Carbon, Bulletin of the Chemical Society of Japan 37 (1964) 1534–1538. https://doi.org/10.1246/bcsj.37.1534.

[96] S. Yamada, H. Sato, Some Physical Properties of Glassy Carbon, Nature 193 (1962) 261–262. https://doi.org/10.1038/193261b0.

[97] C.M. Baldwin, R.M. Almeida, J.D. Mackenzie, Halide glasses, Journal of Non-Crystalline Solids 43 (1981) 309–344. https://doi.org/10.1016/0022-3093(81)90101-0.

[98] M. Poulain, Halide glasses, Journal of Non-Crystalline Solids 56 (1983) 1–14. https://doi.org/10.1016/0022-3093(83)90439-8.

[99] J. Portier, Halogenide, chalcogenide and chalcohalogenide glasses: materials, models, applications, Journal of Non-Crystalline Solids 112 (1989) 15–22. https://doi.org/10.1016/0022-3093(89)90489-4.

[100] V.Q. Nguyen, J.S. Sanghera, I.D. Aggarwal, I.K. Lloyd, Physical Properties of Chalcogenide and Chalcohalide Glasses, Journal of the American Ceramic Society 83 (2000) 855–859. https://doi.org/10.1111/j.1151-2916.2000.tb01285.x.

[101] B. Bureau, X.H. Zhang, F. Smektala, J.-L. Adam, J. Troles, H. Ma, C. Boussard-Plèdel, J. Lucas, P. Lucas, D. Le Coq, M.R. Riley, J.H. Simmons, Recent advances in chalcogenide glasses, Journal of Non-Crystalline Solids 345–346 (2004) 276–283. https://doi.org/10.1016/j.jnoncrysol.2004.08.096.

[102] A. Zakery, S.R. Elliott, Optical properties and applications of chalcogenide glasses: a review, Journal of Non-Crystalline Solids 330 (2003) 1–12. https://doi.org/10.1016/j.jnoncrysol.2003.08.064.

[103] L. Zhenhua, Chemical bond approach to the chalcogenide glass forming tendency, Journal of Non-Crystalline Solids 127 (1991) 298–305. https://doi.org/10.1016/0022-3093(91)90482-L.

[104] V. Dimitrov, T. Komatsu, Classification of oxide glasses: A polarizability approach, Journal of Solid State Chemistry 178 (2005) 831–846. https://doi.org/10.1016/j.jssc.2004.12.013.

[105] Z.P. Lu, C.T. Liu, Glass Formation Criterion for Various Glass-Forming Systems, Phys. Rev. Lett. 91 (2003) 115505. https://doi.org/10.1103/PhysRevLett.91.115505.

[106] A.I. Priven, General method for calculating the properties of oxide glasses and glass forming melts from their composition and temperature, Glass Technology 45 (2004) 244–254.

[107] N. Boubata, A. Roula, I. Moussaoui, Thermodynamic and relative approach to compute glass-forming ability of oxides, Bull Mater Sci 36 (2013) 457–460. https://doi.org/10.1007/s12034-013-0494-8.

[108] K.-U. Hess, J.E.K. Schawe, M. Wilding, B. Purgstaller, K.E. Goetschl, S. Sturm, K. Müller-Caspary, E.V. Sturm, W. Schmahl, E. Griesshaber, T. Bissbort, D. Weidendorfer, M. Dietzel, D.B. Dingwell, Glass transition temperatures and crystallization kinetics of a synthetic, anhydrous, amorphous calcium-magnesium carbonate, Philosophical Transactions of the Royal Society A: Mathematical, Physical and Engineering Sciences 381 (2023) 20220356. https://doi.org/10.1098/rsta.2022.0356.

[109] D. Weidendorfer, K.-U. Hess, R.M. Ruhekenya, J.E.K. Schawe, M.C. Wilding, D.B. Dingwell, Effect of water on the glass transition of a potassium-magnesium carbonate melt, Philosophical Transactions of the Royal Society A: Mathematical, Physical and Engineering Sciences 381 (2023) 20220355. https://doi.org/10.1098/rsta.2022.0355.

[110] J.D. Mackenzie, Applications of zachariasen's rules to different types of noncrystalline solids, Journal of Non-Crystalline Solids 95–96 (1987) 441–448. https://doi.org/10.1016/S0022-3093(87)80142-4.

[111] K.-H. Sun, Fundamental Condition of Glass Formation, Journal of the American Ceramic Society 30 (1947) 277–281. https://doi.org/10.1111/j.1151-2916.1947.tb19654.x.

[112] K. Kühne, 7. Literaturverzeichnis, in: 7. Literaturverzeichnis, De Gruyter, 2022: pp. 307–319. https://doi.org/10.1515/9783112540961-025.

[113] Les causes et les effets de la trempe du verre - 2 tirés à part extraits de la Revue d'Optique Théorique et Instrumentale - 1. Tome 15, n° 9, septembre 1936 (17 pages, 8 figures) - 2. Tome 16 (1937), (25 pages, 10 figures), n.d. https://www.livre-rare-book.com/book/5472375/65178 (accessed April 28, 2024).

[114] V.S. Minaev, V.P. Vassiliev, S.P. Timoshenkov, The new approach to the vitrification process, (n.d.).

[115] M.C. Ball, C.M. Snelling, A.N. Strachan, Dehydration of sodium carbonate monohydrate, J. Chem. Soc., Faraday Trans. 1 81 (1985) 1761–1766. https://doi.org/10.1039/F19858101761.

[116] E. Meechoowas, P. Ketboonruang, K. Tapasa, T. Jitwatcharakomol, Improve melting glass efficiency by Batch-to melt conversion, Procedia Engineering 32 (2012) 956–961. https://doi.org/10.1016/j.proeng.2012.02.038.

[117] J.-W. Kim, Y.-D. Lee, H.-G. Lee, Decomposition of Na2CO3 by Interaction with SiO2 in Mold Flux of Steel Continuous Casting, ISIJ International 41 (2001) 116–123. https://doi.org/10.2355/isijinternational.41.116.

[118] A.I. Zaitsev, N.E. Shelkova, N.P. Lyakishev, B.M. Mogutnov, Thermodynamic properties and phase equilibria in the Na 2 O–SiO 2 system, Physical Chemistry Chemical Physics 1 (1999) 1899–1907. https://doi.org/10.1039/A809003C.

[119] P. Niggli, The phenomena of equilibria between silica and the alcali carbonates, ACS Publications (2002). https://doi.org/10.1021/ja02200a004.

[120] M. Cable, A Century of Developments in Glassmelting Research, Journal of the American Ceramic Society 81 (1998) 1083–1094. https://doi.org/10.1111/j.1151-2916.1998.tb02455.x.

[121] L. Němec, P. Cincibusová, Glass melting and its innovation potentials: the potential role of glass flow in the sand-dissolution process, (2009).

[122] R.G.C. Beerkens, Sulfate Decomposition and Sodium Oxide Activity in Soda–Lime–Silica Glass Melts, Journal of the American Ceramic Society 86 (2003) 1893–1899. https://doi.org/10.1111/j.1151-2916.2003.tb03578.x.

[123] D.-S. Kim, P. Hrma, Foaming in Glass Melts Produced by Sodium Sulfate Decomposition under Ramp Heating Conditions, Journal of the American Ceramic Society 75 (1992) 2959–2963. https://doi.org/10.1111/j.1151-2916.1992.tb04371.x.

[124] S. Tanimoto, T. Rehren, Interactions between silicate and salt melts in LBA glassmaking, Journal of Archaeological Science 35 (2008) 2566–2573. https://doi.org/10.1016/j.jas.2008.04.016.

[125] R. Conradt, Prospects and physical limits of processes and technologies in glass melting, Journal of Asian Ceramic Societies (2019). https://www.tandfonline.com/doi/abs/10.1080/21870764.2019.1656360 (accessed April 28, 2024).

[126] L. Němec, M. Jebavá, P. Dyrčíková, Glass melting phenomena, their ordering and melting space utilisation, (2013).

[127] M. Hujova, Influence of fining agents on glass melting: a review, Part 1, Ceramics - Silikaty (2017) 119–126. https://doi.org/10.13168/cs.2017.0006.

[128] C. Lin, C. Rüssel, S. Dai, Chalcogenide glass-ceramics: Functional design and crystallization mechanism, Progress in Materials Science 93 (2018) 1–44. https://doi.org/10.1016/j.pmatsci.2017.11.001.

[129] M. He, J. Jia, J. Zhao, X. Qiao, J. Du, X. Fan, Glass-ceramic phosphors for solid state lighting: A review, Ceramics International 47 (2021) 2963–2980. https://doi.org/10.1016/j.ceramint.2020.09.227.

[130] Yu.B. Petrov, Yu.P. Udalov, J. Slovak, Yu.G. Morozov, Liquid Immiscibility Phenomena in Melts of the ZrO_2–FeO–Fe_2O_3 System, Glass Physics and Chemistry 28 (2002) 139–146. https://doi.org/10.1023/A:1016043117024.

[131] P. Hudon, D.R. Baker, The nature of phase separation in binary oxide melts and glasses. I. Silicate systems, Journal of Non-Crystalline Solids 303 (2002) 299–345. https://doi.org/10.1016/S0022-3093(02)01043-8.

[132] P. Hudon, D.R. Baker, The nature of phase separation in binary oxide melts and glasses. II. Selective solution mechanism, Journal of Non-Crystalline Solids 303 (2002) 346–353. https://doi.org/10.1016/S0022-3093(02)01044-X.

[133] P. Hudon, D.R. Baker, The nature of phase separation in binary oxide melts and glasses. III. Borate and germanate systems, Journal of Non-Crystalline Solids 303 (2002) 354–371. https://doi.org/10.1016/S0022-3093(02)01045-1.

[134] D. Chen, Z. Wan, Y. Zhou, Y. Chen, H. Yu, H. Lu, Z. Ji, P. Huang, Lanthanide-activated $Na_5Gd_9F_{32}$ nanocrystals precipitated from a borosilicate glass: Phase-separation-controlled crystallization and optical property, Journal of Alloys and Compounds 625 (2015) 149–157. https://doi.org/10.1016/j.jallcom.2014.11.128.

[135] H. Segawa, H. Yoshimizu, N. Hirosaki, S. Inoue, Fabrication of silica glass containing yellow oxynitride phosphor by the sol–gel process, Science and Technology of Advanced Materials 12 (2011) 034407. https://doi.org/10.1088/1468-6996/12/3/034407.

[136] H. Lin, E.Y.-B. Pun, X. Wang, X. Liu, Intense visible fluorescence and energy transfer in Dy^{3+}, Tb^{3+}, Sm^{3+} and Eu^{3+} doped rare-earth borate

glasses, Journal of Alloys and Compounds 390 (2005) 197–201. https://doi.org/10.1016/j.jallcom.2004.07.068.

[137] A. Van Die, A.C.H.I. Leenaers, G. Blasse, W.F. Van Der Weg, Germanate glasses as hosts for luminescence of Mn^{2+} and Cr^{3+}, Journal of Non-Crystalline Solids 99 (1988) 32–44. https://doi.org/10.1016/0022-3093(88)90455-3.

[138] B. Dunn, J.I. Zink, Optical properties of sol–gel glasses doped with organic molecules, J. Mater. Chem. 1 (1991) 903–913. https://doi.org/10.1039/JM9910100903.

[139] S. Baccaro, A. Cemmi, I. Di Sarcina, F. Menchini, Gamma Rays Effects on the Optical Properties of Cerium-Doped Glasses, International Journal of Applied Glass Science 6 (2015) 295–301. https://doi.org/10.1111/ijag.12131.

[140] P.R.N. A, P. R, V. N, B. P, K.M. N, Neodymium-doped magnesium phosphate glasses for NIR laser applications at 1.05 μm, Mater. Res. Express 6 (2019) 096204. https://doi.org/10.1088/2053-1591/ab318e.

[141] D. A.v., P. Murugasen, P. Muralimanohar, S.P. Kumar, Optical studies of lanthanum oxide doped phosphate glasses, Optik 160 (2018) 348–352. https://doi.org/10.1016/j.ijleo.2018.01.108.

[142] F.H. ElBatal, M.A. Marzouk, H.A. ElBatal, Optical and crystallization studies of titanium dioxide doped sodium and potassium silicate glasses, Journal of Molecular Structure 1121 (2016) 54–59. https://doi.org/10.1016/j.molstruc.2016.05.052.

[143] H. Dong, Y. Chen, Y. Jiao, Q. Zhou, Y. Cheng, H. Zhang, Y. Lu, S. Wang, C. Yu, L. Hu, Nanocrystalline Yb:YAG-Doped Silica Glass with Good Transmittance and Significant Spectral Performance Enhancements, Nanomaterials (Basel) 12 (2022) 1263. https://doi.org/10.3390/nano12081263.

[144] H. Gong, X. Zhao, X. Yu, T. Setsuhisa, H. Lin, [Optical and spectral parameters in Ce^{3+} -doped gadolinium gallium aluminum garnet glass-ceramics], Guang Pu Xue Yu Guang Pu Fen Xi 30 (2010) 128–132.

[145] Q. Chen, P. Lin, W. Niu, H. Li, C. Jiang, J. Xu, J. Li, T. Lin, P. He, W. Long, H. Liu, Y. Liu, Microstructure and properties of YIG/bismuth-based composite glass/YIG joints with growth of in situ $MgFe_2O_4$ whiskers, Materials Characterization 169 (2020) 110593. https://doi.org/10.1016/j.matchar.2020.110593.

[146] S. Nishikawa, Crystal Structure of a Garnet, Tokyo Sugaku-Buturigakkwai Kizi Dai 2 Ki 9 (1917) 194–197. https://doi.org/10.11429/ptmps1907.9.8_194.

[147] G. Menzer, XX. Die Kristallstruktur der Granate, Zeitschrift für Kristallographie - Crystalline Materials 69 (1929) 300–396. https://doi.org/10.1524/zkri.1929.69.1.300.

[148] H.S. Yoder, M.L. Keith, Complete substitution of aluminum for silicon: The system $3MnO \cdot Al_2O_3 \cdot 3SiO_2$—$3Y_2O_3 \cdot 5Al_2O_3$, American Mineralogist 36 (1951) 519–533.

[149] E.J.W. Whittaker, (R. W. G.) Wyckoff. Crystal Structures. Vol. 3. (2nd edn). New York, London, Sydney (Interseience Publishers), 1965, viii+981 pp. illus. Mineralogical Magazine and Journal of the Mineralogical Society 35 (1966) 1022–1024. https://doi.org/10.1180/minmag.1966.035.275.20.

[150] F. Euler, J.A. Bruce, Oxygen coordinates of compounds with garnet structure, Acta Cryst 19 (1965) 971–978. https://doi.org/10.1107/S0365110X65004747.

[151] M.M. Kuklja, R. Pandey, Atomistic Modeling of Native Point Defects in Yttrium Aluminum Garnet Crystals, Journal of the American Ceramic Society 82 (1999) 2881–2886. https://doi.org/10.1111/j.1151-2916.1999.tb02172.x.

[152] C.-S. Chou, C.-Y. Wu, C.-H. Yeh, R.-Y. Yang, J.-H. Chen, The optimum conditions for solid-state-prepared $(Y_{3-x}Ce_x)Al_5O_{12}$ phosphor using the Taguchi method, Advanced Powder Technology 23 (2012) 97–103. https://doi.org/10.1016/j.apt.2010.12.016.

[153] C. Li, H. Zuo, M. Zhang, J. Han, S. Meng, Fabrication of transparent YAG ceramics by traditional solid-state-reaction method, Transactions of Nonferrous Metals Society of China 17 (2007) 148–153. https://doi.org/10.1016/S1003-6326(07)60064-8.

[154] T. Pawlik, M. Sopicka-Lizer, D. Michalik, J. Plewa, Application of mechanochemical processing to synthesis of YAG: Ce garnet powder, Archives of Metallurgy and Materials (2011).

[155] Annalen der Physik, J. A. Barth, 1888.

[156] F. Wang, X. Liu, Recent advances in the chemistry of lanthanide-doped upconversion nanocrystals, Chemical Society Reviews 38 (2009) 976–989. https://doi.org/10.1039/B809132N.

[157] Y. Zhang, J. Hao, Metal-ion doped luminescent thin films for optoelectronic applications, J. Mater. Chem. C 1 (2013) 5607–5618. https://doi.org/10.1039/C3TC31024H.

[158] W. Ryba-Romanowski, S. Golab, G. Dominiak-Dzik, M. Berkowski, Optical spectra of a $LaGaO_3$ crystal singly doped with chromium, vanadium and cobalt, Journal of Alloys and Compounds 288 (1999) 262–268. https://doi.org/10.1016/S0925-8388(99)00117-6.

[159] G. Murugadoss, Luminescence properties of co-doped ZnS:Ni, Mn and ZnS:Cu, Cd nanoparticles, Journal of Luminescence 132 (2012) 2043–2048. https://doi.org/10.1016/j.jlumin.2012.02.011.

[160] T. Xu, L. Yuan, Y. Chen, Y. Zhao, L. Ding, J. Liu, W. Xiang, X. Liang, $Y_3Al_5O_{12}:Ce^{3+}$ single crystal and red-emitting $Y_3Al_5O_{12}:Cr^{3+}$ single crystal for high power W-LEDs, Optical Materials 91 (2019) 30–34. https://doi.org/10.1016/j.optmat.2019.03.010.

[161] Nanomaterials | Free Full-Text | Enhancing the Relative Sensitivity of V^{5+}, V^{4+} and V^{3+} Based Luminescent Thermometer by the Optimization of the Stoichiometry of $Y_3Al_{5-x}Ga_xO_{12}$ Nanocrystals | HTML, (n.d.).

https://www.mdpi.com/2079-4991/9/10/1375/htm (accessed October 31, 2022).

[162] Enhancing Luminescence and Controlling the Mn Valence State of $Gd_3Ga_{5-x-\delta}Al_{x-y+\delta}O_{12}$:yMn Phosphors by the Design of the Garnet Structure | ACS Applied Materials & Interfaces, (n.d.). https://pubs.acs.org/doi/full/10.1021/acsami.9b20915 (accessed October 31, 2022).

[163] K. Kniec, K. Ledwa, K. Maciejewska, L. Marciniak, Intentional modification of the optical spectral response and relative sensitivity of luminescent thermometers based on Fe^{3+},Cr^{3+},Nd^{3+} co-doped garnet nanocrystals by crystal field strength optimization, Mater. Chem. Front. 4 (2020) 1697–1705. https://doi.org/10.1039/D0QM00097C.

[164] G. Murugadoss, Luminescence properties of co-doped ZnS:Ni, Mn and ZnS:Cu, Cd nanoparticles, Journal of Luminescence 132 (2012) 2043–2048. https://doi.org/10.1016/j.jlumin.2012.02.011.

[165] T. Xu, L. Yuan, Y. Chen, Y. Zhao, L. Ding, J. Liu, W. Xiang, X. Liang, $Y_3Al_5O_{12}$:Ce^{3+} single crystal and red-emitting $Y_3Al_5O_{12}$:Cr^{3+} single crystal for high power W-LEDs, Optical Materials 91 (2019) 30–34. https://doi.org/10.1016/j.optmat.2019.03.010.

[166] M.D. Seltzer, Interpretation of the Emission Spectra of Trivalent Chromium-Doped Garnet Crystals Using Tanabe-Sugano Diagrams, J. Chem. Educ. 72 (1995) 886. https://doi.org/10.1021/ed072p886.

[167] M. Skruodiene, A. Katelnikovas, L. Vasylechko, R. Skaudzius, Tb^{3+} to Cr^{3+} energy transfer in a co-doped $Y_3Al_5O_{12}$ host, Journal of Luminescence 208 (2019) 327–333. https://doi.org/10.1016/j.jlumin.2018.12.048.

[168] K. Elzbieciak, L. Marciniak, The Impact of Cr^{3+} Doping on Temperature Sensitivity Modulation in Cr^{3+} Doped and Cr^{3+}, Nd^{3+} Co-doped $Y_3Al_5O_{12}$, $Y_3Al_2Ga_3O_{12}$, and $Y_3Ga_5O_{12}$ Nanothermometers, Frontiers in Chemistry 6 (2018). https://www.frontiersin.org/articles/10.3389/fchem.2018.00424 (accessed October 31, 2022).

[169] P. Głuchowski, R. Pązik, D. Hreniak, W. Stręk, Luminescence properties of Cr^{3+}:Y3Al5O12 nanocrystals, Journal of Luminescence 129 (2009) 548–553. https://doi.org/10.1016/j.jlumin.2008.12.012.

[170] T. Xu, L. Yuan, Y. Chen, Y. Zhao, L. Ding, J. Liu, W. Xiang, X. Liang, $Y_3Al_5O_{12}$:Ce^{3+} single crystal and red-emitting $Y_3Al_5O_{12}$:Cr^{3+} single crystal for high power W-LEDs, Optical Materials 91 (2019) 30–34. https://doi.org/10.1016/j.optmat.2019.03.010.

[171] H. Yagi, T. Yanagitani, H. Yoshida, M. Nakatsuka, K. Ueda, The optical properties and laser characteristics of Cr^{3+} and Nd^{3+} co-doped $Y_3Al_5O_{12}$ ceramics, Optics & Laser Technology 39 (2007) 1295–1300. https://doi.org/10.1016/j.optlastec.2006.06.016.

[172] L.-M. Shao, X.-P. Jing, Energy transfer and luminescent properties of Ce^{3+}, Cr^{3+} co-doped $Y_3Al_5O_{12}$, Journal of Luminescence 131 (2011) 1216–1221. https://doi.org/10.1016/j.jlumin.2011.02.019.

[173] A. Zabiliūtė, S. Butkutė, A. Žukauskas, P. Vitta, A. Kareiva, Sol-gel synthesized far-red chromium-doped garnet phosphors for phosphor-conversion light-emitting diodes that meet the photomorphogenetic needs of plants, Appl. Opt., AO 53 (2014) 907–914. https://doi.org/10.1364/AO.53.000907.

[174] L. Chen, C.-C. Lin, C.-W. Yeh, R.-S. Liu, Light Converting Inorganic Phosphors for White Light-Emitting Diodes, Materials 3 (2010) 2172–2195. https://doi.org/10.3390/ma3032172.

[175] S. Inaho, S. Shionoya, T. Hase, W.M. Yen, K. Iga, H. Yamamoto, K. Kohmoto, H. Sasakura, G. Hatakoshi, T. Inoguchi, S. Tanaka, S. Kanaya, T. Yoshioka, M. Kobayashi, H. Kobayashi, S. Tanimizu, H. Mizuno, K. Murakami, M. Yoshida, toshiya Yokogawa, T. Takahara, M. Morita, A.M. Srivastava, P.R. Ravilisetty, X. Wang, D.D. Jia, R.-J. Xie, C. Adachi, H. Tamaki, K. Narisada, N. Hashimoto, S. Nakajima, Y. Itsuki, H. Matsunami, S. Payne, B. Tissue, W. Jia, R.P. Rao, R.S. Meltzer, S. Nakamura, Y. Murayama, K. Narita, M. Ogawa, A. Mikami, Y. Komine, A. Suzuki, Y. Masumoto, K. Morimoto, K. Takahashi, S. Hayakawa, Y. Tomita, K. Ohno, K. Urabe, S. Ibuki, H. Yamamoto, M. Tamatani, S. Miyahara, N. Miura, T. Kano, S. Kamiya, S. Nara, T. Tsutsui, E. Nakazawa, Y. Mita, Phosphor Handbook, 2nd ed., CRC Press, Boca Raton, 2017. https://doi.org/10.1201/9781315222066.

[176] Nitride Phosphors and Solid-State Lighting, Routledge & CRC Press (n.d.). https://www.routledge.com/Nitride-Phosphors-and-Solid-State-Lighting/Xie-Li-Hirosaki-Yamamoto/p/book/9780367576950 (accessed October 31, 2022).

[177] J.F. Ready, ed., Preface, in: Industrial Applications of Lasers (Second Edition), Academic Press, San Diego, 1997: pp. xv–xvi. https://doi.org/10.1016/B978-012583961-7/50000-4.

[178] G. Blasse, B.C. Grabmaier, Luminescent Materials, Springer, Berlin, Heidelberg, 1994. https://doi.org/10.1007/978-3-642-79017-1.

[179] Y. Wang, K. Zheng, S. Song, D. Fan, H. Zhang, X. Liu, Remote manipulation of upconversion luminescence, Chem. Soc. Rev. 47 (2018) 6473–6485. https://doi.org/10.1039/C8CS00124C.

[180] P.A. Tanner, Some misconceptions concerning the electronic spectra of tri-positive europium and cerium, Chem. Soc. Rev. 42 (2013) 5090–5101. https://doi.org/10.1039/C3CS60033E.

[181] M.A. Musa, R.S. Azis, N.H. Osman, J. Hassan, T. Zangina, Structural and magnetic properties of yttrium iron garnet (YIG) and yttrium aluminum iron garnet (YAlG) nanoferrite via sol-gel synthesis, Results in Physics 7 (2017) 1135–1142. https://doi.org/10.1016/j.rinp.2017.02.038.

[182] M. Rajendran, S. Deka, P.A. Joy, A.K. Bhattacharya, Size-dependent magnetic properties of nanocrystalline yttrium iron garnet powders, Journal of Magnetism and Magnetic Materials 301 (2006) 212–219. https://doi.org/10.1016/j.jmmm.2005.06.027.

[183] Y.F. Chen, K.T. Wu, Y.D. Yao, C.H. Peng, K.L. You, W.S. Tse, The influence of Fe concentration on $Y_3Al_{5-x}Fe_xO_{12}$ garnets, Microelectronic Engineering 81 (2005) 329–335. https://doi.org/10.1016/j.mee.2005.03.028.

[184] E.J.J. Mallmann, A.S.B. Sombra, J.C. Goes, P.B.A. Fechine, Yttrium Iron Garnet: Properties and Applications Review, Solid State Phenomena 202 (2013) 65–96. https://doi.org/10.4028/www.scientific.net/SSP.202.65.

[185] A. Mergen, A. Qureshi, Characterization of YIG nanopowders by mechanochemical synthesis, Journal of Alloys and Compounds 478 (2009) 741–744. https://doi.org/10.1016/j.jallcom.2008.11.133.

[186] O. Opuchovic, A. Beganskiene, A. Kareiva, Sol–gel derived $Tb_3Fe_5O_{12}$ and $Y_3Fe_5O_{12}$ garnets: Synthesis, phase purity, micro-structure and improved design of morphology, Journal of Alloys and Compounds 647 (2015) 189–197. https://doi.org/10.1016/j.jallcom.2015.05.169.

[187] K. Praveena, K. Sadhana, S. Srinath, S.R. Murthy, Structural and magnetic properties of nanocrystalline $Y_3Fe_5O_{12}$ using co-precipitation method, AIP Conference Proceedings 1447 (2012) 291–292. https://doi.org/10.1063/1.4709994.

[188] F. Xue, J. Huang, T. Li, Z. Wang, X. Zhou, L. Wei, B. Gao, Y. Zhai, Q. Li, Q. Xu, J. Du, Lowering the synthesis temperature of $Y_3Fe_5O_{12}$ by surfactant assisted solid state reaction, Journal of Magnetism and Magnetic Materials 446 (2018) 118–124. https://doi.org/10.1016/j.jmmm.2017.08.076.

[189] J. Goldwin, K. Aravinthan, S.G. Raj, G.R. Kumar, Synthesis and Characterization of Nanocrystalline Yttrium Iron Garnet ($Y_3Fe_5O_{12}$) for Magnetoelectric Applications, (n.d.) 5.

[190] T. Ramesh, G.N. Rao, T. Suneetha, R.S. Shinde, V. Rajendar, S.R. Murthy, S.A. Kumar, Microwave-Hydrothermal Synthesis of $Y_3Fe_5O_{12}$ Nanoparticles: Sintering Temperature Effect on Structural, Magnetic and Dielectric Properties, J Supercond Nov Magn 31 (2018) 1899–1908. https://doi.org/10.1007/s10948-017-4425-6.

[191] M. Pardavi-Horvath, Microwave applications of soft ferrites, Journal of Magnetism and Magnetic Materials 215–216 (2000) 171–183. https://doi.org/10.1016/S0304-8853(00)00106-2.

[192] K. Sadhana, S.R. Murthy, K. Praveena, Effect of Sm^{3+} on dielectric and magnetic properties of $Y_3Fe_5O_{12}$ nanoparticles, J Mater Sci: Mater Electron 25 (2014) 5130–5136. https://doi.org/10.1007/s10854-014-2282-7.

[193] K. Praveena, S. Srinath, Effect of Gd^{3+} on dielectric and magnetic properties of $Y_3Fe_5O_{12}$, Journal of Magnetism and Magnetic Materials 349 (2014) 45–50. https://doi.org/10.1016/j.jmmm.2013.08.035.

[194] M.A. Musa, R.S. Azis, N.H. Osman, J. Hassan, T. Zangina, Structural and magnetic properties of yttrium iron garnet (YIG) and yttrium aluminum iron garnet (YAlG) nanoferrite via sol-gel synthesis, Results in Physics 7 (2017) 1135–1142. https://doi.org/10.1016/j.rinp.2017.02.038.

[195] C.-C. Huang, Y.-H. Hung, J.-Y. Huang, M.-F. Kuo, Performance improvement of S-band phase shifter using Al, Mn and Gd doped $Y_3Fe_5O_{12}$ and sintering optimization, Journal of Alloys and Compounds 643 (2015) S193–S198. https://doi.org/10.1016/j.jallcom.2014.12.123.

[196] M.I. Khan, M. Waqas, M.A. Naeem, M.S. Hasan, M. Iqbal, A. Mahmood, S.M. Ramay, W. Al-Masry, S.A. Abubshait, H.A. Abubshait, Q. Mahmood, Magnetic behavior of Ga doped yttrium iron garnet ferrite thin films deposited by sol-gel technique, Ceramics International 46 (2020) 27318–27325. https://doi.org/10.1016/j.ceramint.2020.07.217.

[197] J.J. Hudgens, R.K. Brow, D.R. Tallant, S.W. Martin, Raman spectroscopy study of the structure of lithium and sodium ultraphosphate glasses, Journal of Non-Crystalline Solids 223 (1998) 21–31. https://doi.org/10.1016/S0022-3093(97)00347-5.

[198] J.E. Pemberton, L. Latifzadeh, J.P. Fletcher, S.H. Risbud, Raman spectroscopy of calcium phosphate glasses with varying calcium oxide modifier concentrations, Chem. Mater. 3 (1991) 195–200. https://doi.org/10.1021/cm00013a039.

[199] C. Ivascu, A. Timar Gabor, O. Cozar, L. Daraban, I. Ardelean, FT-IR, Raman and thermoluminescence investigation of P_2O_5–BaO–Li_2O glass system, Journal of Molecular Structure 993 (2011) 249–253. https://doi.org/10.1016/j.molstruc.2010.11.047.

[200] G.S. Henderson, R.T. Amos, The structure of alkali germanophosphate glasses by Raman spectroscopy, Journal of Non-Crystalline Solids 328 (2003) 1–19. https://doi.org/10.1016/S0022-3093(03)00478-2.

[201] B.N. Nelson, G.J. Exarhos, Vibrational spectroscopy of cation-site interactions in phosphate glasses, J. Chem. Phys. 71 (1979) 2739–2747. https://doi.org/10.1063/1.438679.

[202] O. Cozar, D.A. Magdas, L. Nasdala, I. Ardelean, G. Damian, Raman spectroscopic study of some lead phosphate glasses with tungsten ions, Journal of Non-Crystalline Solids 352 (2006) 3121–3125. https://doi.org/10.1016/j.jnoncrysol.2006.03.066.

[203] H.H. Eysel, K.T. Lim, Raman intensities of phosphate and diphosphate ions in aqueous solution, Journal of Raman Spectroscopy 19 (1988) 535–539. https://doi.org/10.1002/jrs.1250190807.

[204] G. Niaura, A.K. Gaigalas, V.L. Vilker, Surface-Enhanced Raman Spectroscopy of Phosphate Anions: Adsorption on Silver, Gold, and

Copper Electrodes, J. Phys. Chem. B 101 (1997) 9250–9262. https://doi.org/10.1021/jp970097k.

[205] G. Niaura, R. Jakubėnas, The alkali metal cation effect on the surface-enhanced Raman spectra of phosphate anions adsorbed at silver electrodes, Journal of Electroanalytical Chemistry 510 (2001) 50–58. https://doi.org/10.1016/S0022-0728(01)00542-3.

[206] L.Y. Zhang, H. Li, L.L. Hu, Statistical structure analysis of GeO_2 modified Yb^{3+}: Phosphate glasses based on Raman and FTIR study, Journal of Alloys and Compounds 698 (2017) 103–113. https://doi.org/10.1016/j.jallcom.2016.12.175.

[207] S. Agathopoulos, D.U. Tulyaganov, J.M.G. Ventura, S. Kannan, M.A. Karakassides, J.M.F. Ferreira, Formation of hydroxyapatite onto glasses of the CaO-MgO-SiO_2 system with B_2O_3, Na_2O, CaF_2 and P_2O_5 additives, Biomaterials 27 (2006) 1832–1840. https://doi.org/10.1016/j.biomaterials.2005.10.033.

[208] A. Saranti, I. Koutselas, M.A. Karakassides, Bioactive glasses in the system CaO–B_2O_3–P_2O_5: Preparation, structural study and in vitro evaluation, Journal of Non-Crystalline Solids 352 (2006) 390–398. https://doi.org/10.1016/j.jnoncrysol.2006.01.042.

[209] B.C. Cornilsen, R.A. Condrate, The vibrational spectra of magnesium pyrophosphate polymorphs, Journal of Physics and Chemistry of Solids 38 (1977) 1327–1332. https://doi.org/10.1016/0022-3697(77)90003-8.

[210] C.C. Pye, W.W. Rudolph, An ab Initio, Infrared, and Raman Investigation of Phosphate Ion Hydration, J. Phys. Chem. A 107 (2003) 8746–8755. https://doi.org/10.1021/jp035594h.

[211] S. Damodaraiah, V. Reddy Prasad, R.P. Vijaya Lakshmi, Y.C. Ratnakaram, Luminescence behaviour and phonon sideband analysis of europium doped Bi_2O_3 based phosphate glasses for red emitting device applications, Optical Materials 92 (2019) 352–358. https://doi.org/10.1016/j.optmat.2019.04.060.

[212] M. Shwetha, B. Eraiah, Influence of europium (Eu^{3+}) ions on the optical properties of lithium zinc phosphate glasses, IOP Conf. Ser.: Mater. Sci. Eng. 310 (2018) 012033. https://doi.org/10.1088/1757-899X/310/1/012033.

[213] S.S. Babu, K. Jang, E.J. Cho, H. Lee, C.K. Jayasankar, Thermal, structural and optical properties of Eu^{3+}-doped zinc-tellurite glasses, J. Phys. D: Appl. Phys. 40 (2007) 5767–5774. https://doi.org/10.1088/0022-3727/40/18/038.

[214] W. Stambouli, H. Elhouichet, B. Gelloz, M. Férid, Optical and spectroscopic properties of Eu-doped tellurite glasses and glass ceramics, Journal of Luminescence 138 (2013) 201–208. https://doi.org/10.1016/j.jlumin.2013.01.019.

[215] A.V. Egorysheva, V.D. Volodin, A.A. Chistyakov, Yu.A. Kuzishchin, V.M. Skorikov, T.D. Dudkina, Luminescence of europium-doped BaO-

Bi2O3-B2O3 glasses, Inorg Mater 46 (2010) 1384–1390. https://doi.org/10.1134/S0020168510120204.

[216] J. Deng, W. Li, H. Zhang, Y. Liu, B. Lei, H. Zhang, L. Liu, X. Bai, H. Luo, H. Liu, W.-R. Liu, J. Wang, Eu $^{3+}$ -Doped Phosphor-in-Glass: A Route toward Tunable Multicolor Materials for Near-UV High-Power Warm-White LEDs, Advanced Optical Materials 5 (2017) 1600910. https://doi.org/10.1002/adom.201600910.

[217] W. Mao, M. Cai, W. Xie, P. Li, W. Zhen, S. Xu, J. Zhang, Tunable white light in trivalent europium single doped tin fluorophosphates ultra-low melting glass, Journal of Alloys and Compounds 805 (2019) 205–210. https://doi.org/10.1016/j.jallcom.2019.07.014.

[218] R. Reisfeld, E. Zigansky, M. Gaft, Europium probe for estimation of site symmetry in glass films, glasses and crystals, Molecular Physics 102 (2004) 1319–1330. https://doi.org/10.1080/00268970410001728609.

[219] J. Meyer, F. Tappe, Photoluminescent Materials for Solid-State Lighting: State of the Art and Future Challenges, Advanced Optical Materials 3 (2015) 424–430. https://doi.org/10.1002/adom.201400511.

[220] G.P. Espinosa, Crystal Chemical Study of the Rare-Earth Iron Garnets, J. Chem. Phys. 37 (1962) 2344–2347. https://doi.org/10.1063/1.1733008.

[221] Z. Cheng, Y. Cui, H. Yang, Y. Chen, Effect of lanthanum ions on magnetic properties of $Y_3Fe_5O_{12}$ nanoparticles, J Nanopart Res 11 (2009) 1185–1192. https://doi.org/10.1007/s11051-008-9501-1.

[222] A. Pakalniskis, D. Baltrunas, K. Mazeika, R. Skaudzius, R. Ramanauskas, A. Kareiva, Reinspection of low temperature synthesis of bulk $Bi_3Fe_5O_{12}$ (BIG): An aqueous sol-gel processing, Materials Chemistry and Physics 253 (2020) 123283. https://doi.org/10.1016/j.matchemphys.2020.123283.

[223] R. Nakamoto, B. Xu, C. Xu, H. Xu, L. Bellaiche, Properties of rare-earth iron garnets from first principles, Phys. Rev. B 95 (2017) 024434. https://doi.org/10.1103/PhysRevB.95.024434.

[224] D. Vandormael, F. Grandjean, D. Hautot, G.J. Long, Mössbauer spectral evidence for rhombohedral symmetry in $R_3Fe_5O_{12}$ garnets with R = Y, Eu and Dy, J. Phys.: Condens. Matter 13 (2001) 1759–1772. https://doi.org/10.1088/0953-8984/13/8/312.

[225] O. Opuchovic, A. Kareiva, K. Mazeika, D. Baltrunas, Magnetic nanosized rare earth iron garnets $R_3Fe_5O_{12}$: Sol–gel fabrication, characterization and reinspection, Journal of Magnetism and Magnetic Materials 422 (2017) 425–433. https://doi.org/10.1016/j.jmmm.2016.09.041.

[226] R. Skaudzius, J. Pinkas, R. Raudonis, A. Selskis, R. Juskenas, A. Kareiva, On the limitary radius of garnet structure compounds $Y_3Al_{5-x}M_xO_{12}$ (M = Cr, Co, Mn, Ni, Cu) and $Y_3Fe_{5-x}Co_xO_{12}$ ($0 \leq x \leq 2.75$) synthesized by sol–gel method, Materials Chemistry and

Physics 135 (2012) 479–485. https://doi.org/10.1016/j.matchemphys.2012.05.011.

[227] A.M. Hofmeister, K.R. Campbell, Infrared spectroscopy of yttrium aluminum, yttrium gallium, and yttrium iron garnets, Journal of Applied Physics 72 (1992) 638–646. https://doi.org/10.1063/1.351846.

[228] B. Bai, P. Dang, D. Huang, H. Lian, J. Lin, Broadband Near-Infrared Emitting $Ca_2LuScGa_2Ge_2O_{12}$:Cr^{3+} Phosphors: Luminescence Properties and Application in Light-Emitting Diodes, Inorg. Chem. 59 (2020) 13481–13488. https://doi.org/10.1021/acs.inorgchem.0c01890.

[229] H. Lin, G. Bai, T. Yu, M.-K. Tsang, Q. Zhang, J. Hao, Site Occupancy and Near-Infrared Luminescence in $Ca_3Ga_2Ge_3$O12: Cr^{3+} Persistent Phosphor, Advanced Optical Materials 5 (2017) 1700227. https://doi.org/10.1002/adom.201700227.

[230] K.E. Lipinska-Kalita, D.M. Krol, R.J. Hemley, P.E. Kalita, C.L. Gobin, Y. Ohki, Temperature effects on luminescence properties of Cr^{3+} ions in alkali gallium silicate nanostructured media, Journal of Applied Physics 98 (2005) 054302. https://doi.org/10.1063/1.2012509.

[231] V. Rajendran, M.-H. Fang, W.-T. Huang, N. Majewska, T. Lesniewski, S. Mahlik, G. Leniec, S.M. Kaczmarek, W.K. Pang, V.K. Peterson, K.-M. Lu, H. Chang, R.-S. Liu, Chromium Ion Pair Luminescence: A Strategy in Broadband Near-Infrared Light-Emitting Diode Design, J. Am. Chem. Soc. 143 (2021) 19058–19066. https://doi.org/10.1021/jacs.1c08334.

[232] K. Li, D. Xue, Estimation of Electronegativity Values of Elements in Different Valence States, J. Phys. Chem. A 110 (2006) 11332–11337. https://doi.org/10.1021/jp062886k.

[233] K. Li, D. Xue, New development of concept of electronegativity, Chin. Sci. Bull. 54 (2009) 328–334. https://doi.org/10.1007/s11434-008-0578-9.

NOTES

NOTES

NOTES

Vilniaus universiteto leidykla
Saulėtekio al. 9, III rūmai, LT-10222 Vilnius
El. p. info@leidykla.vu.lt, www.leidykla.vu.lt
bookshop.vu.lt, journals.vu.lt
Tiražas 15 egz.